Fundamentals and application of solid-state phase transformations for advanced high strength steels containing metastable retained austenite

Dai, Zongbiao; Chen, Hao; Ding, Ran; Lu, Qi; Zhang, Chi; Yang, Zhigang; van der Zwaag, Sybrand

DOI
10.1016/j.mser.2020.100590

Publication date
2021

Document Version
Accepted author manuscript

Published in
Materials Science and Engineering R: Reports

Materials Science & Engineering R

Fundamentals and application of solid-state phase transformations for advanced high strength steels containing metastable retained austenite

--Manuscript Draft--

Manuscript Number:	
Article Type:	Review article
Keywords:	Automotive steels; Solid-state Phase transformations; Retained austenite; Microstructures; Steel chemistry; Alloy design
Corresponding Author:	Zongbiao Dai Tsinghua University Beijing, China CHINA
First Author:	Zongbiao Dai
Order of Authors:	Zongbiao Dai
	Hao Chen
	Ran Ding
	Qi Lu
	Chi Zhang
	Zhigang Yang
	Sybrand van der Zwaag
Abstract:	Over many decades, significant efforts have been made to improve the strength-elongation product of advanced high strength steels (AHSSs) by creating tailored multi-phase microstructures. Successive solid-state phase transformations for steels with a well selected chemical composition turned out to be the key instrument in the realisation of such microstructures. In this contribution, we first provide a brief review of the desired microstructures for Transformation-induced plasticity (TRIP), Carbide-free Bainitic (CFB), Quenching & Partitioning (Q&P) and Medium Manganese steels followed by comprehensive discussions on the phase transformations to be used in their creation. The implications for the steel composition to be selected are addressed too. As the presence of the right amount and type of metastable retained austenite (RA) is of crucial importance for the mechanical performance of these AHSSs, special attention is paid to the important role of successive solid-state phase transformations in creating the desired fraction and composition of RA by suitable element partitioning (in particular C and Mn). This critical partitioning not only takes place during final cooling (austenite decomposition) but also during the back transformation (austenite reversion) during reheating. This review aims to be more than just descriptive of the various findings, but to present them from a coherent thermodynamic / thermo-kinetic perspective, such that it provides the academic and industrial community with a rather complete conceptual and theoretical framework to accelerate the further development of this important class of steels. The detailed stepwise treatment makes the review relevant not only for experts but also metallurgists entering the field.
Suggested Reviewers:	Matthias Militzer, PhD Dofasco Chair in Advanced Steel Processing, University of British Columbia Matthias.Militzer@ubc.ca Prof. Militzer is an expert in the field of physical metallurgy and multi-scale modelling of microstructure evolution of advanced high strength steels.
	Hatem Zurob, PhD Chair, McMaster University zurobh@mcmaster.ca Prof. Zurob is an expert in the field of phase transformations and microstructure evolution simulation in steels.
	Gary Purdy, PhD McMaster University

	purdyg@mcmaster.ca Prof. Purdy is an expert in the field of physical metallurgyphase transformation in metals.
	Annika Borgenstam, PhD KTH Royal Institute of Technology annbor@kth.se Prof. Borgenstam is an expert in the field of phase transformations and alloying design in metals.
	Ernst Gamsjäger, PhD Leoben univerisity Ernst.Gamsjaeger@unileoben.ac.at Prof. Gamsjager is an expert in the field of thermodynamics and kinetics of phase transformations in steels.
	Amy Clarke, PhD Colorado School of Mines amyclarke@mines.edu Prof. Clarke is an expert in the field of physical metallurgy and microstructure characterization in advanced high strength steels.
	Peter Hodgson, PhD Deakin University peter.hodgson@deakin.edu.au Prof. Hodgson is an expert in the field of automtive steel manufacturing process and phase transformations in steels.
	Nobuo Nakada, PhD Tokyo Institute of Technology nakada.n.aa@m.titech.ac.jp Prof. Nakada is an expert in the field of phase transformations in steels.
Opposed Reviewers:	Harry Bhadeshia University of Cambridge hkdb@cam.ac.uk Prof. Bhadeshia has a series of earlier professional conflicts with the authors.

Materials Science and Engineering: R: Reports paper

Fundamentals and application of solid-state phase transformations for advanced high strength steels containing metastable retained austenite

Zongbiao Dai[a], Hao Chen[a*], Ran Ding[a], Qi Lu[b], Chi Zhang[a], Zhigang Yang[a], Sybrand van der Zwaag[a,c]

[a] Key Laboratory for Advanced Materials of Ministry of Education, School of Materials Science and Engineering, Tsinghua University, Beijing, China

[b] China Science Lab, General Motors Global Research and Development, Shanghai, China

[c] Faculty of Aerospace Engineering, Delft University of Technology, Kluyverweg 1, 2629HS Delft, The Netherlands

[*] Corresponding author; E-mail: hao.chen@mail.tsinghua.edu.cn

Abstract

Over many decades, significant efforts have been made to improve the strength-elongation product of advanced high strength steels (AHSSs) by creating tailored multi-phase microstructures. Successive solid-state phase transformations for steels with a well selected chemical composition turned out to be the key instrument in the realisation of such microstructures. In this contribution, we first provide a brief review of the desired microstructures for Transformation-induced plasticity (TRIP), Carbide-free Bainitic (CFB), Quenching & Partitioning (Q&P) and Medium Manganese steels followed by comprehensive discussions on the phase transformations to be used in their creation. The implications for the

steel composition to be selected are addressed too. As the presence of the right amount and type of metastable retained austenite (RA) is of crucial importance for the mechanical performance of these AHSSs, special attention is paid to the important role of successive solid-state phase transformations in creating the desired fraction and composition of RA by suitable element partitioning (in particular C and Mn). This critical partitioning not only takes place during final cooling (austenite decomposition) but also during the back transformation (austenite reversion) during reheating.

This review aims to be more than just descriptive of the various findings, but to present them from a coherent thermodynamic / thermo-kinetic perspective, such that it provides the academic and industrial community with a rather complete conceptual and theoretical framework to accelerate the further development of this important class of steels. The detailed stepwise treatment makes the review relevant not only for experts but also metallurgists entering the field.

Keywords: Automotive steels; Solid-state Phase transformations; Retained austenite; Microstructures; Steel chemistry; Alloy design

Nomenclature

Symbol	Description
AHSSs	Advanced high strength steels
ART	Austenite reversion treatment
BCC	Body-centred cubic
B_s	Bainite start temperature
CCE	Constrained carbon equilibrium
CFB	Carbide-free bainitic
DP	Dual phase
EBSD	Electron backscattered diffraction
FCC	Face-centred cubic

GEB	Gibbs energy balance
HE-XRD	High energy X-ray diffraction
IA	Intercritical annealing
IBT	Isothermal bainitic transformation
K-M	Koistinen-Marburger
K-S	Kurdjumove-Sachs
LE	Local equilibrium
M	Substitutional alloying element
M_s	Martensite start temperature
M_f	Martensite finish temperature
MES	Mössbauer effect spectroscopy
NPLE	Negligible partitioning local equilibrium
PE	Para-equilibrium
PLE	Partitioning local equilibrium
Q&P	Quenching and partitioning
RA	Retained austenite
SEM	Scanning electron microscope
3DAPT	Three-dimensional atom probe tomography
TEM	Transmission electron microscopy
TRIP	Transformation-induced plasticity
WBs	Widmanstätten bainite start
XRD	X-ray diffraction

1. Introduction

Given their large share in the steel market and the high pressure on the improvement of their performance over weight and price ratio, advanced high strength steels (AHSSs) for automotive applications have been and remain a major driver in the development of new steels. As a result, there have been major developments in their composition, hot- and cold-rolling processes, microstructure and properties since the application of steel for the car body of early generation cars such as the T-Ford in 1908. The early generations of automotive steels were

simple C-Mn steels obtained via a simple thermomechanical process: continuous cooling immediately following after the hot rolling of the steel in a fully austenitic state. The resulting microstructure consisted of ferrite and pearlite and still had a larger number of impurities. For such a steel the mechanical properties depend primarily on the ferrite grain size and the amount of pearlite present (i.e. the carbon concentration). There are no indications that special attention was given to precisely control the concentration of other alloying elements. Typical mechanical properties of the early generation automotive steels are a yield strength of about 180 MPa and an ultimate tensile strength of 330 MPa [1].

With the progress of understanding of the strengthening mechanisms in ferrous alloys, e.g. solution strengthening, grain size reduction, precipitation hardening and dislocation hardening, the properties of steel grades gradually improved but the microstructures of the steels essentially remained to be a mixture of ferrite and pearlite or carbides in general. As both ferrite and pearlite/carbides are equilibrium phases, plastic deformation of such steels essentially proceeds via the accumulation of dislocations in the ferrite and strain localisation leading to that failure sets in when the strain hardening equals the true stress value, i.e. a so-called Considère principle.

A major step towards substantially raising the mechanical properties of AHSSs was made when the concept of non-equilibrium multi-phase steels was embraced and this led to the development of Dual Phase (DP) steels, in which the microstructure consisted of both ferrite and a sizeable fraction of martensite[2]. Such a microstructure was realised not by making large changes in the steel composition, but by tuning the non-equilibrium phase transformations and elements partitioning using a multi-stage cooling strategy.

Since then, modern steel design relies on tailored partitioning of alloying elements between the parent austenite and its product phases during a multi-stage heat treatment [3]. In the case of the DP steels, the slow cooling of the fully austenitic state leads to the ferrite

formation and carbon enrichment of the remaining austenite. Then, rapid cooling leaves the ferrite unaffected, but transforms the remaining austenite into martensite, provided the remaining austenite has sufficient hardenability. As the volume fraction and hardness of martensite are much higher than the pearlite in conventional steels, the DP steels have a higher yield strength (~ 400 MPa) and ultimate tensile strength (~600 MPa) [4]. Notwithstanding the large volume fraction of martensite and its high hardness, the presence of a continuous network of ferritic grains ensures a good ductility and formability. The properties of DP steels can be tuned by adjusting the austenite grain size and/or adjusting the heat treatment such that different martensite fractions are achieved. It is important to note that the development of DP steels did not require important adjustments in the chemical composition, with C and Mn remaining the main alloying elements, just as in C-Mn steels.

The next step in the development of AHSSs came with the realisation that mechanical properties could be enhanced by introducing metastable retained austenite (RA) into the multiphase microstructures. RA can transform into martensite during plastic deformation and the resulting hardening prevents local damage, thereby permitting greater uniform elongation prior to necking, i.e. Transformation-induced plasticity (TRIP) effect [5, 6]. By tuning the steel composition and the thermal processing conditions, austenite in the final microstructure can be retained if sufficient carbon is accumulated so that the martensite start temperature is below ambient temperature. For such a condition, the metastable austenite will only transform upon plastic deformation but will not transform spontaneously. The creation of such a multiphase microstructure requires more serious adjustments of the composition and the thermal processing in order to allow for even more extensive partitioning of carbon while preventing the formation of cementite by raising the Si and/or Al concentration.

The earliest generation of such RA containing steels is the Transformation-induced plasticity (TRIP) assisted steels [7, 8], with a microstructure that is a ferrite-bainite matrix

interspersed with ‘blocky’ or film-like RA. The properties of TRIP steels resemble those of DP steels but with a higher strength for a given ductility or a higher ductility for a given strength level.

The logical next step in raising the mechanical properties is the replacement of the ferrite fraction in TRIP steels by a bainite fraction, while keeping a comparable RA fraction [9]. This led to the formulation of carbide-free bainitic steels. The approach relies on selecting the right composition, in particular a higher Mn concentration, such that the bainite transformation does not proceed to completion but kinetically halts. The austenite at the end of the bainitic holding treatment then becomes the RA.

An even stronger matrix than a bainitic matrix can be obtained via a tempered martensitic microstructure in combination with enough and the right amount of RA. The production of such a microstructure proved very tricky but this all changed with the invention of the Quenching and Partitioning (Q&P) process [10, 11]. In this process, the steel is first quenched from the fully or partially austenitic state to a temperature in between the martensite start temperature (M_s) and the martensite finish temperature (M_f), and then isothermally held at a temperature above M_s to allow the excess carbon partitioning from martensite into the residual austenite. This versatile process allows many variants but generally yields a nice homogeneous matrix structure and a tuneable amount and type of RA.

Finally, as mechanical properties seem to be highly linked to the amount of RA, much effort was paid to enhance the RA fraction via alloy design. Research into the effects of the austenite stabilising element Mn on the steel microstructure has led to a new family of potential future automotive steels containing a Mn concentration about 3~10 wt.%, i.e. medium Mn steels [12, 13]. Medium Mn steels are intercritically annealed to obtain an ultra-fine ferrite and 20~50 vol.% austenite mixture, during which both C and Mn partition from martensite into austenite to enhance austenite stability. This processing is called the austenite reversion treatment (ART).

The strength-elongation ranges for the AHSSs introduced above are illustrated in **Fig. 1**. **Fig. 1a** shows the strength-elongation envelopes for the various types of AHSSs, while **Fig. 1b** shows the same envelopes but classified by their microstructure. The RA containing multi-phase steel grades to be described in more detail in this review are located within the dashed oval. The figure clearly illustrates a higher mechanical performance require both a more complex matrix microstructure and an increasing contribution of the RA.

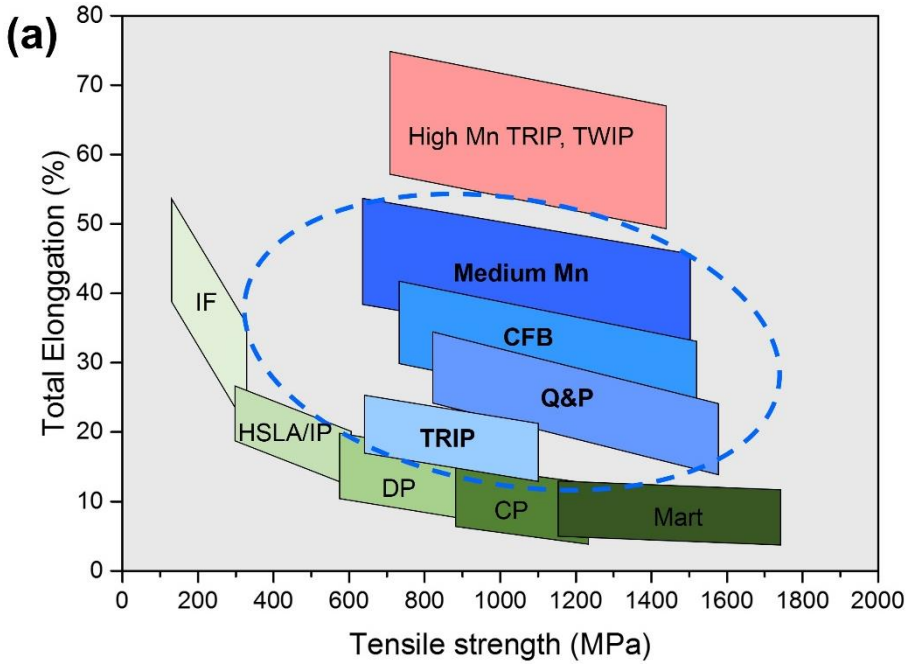

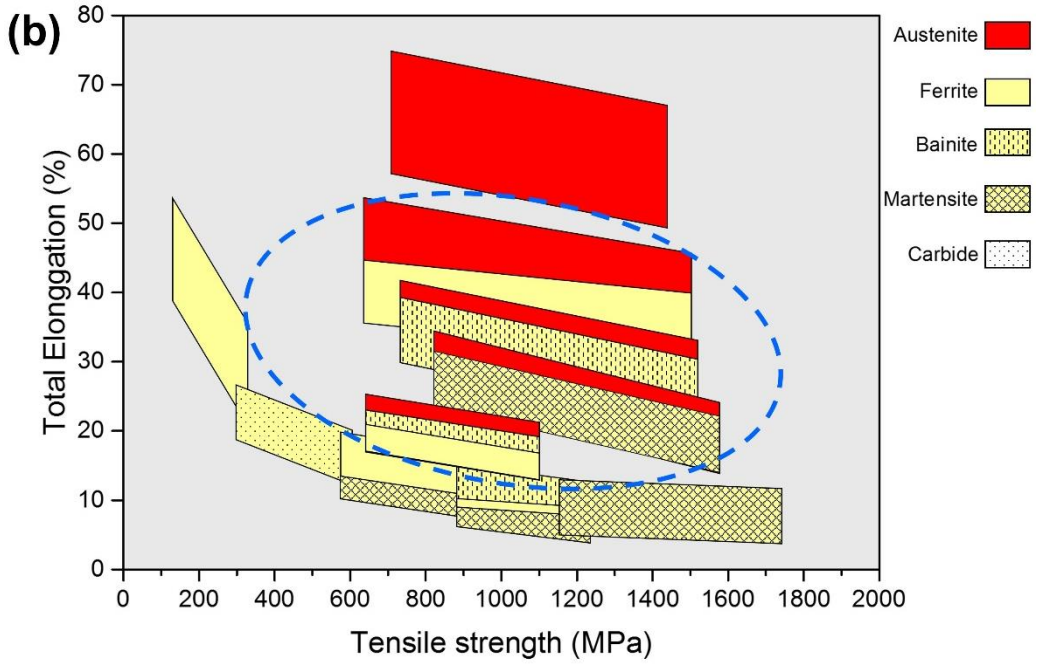

Fig. 1. Classification of the various steel 'families' according to (a) their properties and (b) their corresponding microstructure. IF: interstitial free steel; HSLA: high strength low alloyed steel; DP: dual phase steel; CP: complex phase steel; Mart: martensitic steel; TRIP: transformation-induced plasticity steel; TWIP: twinning-induced plasticity steel; CFB: carbide-free bainitic steel; Q&P: quenching and partitioning steel.

It is the aim of this paper to describe and explain the key phase transformations required in the realisation of these four types of modern automotive steel grades (TRIP, CFB, Q&P and medium Mn steels) and to show at the same time how the required solid-state phase transformations not only require new multi-step thermal routes but also require tuning of the chemical composition. While other reviews on AHSSs focus on thermomechanical processing parameters [14], this review will link the formation of the microstructure to the underlying thermodynamics and kinetics of the subsequent transformations. The TRIP steels, as the first generation AHSSs, has been well investigated and reviewed [4, 8, 15]. We will briefly review the recent advances on TRIP steels and mainly focus on the progress in the new third generation AHSSs (CFB, Q&P and medium Mn steels).

Finally, this review ends with a short summary of the key unresolved issues in the field and future prospects for rationally designing the microstructure of AHSSs based on successive solid-state phase transformations.

2. Transformation-induced plasticity (TRIP) steels

2.1. Desired microstructures and required chemical composition

The target microstructure of a TRIP steel consists of 50~55 vol.% ferrite, 30~35 vol.% bainitic ferrite and 7~15 vol.% RA [16]. While not always intentional a TRIP steel may also contain some martensite. The ferrite phase with its relatively large grain size (~10 μm) and low hardness is responsible for a better elongation and formability than a fully bainitic microstructure. Besides, a considerable amount of ferrite can enhance the hardenability of austenite. The bainite phase has a much smaller size and has a higher hardness. The RA grains are generally small and come in two morphologies: somewhat larger equiaxed 'blocky' austenite grains with a diameter of 1~2 μm and 'film-like' austenite grains with a typical thickness of ~20 nm and a length of ~200 nm. The blocky RA is found near or within the ferrite grains while the film-like RA is usually found in between the bainitic islands. A typical microstructure of a commercial cold-rolled TRIP780 steel is shown in **Fig. 2**.

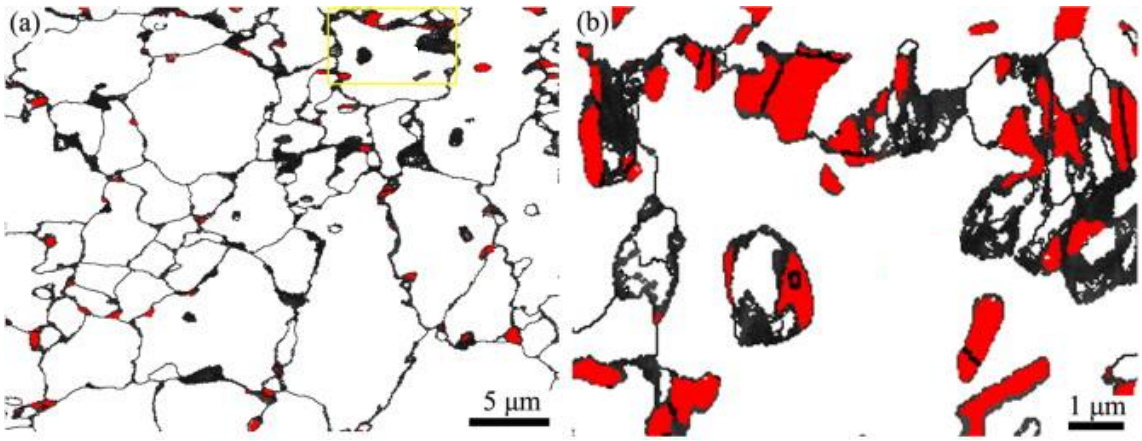

Fig. 2. (a) EBSD images of a commercial cold-rolled Fe-0.20C-1.87Mn-1.42Si-0.04Al-0.012P TRIP780 steel [17]. (b) magnified area in (a). Retained austenite, martensite/austenite island and ferrite/bainite are represented by red, black and white, respectively. Black lines represent high-angle boundaries (>10°).

Given the fact that ferrite and bainitic ferrite have a very low carbon concentration of about 0.02 wt.% and the RA must have a carbon concentration of 0.6~1.5 wt.% in order to be stable at room temperature, it is clear that the overall carbon concentration of a TRIP steel must be of the order of 0.1 to 0.4 wt.%. For reasons of weldability, the current TRIP steels usually have a carbon concentration of 0.20~0.25 wt.% C or less. In the literature different values for the average C concentration in the RA grains have been reported. In part these differences are real due to processing and composition differences and in part they are artificial due to experimental uncertainties [18-21]. The suppression of unwanted precipitation of carbides which affects the carbon balance in the creation of sufficiently C-enriched austenite is realised by alloying the steel with Si (typically 0.4~1.8 wt.%), Al (typically 0.3~0.8 wt.%) or P (typically 0.05~0.1 wt.%) or combinations thereof [8, 22]. Mn is added in concentrations of 0.2~2.5 wt.% to control the kinetics of the phase transformations [8]. Other alloying elements, such as Cu, Cr and Ni [23], may be added for improved mechanical properties, but their concentrations are generally low and they do not play an important role in the creation of the characteristic microstructure of a TRIP steel. The use of micro-alloying elements in order to reduce the size of the ferrite grains and to strengthen the ferritic matrix has been explored [24] but most commercial TRIP steels are free of micro-alloying elements to reduce costs.

2.2. Starting microstructures and processing routes

TRIP steels can be made from a hot-rolled starting condition in which case the starting microstructure is a fully austenitic microstructure containing equiaxed austenitic grains, or from a cold-rolled starting condition in which case the starting microstructure contains two geometrically and compositionally different microstructural components: relatively large elongated ferrite grains with a high dislocation density and small pearlite colonies or isolated

carbides. While the early research on TRIP steels focussed on materials produced directly after hot-rolling, most commercial TRIP steels are now produced from cold-rolled starting materials [14].

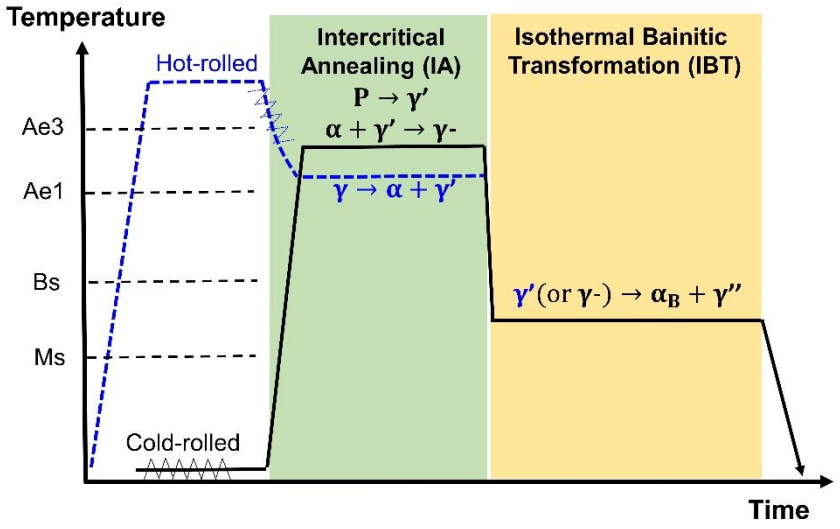

Fig. 3. Thermo-mechanical processing of TRIP steels via the hot-rolling and the cold-rolling routes. α: ferrite; α_B: bainitic ferrite; P: pearlite; γ: austenite; γ-: carbon-depleted austenite; γ′, γ′′: carbon-enriched austenite.

The typical processing routes for the hot-rolled and the cold-rolled steels and the critical phase transformations are shown in **Fig. 3**. The creation of the desired microstructure starts with an intermediate intercritical annealing (IA) treatment in which either the starting austenite or the starting ferrite-pearlite structure is transformed into a ferrite-austenite mixture. The volume fractions of austenite and ferrite depend on the intercritical holding temperature, the holding time and the initial microstructure [25]. The temperatures to be selected are in between the Ae_1 and the Ae_3 temperatures for the nominal steel composition. As will be explained below in more detail, the actual intercritical holding temperature to be used also depends on the initial microstructure.

After the IA process, the steel is cooled to the isothermal bainitic transformation (IBT) temperature (350~490°C) and holding for 4~8 minutes, during which the austenite transforms

to bainite. Note that slow cooling rates will lead to a higher ferrite fraction and a larger ferrite grain size [26], while fast cooling will lead to a higher bainite fraction [27]. After the IBT process, the steel is further quenched to room temperature. It is clear that, for a short bainitic holding time, the average carbon concentration in the remaining austenite is relatively low, which may cause austenite to partially transform to martensite during final cooling to room temperature leading to a reduced final RA fraction [28]. In case of a long bainitic holding time the carbon concentration in the austenite grains will be higher and they will easily survive during the final quenching. However, the final RA fraction present will again be lower as the starting austenite fraction at the end of the IBT process has decreased [20, 29]. The maximum obtainable carbon concentration in austenite after the IBT process is determined by the occurrence of the incomplete bainitic transformation also called the bainitic stasis. The optimal combination of a high volume fraction of RA grains having a suitable stability such that they will transform into martensite upon mechanical straining can be obtained by tuning the bainitic temperature and holding time [30]. At this point it might be appropriate to stipulate that the expression 'austenite stability' is a rather generic term as there are many factors all playing a role simultaneously in determining the stress or strain values at which stress or strain level an individual grain will transform from austenite to martensite. High resolution in-situ diffraction experiments following the transformation of individual RA grains in TRIP and other RA containing AHSSs have shown the effects of grain size [20, 31], carbon concentration [31-33], orientation with respect to the principal loading direction [33], temperature [33], nature of the stress field [34, 35]. Micromechanical models [36, 37] showed that the yield stress, the strain hardening and the crystal orientation of the ferritic matrix surrounding the RA play a role too. A full discussion of all aspects affecting retained austenite stability is outside the scope of this review.

2.3. Critical phase transformations

2.3.1. Ferrite formation during intercritical annealing

The formation of ferrite from austenite is probably the best studied ferrous phase transformation of all, as it was and is the most important phase transformation for all past and present AHSSs. The austenite-to-ferrite transformation involves both a reconstruction of the crystal lattice (the transition from the parent austenite (γ) or FCC crystal structure to the product ferrite (α) or BCC crystal structure) as well as a redistribution of the alloying elements. The tendency to partitioning is due to the difference in solubility of each element in austenite and ferrite. The most important partitioning reaction is that of carbon, which has a high solubility in austenite and a low solubility in ferrite. As the diffusion coefficient of carbon in ferrite is much higher than that in austenite, the early models for the austenite-to-ferrite transformation, e.g. the Zener model [38], considered a homogeneous carbon distribution in the ferrite, local equilibrium at the moving α/γ interface and a carbon gradient in the austenite, which continues until the transformation comes to completion. For a simple binary Fe-C system, i.e. the reference system for all AHSSs, the kinetics of the moving interface is determined by the diffusion of carbon only and the reconstruction of the interface is assumed not to play any kinetic role. This does not mean that the interface mobility is infinite, it is just that the effect of the carbon diffusion on the velocity of the interface is dominant.

AHSSs, such as TRIP steels, also contain substitutional alloying elements M (M=Mn, Si and/or Al), which have much lower diffusion coefficient than carbon. Therefore, partitioning of these substitutional alloying elements is not as extensive and complete as thermodynamically predicted. The partitioning extent of substitutional alloying elements M across the interface plays a critical role in the kinetics of interface migration. As shown in **Fig. 4** (for the case of austenite-to-ferrite transformation), in the conceptual limit, there are three modes for the

interaction between substitutional alloying elements M partitioning and interface migration behavior: *(i)* the paraequilibrium (PE) mode, in which M is assumed not to partition at all and the kinetics of interface migration is only determined by C diffusion [39, 40]. *(ii)* the negligible-partitioning local equilibrium (NPLE) mode, in which there is only a very sharp spike of enriched M at the moving interface and the kinetics of interface migration is mainly determined by the C diffusion [39, 41, 42]. *(iii)* the partitioning local equilibrium (PLE) mode, in which M is assumed to partition across the interface significantly [39, 41, 42]. Under the PLE mode, the kinetics of interface migration is determined by M diffusion and the thermodynamic equilibrium (full equilibrium) is reached very sluggishly. The various modes of austenite-to-ferrite transformation in relation to steel composition and their thermodynamic origin have been described comprehensively in a recent review paper [43]. In the the multicomponent diffusional approach, the net velocity of the interface is in principle determined by the diffusion of all alloying components, but with different roles for the fast-moving interstitial C and the sluggish moving substitutional elements M at different stages of the transformation, leading to the NPLE mode and the PLE mode.

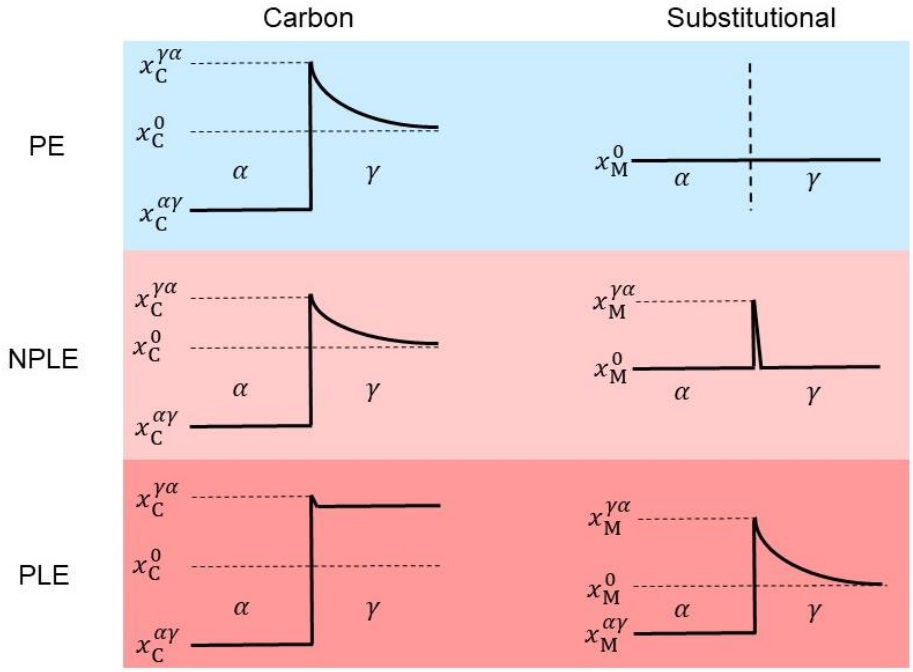

Fig. 4. C and M element distributions near the migrating interface for the PE, NPLE and PLE modes. x_i^0, bulk content of element *i*; $x_i^{\alpha/\gamma}$, content of element *i* in ferrite at the interface; $x_i^{\gamma/\alpha}$, content of element *i* in austenite at the interface.

In order to obtain a considerable amount of ferrite in a certain time period, the intercritical annealing condition should be selected to ensure the austenite-to-ferrite transformation taking place under the NPLE mode. The schematic isothermal section of the Fe-C-M phase diagram showing the NPLE and PLE regions during the ferrite formation starting from a fully austenitic starting condition for a typical TRIP steel composition is shown in **Fig. 5**. The figure also shows the relevant C and M profiles. **Fig. 5** shows that the austenite-to-ferrite transformation starts in the NPLE mode, i.e. the growing ferrite inherits the M content of the parent austenite. Hence, the composition of the newly formed ferrite, point P, is determined by the intersection between carbon component ray PR and the $\alpha/(\alpha+\gamma)$ phase boundary. A positive spike of M appears ahead of the interface in the austenite phase. The carbon concentration at the interface in the austenite is given by the interactions between the tie-line QR and the carbon component ray PR, point R. As a result, a large carbon activity gradient is present in the austenite and the austenite-to-ferrite transformation proceeds via carbon diffusion. As the ferrite formation proceeds the carbon concentration in the core of the grain will reach a value marked by point R and the transformation switches to the PLE mode. This condition can be simply regarded as the onset of the transformation stasis, although there is no very sudden change of the kinetic mode from NPLE to PLE in actual phase transformation. The NPLE/PLE transition concept has been shown to be an effective and practical tool to estimate the remaining austenite fraction and the carbon concentration in austenite [44], which are the critical starting conditions for the subsequent IBT.

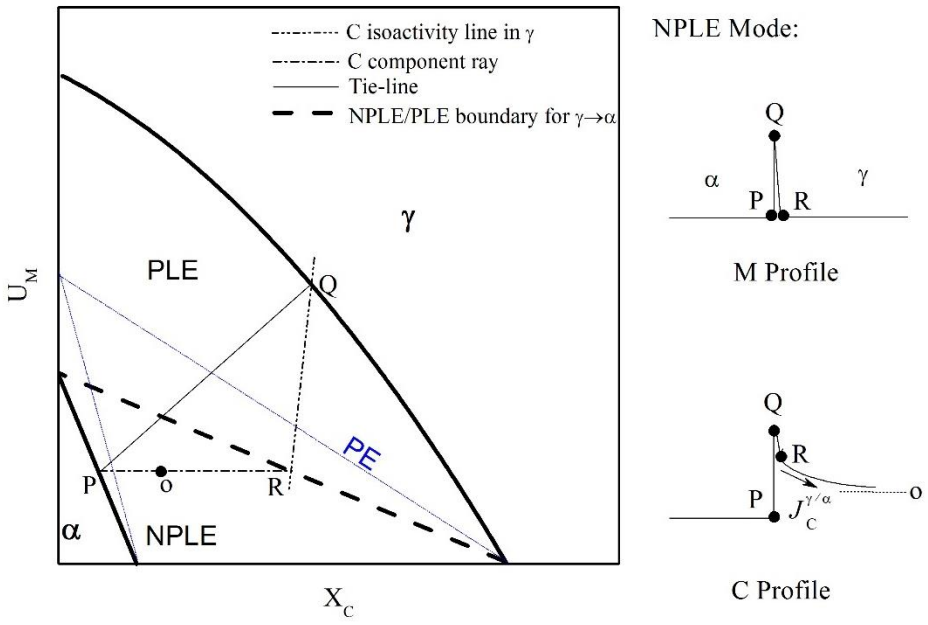

Fig. 5. Schematic isothermal section of the Fe-C-M system phase diagram showing the NPLE and PLE regions for the austenite-to-ferrite transformation. PE boundary is also shown for a comparison. $U_M = X_M/ (1-X_C)$, where X_C and X_M represent the mole fractions of C and M, respectively. $J_C^{\gamma/\alpha}$ is the carbon flux in austenite at the interface.

In the multi-component diffusion approach the reorganisation of the crystal structure itself is assumed to proceed fast enough and not to affect the transformation kinetics. An alternative approach to describe the austenite-to-ferrite transformation is that of the mixed-mode transformation concept in which the transformation rate is assumed to be determined by both the carbon diffusion and the interface mobility [45-47]. The value of the effective α/γ interface mobility depends on temperature and alloy composition, but recent work on massive transformations in binary Fe-M alloys has demonstrated how to separate the chemical component in the effective interface mobility and to derive the intrinsic mobility of the α/γ interface [48]. In a recent paper [49], it was shown that notwithstanding the large conceptual differences between the mixed-mode model and the purely diffusional model, the generalised

form of the mixed-mode model nicely allows a continuous transition from the PE to the LE behaviour depending on the boundary conditions and the solute content of the alloy.

The above paragraphs focussed on the effect of composition on the kinetics of the α/γ interface migration, but the actual transformation kinetics in a TRIP steel production depends also on the cooling rate and the starting microstructure, in particular the austenite grain size, the number of nuclei and their location in the austenite grains, and the amount of dislocations stored in the austenite. This effect of the geometrical conditions on the overall transformation kinetics is generally overlooked but can be very large [50]. There are now several two/three-dimensional models for the kinetics of the austenite decomposition which consider grain size variations, nucleation site distributions, soft/ hard impingement conditions and cooling rate [51-53]. Of particular interest is a recent work by Toloui and Militzer [53] showing that the austenite decomposition kinetics as well as the fractions and morphologies of the products in a TRIP steel production can be well simulated by an integrated phase field model with fitting effective interface mobilities.

2.3.2. Austenite formation during intercritical annealing

As stated in section 2.1, the required intermediate austenite + ferrite microstructure at the intercritical annealing temperature can also be reached by heating a TRIP steel after cold rolling. In that case the starting microstructure consists of both (deformed) ferrite grains and (broken-up) pearlite colonies (or isolated carbides). Hence the transformation process is more complicated and consists of three more or less consecutive steps [54, 55]: *(i)* the very rapid transformation of pearlite into a carbon enriched austenite of more or less the same dimensions as the pearlite colony, due to the high C activity of the cementite and the small ferrite-cementite spacings, *(ii)* the fast growth of this austenite into the surrounding ferrite matrix with kinetics

determined by carbon diffusion with only a spike of M at the interface and *(iii)* the very slow austenite growth dictated by the diffusion of M. As the stage *(iii)* is extremely slow, and thus the transition from stage *(ii)* to *(iii)* is of practical interest.

Recently, the transition between stage *(ii)* and *(iii)* during the austenite formation starting from a ferrite-pearlite microstructure has also been modelled by Dai et al. [44] using a multi-component diffusional approach and the evolution of the critical concentrations are illustrated in **Fig. 6**.

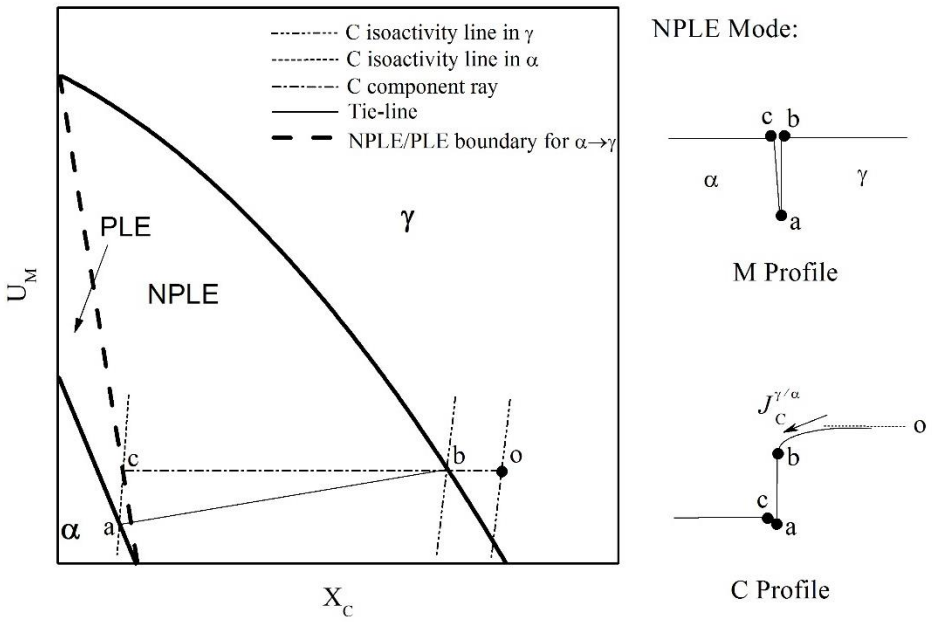

Fig. 6. Schematic isothermal section of the Fe-C-M system phase diagram showing the NPLE and PLE regions for the ferrite-to-austenite transformation. $U_M = X_M/(1-X_C)$, where X_C and X_M represent the mole fractions of C and M, respectively. $J_C^{\gamma/\alpha}$ is the carbon flux in austenite at the interface.

Immediately after the complete dissolution of the pearlite colony a small austenitic region of a C and Mn concentration marked by point 'o' is obtained. Since the diffusivity of M is much lower than that of carbon, the newly formed austenite inherits the M content of the parent ferrite phase. Hence, the interfacial composition of phase is determined by the intersection between

carbon component ray bc and $\gamma/(\alpha+\gamma)$ phase boundary, Point b. Under such a condition, the carbon activity in austenite is larger than that at the interface, which creates a large carbon activity gradient in austenite. In order to satisfy the LE condition, a negative spike of M, which is determined by the end of tie-line ab connecting with the $\alpha/(\alpha+\gamma)$ phase boundary, will appear ahead of the interface in the ferrite phase. Assuming that the carbon activity in ferrite is not affected by the thin M spike at the interface, the composition at the ferritic side of the interface will be determined by the intersection between the carbon iso-activity line ac and the carbon component ray bc, Point c. Under such circumstances, the kinetics of the ferrite-to-austenite transformation is controlled by the carbon diffusion in austenite while a spike of M exists ahead of the interface. As for the ferrite-to-austenite transformation, the initial stage of the transformation proceeds under the NPLE mode. As the transformation proceeds, carbon content in austenite gradually decreases to Point b and thus the carbon activity gradient in austenite disappears. Hence the interface velocity drops, which allows the redistribution of M across the interface. Therefore, the kinetics of the ferrite-to-austenite transformation switches into M diffusion controlled PLE mode and a stasis-like stage is obtained before the transformation proceeds to full equilibrium.

As implicitly shown in the comparison of **Fig. 5** and **Fig. 6**, for a given intercritical annealing temperature, the carbon concentrations in austenite at the onset of the transformation stasis are quite different depending on the starting microstructure being fully austenitic or ferritic-pearlitic. This implies that the apparent NPLE fractions of austenite and ferrite depend on the starting condition. **Fig. 7** clearly shows that the C concentration in austenite will be higher (and hence the austenite fraction will be lower) if the starting condition was ferrite+pearlite instead of fully austenitic. This dependence of the intercritical austenite fraction (at a given intercritical annealing time) on the initial microstructure has also been reported by others [29, 56] and the dependence becomes stronger with an increasing Mn content [57].

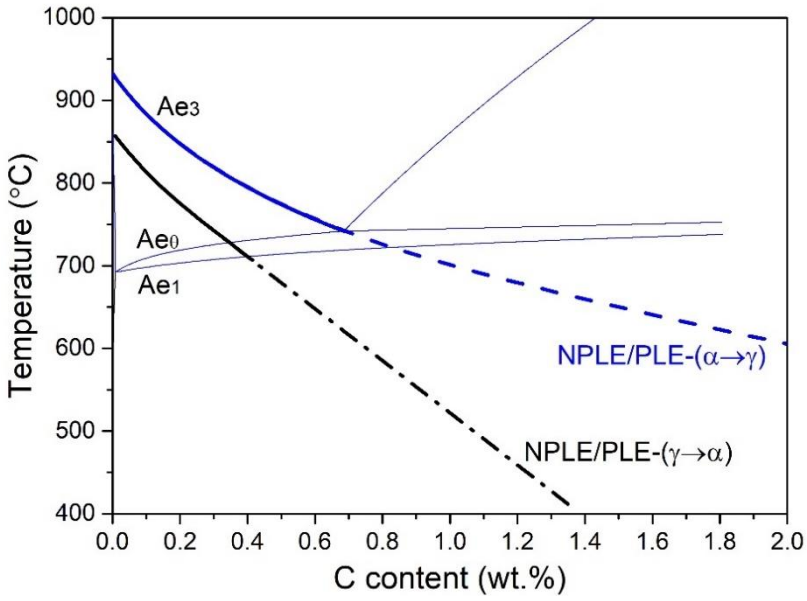

Fig. 7. The NPLE/PLE transition lines for the austenite-to-ferrite transformation and the ferrite-to-austenite transformation are plotted on the partial vertical section of the Fe-*x*C-1.5Mn-1.5Si (in wt.%) steel phase diagram [44].

Finally, the ferrite-to-austenite transformation kinetics could also be described satisfactorily by a mixed-mode model [58-60]. The value of effective interface mobility for the ferrite-to-austenite transformation is different from that for the austenite-to-ferrite transformation. This aspect was addressed by Gamsjaeger [61] who compared in a computational study range the cyclic partial phase transformation of Fe-0.1C-*x*Mn alloys as calculated using DICTRA software with the predictions of the mixed-mode model. Recent work [48] on massive transformations in binary Fe-M alloys further demonstrated that the intrinsic interface mobility depends marginally on the transformation direction. Although the mixed-mode model has some physical and computational advantages over the full diffusion theory, a major remaining drawback of the model is the uncertainty of the value of the effective interface mobility. To some extent, this drawback has restricted the application of the mixed-mode model in microstructure design of AHSSs.

2.3.3. Bainite formation after intercritical annealing

The reaction following the IA step is the formation of bainite in the remaining carbon-enriched austenite. The mechanism of bainite formation has been actively debated for many years. The diffusional and diffusionless theories for bainite transformation will be described in chapter 3 (Carbide Free Bainitic steels) and will not be repeated in this chapter. This section focussed on the effect of the preceding IA treatment on the following bainite formation in TRIP steels.

It has been found that the IA treatment prior to bainite formation affects *(i)* the volume fractions of the grain and interphase boundaries, *(ii)* the local composition at the boundaries and *(iii)* the bulk composition of remaining austenite. The former two factors mainly affect the nucleation kinetics of bainite formation while the latter one affects both the nucleation and growth of bainitic ferrite. Ravi et al. [62] recently found that, even no ferrite formation takes place during IA, IA can still accelerate the overall kinetics of bainite formation. They claimed that the carbon segregation to austenite grain boundary is promoted during IA, which results in carbon-depleted zones in the near vicinity of austenite grain boundary and thus enhance the density of nucleation sites for bainitic ferrite. It has been reported [62, 63] that the presence of α/γ interfaces can accelerate the kinetics of bainite formation as the α/γ interfaces can serve as the nucleation sites for bainitic ferrite, which has been directly observed by Quidort and Brechet [64]. On the contrary, Zhu et al. [65] reported that the kinetics of bainite formation is decelerated by the preceding IA, which was attributed to the reduced driving force for bainitic ferrite nucleation at the α/γ interfaces enriched with austenite stabilizer elements. The α/γ interfaces can also be introduced through the ferrite-to-austenite transformation in the cold-rolled TRIP steels, which were also found to play a role in bainitic transformation [30, 66]. Dedicated experiments are required to comprehensively clarify the role of α/γ interfaces on the following bainitic transformation, which may provide useful guidance for the design of TRIP steels.

It will be clear that the amount of bainite formed not only depends on the steel composition and the IBT temperature and time, but also on the IA conditions. This interaction is captured in a recent integrated model for TRIP steel optimisation [44]. The model considers steel chemistry, intercritical ferrite (or austenite) formation and bainite formation (terminated by the occurrence of bainitic stasis as calculated by the NPLE/PLE concept, see chapter 3). A typical example of the predictions is shown in **Fig. 8** which shows the phase fraction as a function of the IA temperature for 4 sets of cold-rolled CMnSi steels with C levels ranging from 0.1 to 0.4 wt.% and both Mn and Si levels fixed at 1.2 wt.%. The IBT temperature is fixed at 400°C. M_s. As shown in **Fig. 8**, the model predictions are in good agreement with experimental data. The figure also shows that the balance between ferrite and bainite fraction is mainly determined by the IA temperature, and the RA volume fraction is dependent (for a given set of substitutional alloying element concentrations and a fixed IBT temperature) primarily on the nominal C concentration.

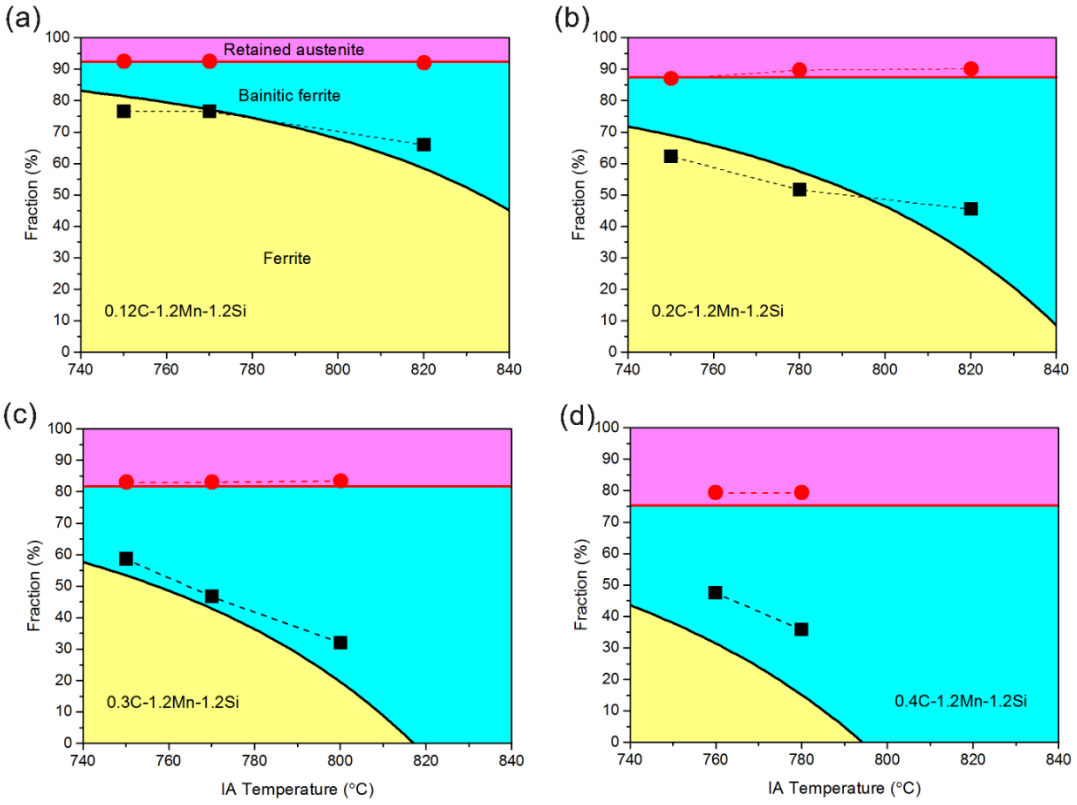

Fig. 8. The predicted ferrite, bainite and austenite fractions as a function of the IA temperature and a fixed IBT temperature of 400°C for 4 sets of Fe-*x*C-1.2Mn-1.2Si (in wt.%) cold-rolled steels [44].

As the model does not cover the actual microstructure formation, it cannot predict the size and C distribution of the austenite, nor does it predict the local environment in which these austenite grains are to be located. All these factors, especially the carbon concentration and the grain size, play a role in the thermal stability of austenite. It is very likely that the carbon concentration and the grain size between different austenite grains obtained after the IBT process in the same sample will not be the same, as the local transformation conditions depend on the local topologies and starting concentrations of both carbon and the substitutional alloying elements [67, 68]. This effect of compositional and volumetric variations between individual austenite grains on the overall thermal stability of austenite is generally overlooked [31, 32]. More dedicated characterisation techniques and realistic models are required to determine the dependence of compositional and volumetric variations between different austenite grains on bulk composition and processing parameters, and clarify their effects on the overall thermal stability of austenite.

3. Carbide-free bainitic (CFB) steels

3.1. Desired microstructures and require chemical composition

As already mentioned, the microstructures of TRIP steels contained 50~55 vol. % ferrite forming the continuous matrix, 30~35 vol. % bainitic ferrite, 7~15 vol. % RA and a very small amount of martensite [16]. However, the hardness difference between the ferritic matrix and bainitic ferrite (and/or martensite) negatively affects the stretch-flangeability and hole-expansion values of TRIP steels [69]. The bad stretch-flangeability has restricted the application of TRIP steels in automotive components. Given that the uniform fine lath microstructures of bainite is beneficial to the stretch-flangeability, it has been proposed to replace the ferritic matrix of TRIP steels by a matrix primarily consisting of lath bainitic ferrite, leading to the development of carbide-free bainitic (CFB) steels [70, 71]. CFB steels, which are also classified as TRIP-aided bainitic ferrite (TBF) steels [72] or super-bainitic TRIP steels [73], have a bainitic ferrite matrix with a certain amount of RA. The bainitic ferrite matrix has a high density of dislocations, which results in a higher yield strength than a ferritic matrix. Furthermore, the enhanced amount of (film-like) RA between the bainitic ferrite laths guarantees a superior balance of strength and elongation. As shown in **Fig. 9**, a typical microstructure of CFB steels consists of bainitic ferrite and film-like austenite with a thickness of ~0.2μm. Some (unintentional) blocky martensite/austenite (M/A) islands can also be observed.

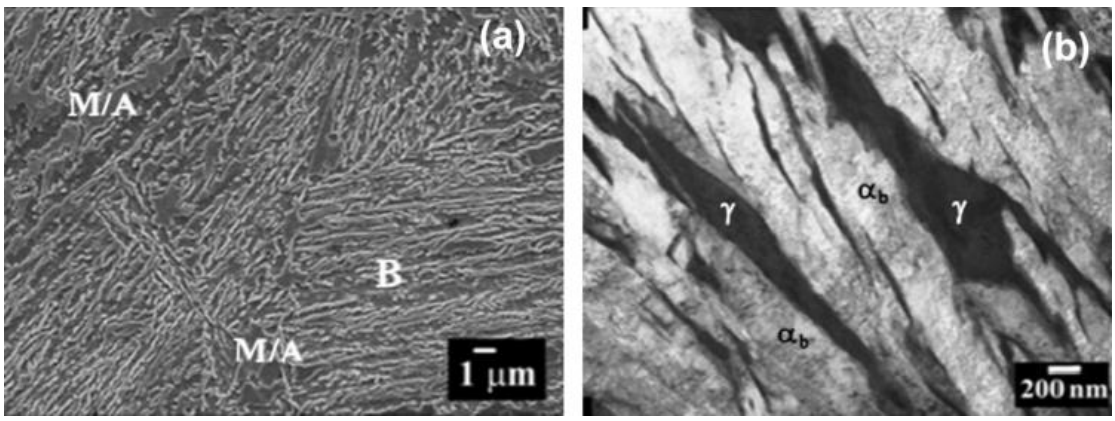

Fig. 9. (a) SEM and (b) TEM images of carbide-free bainitic microstructure [74]. B: bainite; M/A: martensite/austenite island; α_b: bainitic ferrite; γ: austenite.

Within the CFB steel family one can distinguish high carbon CFB steels and low/medium carbon CFB steels. The high carbon CFB steels proposed by Caballero and Bhadeshia et al. [75] have also been called nano-bainite steels. The carbon content in nano-bainite steels is usually higher than 0.7 wt.%, which not only makes these steels unweldable, but also leads to very slow bainite formation rates. As they have no real automotive applications, nano-bainite steels will not be discussed further in this review. However, low carbon CFB steels with a carbon content of 0.2~0.25 wt.% are promising materials for automotive applications. Being an important austenite stabilizer element, Mn is present in low/medium carbon CFB steels at concentration levels less than 2.5 wt.% to suppress ferrite/pearlite formation. Carbide or cementite precipitation would reduce the amount of carbon available to stabilize the austenite, and its presence in the microstructure could also promote crack and void formation [76]. 1.5 wt.% Si is usually added to further suppress cementite precipitation. The influence of the concentration of the principal alloying elements, C, Mn and Si, on the characteristics of the RA and the mechanical properties of representative Fe-C-Mn-Si CFB steels has been systematically investigated by Sugimoto et al. [72, 77, 78]. As in the case of TRIP, Q&P and medium Mn steels, Si addition is not good for surface coating and galvanizing behaviour and several studies have been performed to replace Si by Al in CFB steels [22, 79]. The replacement of Si by Al also increases the Bs temperature and accelerates the overall kinetics of bainite formation. Mo and Cr could be added in smaller quantities too [71, 74, 80-82].

3.2. Starting microstructures and processing routes

Like TRIP steels, CFB steels can be produced either from a hot-rolled or a cold-rolled starting condition [74, 82]. Given their relatively high Mn content (1.5~2.5 wt.%), Mn segregation bands are usually observed in the starting microstructure of CFB steels, which is expected to strongly affect the spatial distribution of the constituent phases and the mechanical properties [83]. However, after a proper homogenization and full austenisation treatment, the influence of the starting microstructure on phase transformations can be neglected, as in both starting conditions the actual processing usually starts from a fully austenitic and compositionally homogeneous starting state.

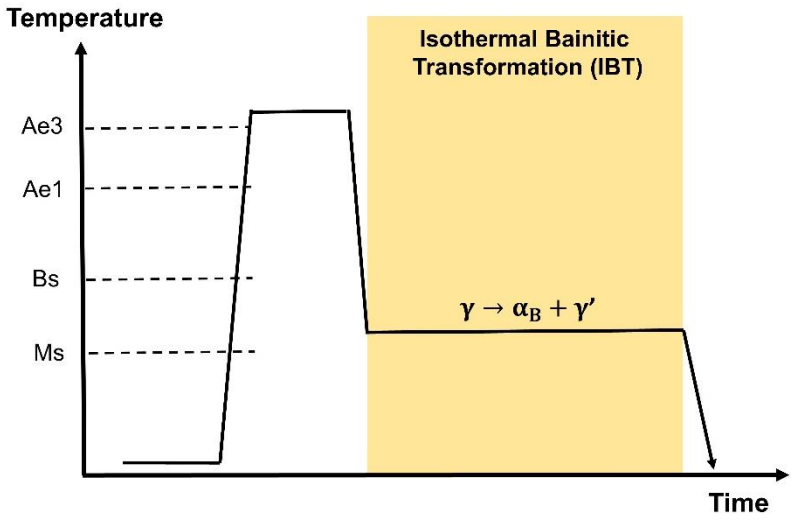

Fig. 10. Thermo-mechanical processing of CFB steels. α_B: bainitic ferrite; γ: austenite; γ': carbon-enriched austenite.

The typical heat treatment of CFB steels shown in **Fig. 10** consists of three steps: *(i)* a full austenisation step; *(ii)* an isothermal bainitic transformation (IBT) step, during which bainitic ferrite nucleates at prior austenite grain boundaries or at bainitic ferrite/austenite interfaces and then grows into the austenite. As a result, the prior austenite is retained as blocky or film-like austenite, and carbon partitioning from the bainitic ferrite into the untransformed austenite takes

place during the IBT; *(iii)* a final quenching step. Individual blocky austenite grains with a low carbon content and a suitable surrounding matrix could partially transform into fresh martensite [84, 85], leading to the formation of M/A islands.

In order to reduce the fraction of M/A islands and to refine the bainitic microstructures, several variants of the conventional IBT process, e.g. the two-step or multi-step IBT process [86-88], the continuous cooling process [71, 74, 80-82, 87, 89-92], the "disturbed" bainitic austempering (DBAT) [93] or the bainite-based quenching and partitioning (BQ&P) [94] process, have been proposed and explored. The two-step IBT process involves bainite formation first at a higher temperature and then at a lower temperature [86, 87]. The B_s and M_s temperatures of the remaining austenite decrease due to the carbon enrichment during the first bainitic holding step. Finer bainitic ferrite and more film-like RA are expected to be formed during the second bainitic holding step [87]. Bainite formation during a continuous cooling process was also found to be effective in refining the bainitic microstructures, and such a thermal path is desirable from an industrial production perspective. In order to reduce the fraction and size of blocky M/A islands, Gao et al. proposed the "disturbed" bainitic austempering (DBAT) [93] or the bainite-based quenching and partitioning (BQ&P) [94] processes, which combine aspects of the conventional IBT and the Q&P processes. In this approach the steel is first processed via the conventional IBT route, which leads to a microstructure consisting of bainitic ferrite, film-like austenite and blocky austenite. It is then quenched to a temperature between the M_s and M_f temperatures, during which the remaining blocky austenite is converted into film-like austenite via a partial martensitic transformation. Subsequently, the steel is reheated to a temperature allowing carbon partitioning from martensite into austenite, and the kinetics of the remaining bainite formation is accelerated due to the presence of the pre-existing martensite [95, 96] (see chapter 4 for a more extensive discussion on the role of the pre-existing martensite). The DBAT or BQ&P process leads to a

significant increase in the toughness and ductility of CFB steels, but greatly raises the complexity of the production route (and the production costs).

Summarising, the microstructure of CFB steels is mainly tuned via the bainite formation during a simple isothermal holding step. Recent progress in the understanding of the bainitic transformation is reviewed below.

3.3. Critical phase transformations

Isothermal bainitic transformation (IBT) is the most critical phase transformation in CFB steels, which to a large extent determines their final microstructures. Despite abundant efforts to solve the issue, the mechanism of bainitic transformation has been fiercely debated for decades [97-102] but in recent times we experience more signs of mutual appreciation and recognition. In this review, we will briefly discuss the mechanism of bainitic transformation with a focus on transformation stasis (or incomplete transformation phenomenon), which is of practical importance for the microstructural design of CFB steels. In general, there are two competing schools (diffusional and diffusionless), who explain the occurrence of the transformation stasis phenomenon in a different way.

The diffusionless school is of the opinion that the bainitic transformation initially proceeds in a displacive and diffusionless manner, similar to the martensitic transformation, rapidly followed by local carbon enrichment of the austenite around the bainite formed. However, the experimentally measured lengthening rate of bainitic ferrite is significantly slower than that for martensite. In order to explain this apparent discrepancy, Bhadeshia et al. [103] proposed that bainitic ferrite forms via nucleation and growth of the so-called "sub-unit", as indicated in **Fig. 11**. They assumed that bainitic ferrite nucleates under para-equilibrium conditions but that it grows in a diffusionless way. As long as the driving force for the nucleation of bainitic ferrite

is larger than the so-called universal nucleation barrier, sub-units nucleate at the prior austenite grain boundary and bainitic ferrite/austenite interfaces and the transformation proceeds. The temperature at which the sub-units start to form is called the T_h temperature. Bhadeshia and his co-workers [103] have experimentally observed the sub-units but other researchers were less successful. They assumed that the growth of individual sub-unit is arrested by plastic deformation within the surrounding austenite, and then new sub-units nucleate at its tip. The bainitic sheaf develops via nucleation and growth of the sub-units, and the average growth rate of a bainitic sheaf is expected to be much slower than that of sub-unit owing to delays between the formation of successive sub-units.

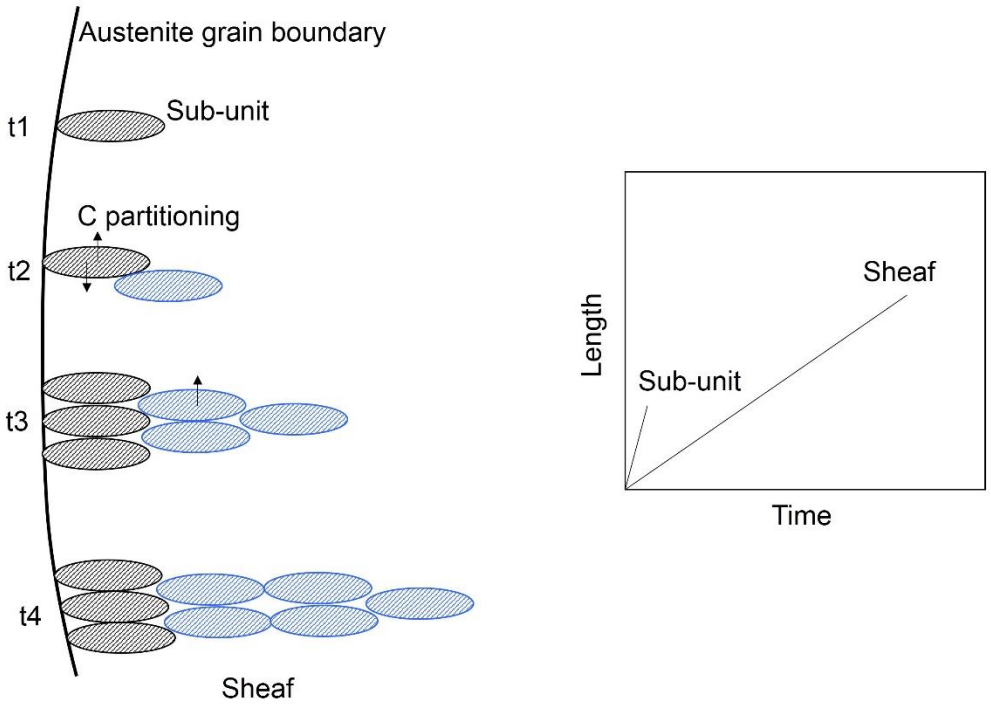

Fig. 11. Schematic illustration of the development of bainitic sheaf described by the diffusionless theory. Arrows indicate carbon partitioning from bainitic ferrite into austenite [104]. Time t1<t2<t3<t4.

With ongoing carbon partitioning from bainite into the surrounding austenite, the Gibbs free-energy of the austenite decreases and gradually approaches that of bainitic ferrite of the

same chemical composition, and the bainite formation should stop and reach a stasis state. The temperature at which the Gibbs energy of austenite is equal to that of bainitic ferrite of the same composition is called the T-zero temperature (T_0). Bhadeshia et al. [103] adopted the T_0 concept and later expanded it into a T_0' theory by adding a constant strain energy term (determined to be 400J/mol by fitting to a limited experimental dataset) to explain transformation stasis phenomenon. One would expect the value of the critical strain energy to depend on the actual mechanical properties of the austenite and the bainitic ferrite, and to change as a function of temperature and alloy composition. Therefore, the assumption of a constant strain energy value for all steel compositions does not seem very realistic. Caballero et al. [105-107] validated the applicability of T_0 or T_0' concept for incomplete bainitic transformation phenomenon in several nano-bainite steels by making a comparison between carbon content in RA measured by experiments and that predicted by the T_0 or T_0' theory. However, other studies [108-112] have indicated that the T_0 or T_0' predictions disagree with the experiments, but we agreed that both the uncertainty in the critical strain energy values and difficulties in the quantitative measurement of the carbon content in RA could also be responsible for the disagreement.

There are several diffusional theories to describe the incomplete bainitic transformation. One is a so-called Widmanstätten Bainite start (WBs) theory proposed by Hillert et al. [113, 114]. They suggested that the growth mechanism of bainitic ferrite is the same as that of Widmanstättern ferrite, and the start temperature of them can be described using one common WBs line. Here we will briefly explain how to obtain the WBs line. It was assumed that the lengthening rate of bainitic ferrite is controlled by carbon diffusion in austenite, and can be described by Zener-Hillert equation [113]:

$$\frac{v}{D} = \frac{(x^{\gamma/\alpha} - x_0)^2}{x_0} \cdot \frac{RT}{8\sigma V_m} \quad (4)$$

where v is the lengthening rate, D is the carbon diffusivity in austenite, $x^{\gamma/\alpha}$ is the carbon content in austenite at the bainitic ferrite/austenite interface, x_0 is the bulk carbon content, R is

the gas constant, T is the absolute temperature, σ is the interfacial energy and V_m is the molar volume of austenite. When the lengthening rate of bainitic ferrite in the binary Fe-C system was extrapolated to zero, it was found that the critical carbon content in austenite x_0 is lower than the equilibrium state $x_{eq}^{\gamma/\alpha}$. At this critical carbon content in the austenite, the driving force for the growth of diffusion-controlled acicular ferrite cannot overcome the energy barrier, and thus the transformation cannot proceed to the equilibrium state, leading to the incomplete transformation phenomenon. The critical carbon content x_0 in the binary Fe-C alloy as estimated by Hillert et al. through extrapolating the lengthening rate to the value of zero is shown in **Fig. 12a**. **Fig. 12b** shows the WBs line for the binary Fe-C alloy, which is located below the Ae_3 line but above the T_0 and T_0' lines. The WBs theory can also predict incomplete bainitic transformation although it has a completely different physical origin from that of the T_0 and T_0' lines.

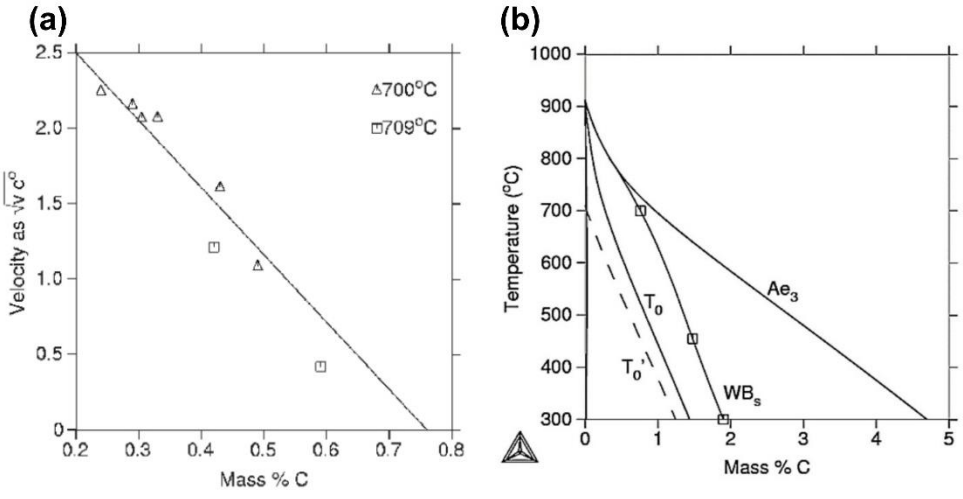

Fig. 12. (a) Lengthening rate as a function of the local C concentration in the binary Fe-C alloy at two temperatures. (b) The WBs line for the binary Fe-C alloy. Ae_3, T_0 and T_0' lines are plotted for a comparison [114, 115].

Based on the energy barrier estimated for the binary Fe-C alloys, Hillert et al. [114] further estimated the effects of alloying element (e.g. Mn, Ni, Si, Cr and Mo, etc) additions on the

magnitude of energy barrier. It was found that addition of austenite stabilizing elements such as Mn and Ni barely changes the energy barrier, but strongly affect the thermodynamic properties of bainitic ferrite and austenite. As a result, the WBs theory predicts that the critical carbon content in austenite shows a strong dependence on Mn content, which implies Mn content plays an important role in the degree of incomplete bainitic transformation. Unlike Mn and Ni, Cr and Mo have a stronger tendency to segregate to the interfaces, which would lead to a so-called solute drag effect and thus enhance the energy barrier. Si addition has no effect on the energy barrier in the WBs theory. Thus, it is predicted that the critical carbon content in austenite is only marginally affected by Si addition, which is also in agreement with experimental results.

Based on experimental data for the binary Fe-C, the ternary Fe-C-M (M = Mn, Ni, Cr and Mo) and the quaternary Fe-C-Mn-Si systems, Leach et al. [116] quantitatively estimated the effects of carbon and substitutional alloying elements contents on the WBs temperature:

$$WB_S(°\mathrm{C}) = 850 - 206w_C - 78w_{Mn} - 33w_{Ni} - 70w_{Cr} - 75w_{Mo} - 61w_{Si} \quad (5)$$

where w_i is in wt. %. The coefficients indicate clearly that the influences of Mn, Cr and Mo additions on the critical carbon content in austenite at a certain temperature are significant and greater than that of the Ni addition. Based on the Eq. (5), Leach et al. [117] further estimated the dependence of the energy barrier on temperature, carbon and substitutional alloying elements contents. The influence of temperature on the energy barrier in the binary Fe-C system as analysed by Leach et al. [117] was found to be smaller than that estimated by Hillert et al. [114] while the effects of Mn, Ni, Mo and Cr additions on the energy barrier estimated by both researchers are similar. However, unlike the Hillert et al.'s predictions [114] Si addition was now predicted to strongly affect the critical carbon content in austenite, as well as the energy barrier. We suggest that the effect of Si addition on the energy barrier and the critical carbon content may have been overestimated by Leach et al. [117] since *(i)* The effect of Si addition

on the bainite start temperature was found to be marginal [118, 119]; *(ii)* Wu et al. [120] reported that the carbon content in RA in the ternary Fe-0.4C-1.5/3.0Si alloys measured using 3DAPT is in good agreement with the WBs theory [114], i.e. Si addition has a marginal effect on the energy barrier; *(iii)* The effect of Si addition on the carbon content in RA in the quaternary Fe-C-Mn-Si alloy was experimentally found to be negligible [78].

Another diffusional theory for bainite formation is the solute drag theory proposed by Aaronson et al. [99, 121]. Aaronson et al. [122] suggested that there is no essential difference between pro-eutectoid ferrite and bainitic ferrite, both of which can be regarded as the transformation products resulting from a competitive behaviour of eutectoid decomposition. Aaronson et al. [99, 121] proposed a so-called coupled solute drag model, in which the attractive interaction between carbon and substitutional atoms partitioned at the interface was considered to affect the carbon activity near the interface and this decelerates the kinetics of bainitic transformation. The coupled solute drag theory has been applied by Reynolds et al. [123] and Goldenstein and Aaronson [124] to qualitatively explain the incomplete bainitic transformation in the ternary Fe–C–Cr and Fe–C–Mo systems.

Inspired by the coupled solute drag concept, Chen and Van der Zwaag [125-129] proposed a so-called Gibbs Energy Balance (GEB) model to quantitatively predict the transformation stasis for both bainite and ferrite formation in ternary and quaternary alloys. In the GEB model, it is assumed that the stasis state occurs when the chemical driving force cannot overcome the maximum dissipation of Gibbs energy due to solute diffusion inside interface. The dissipation of Gibbs energy due to diffusion inside interface was estimated using the solute drag model [130]. As shown in **Fig. 13a**, the dissipation of Gibbs energy due to diffusion inside the interface is composed of two parts, i.e. the dissipation due to solute drag effect and the dissipation due to the alloying element spike. The dissipation is strongly dependent on interface velocity which determines the segregation/partitioning behavior at the interface. **Fig. 13b** shows that the solute

diffusion profile inside the interface is strongly dependent on the interface velocity. At a relatively high interface velocity, the growth of bainitic ferrite occurs under the paraequilibrium condition while at a low interface velocity it occurs with solute diffusion inside the interface. A typical GEB diagram for an Fe-0.1C-3.0Mn alloy at 500°C, which shows the balance between chemical driving force and dissipation, is presented in **Fig. 14.** The intersection between chemical driving force and dissipation curves gives the lengthening rate of bainitic ferrite. With bainitic transformation proceeding, the carbon content in austenite increases, which reduces the chemical driving force for the growth of bainitic ferrite. It is predicted in **Fig. 14,** when the fraction of bainitic ferrite is lower than 0.75, the lengthening rate of bainitic ferrite is very high and controlled by carbon diffusion. When the fraction of bainitic ferrite is higher than 0.75, the lengthening rate is controlled by Mn diffusion inside the interface and dramatically decreases to a very low value, e.g. the transformation reaches a stasis state. Based on the Gibbs energy balance between the chemical driving force and the dissipation, there is a complex kinetic transition from the fast Paraequilibrium (PE) mode to the sluggish Negligible Partitioning (NP) mode during isothermal bainitic transformation, as described in [128].

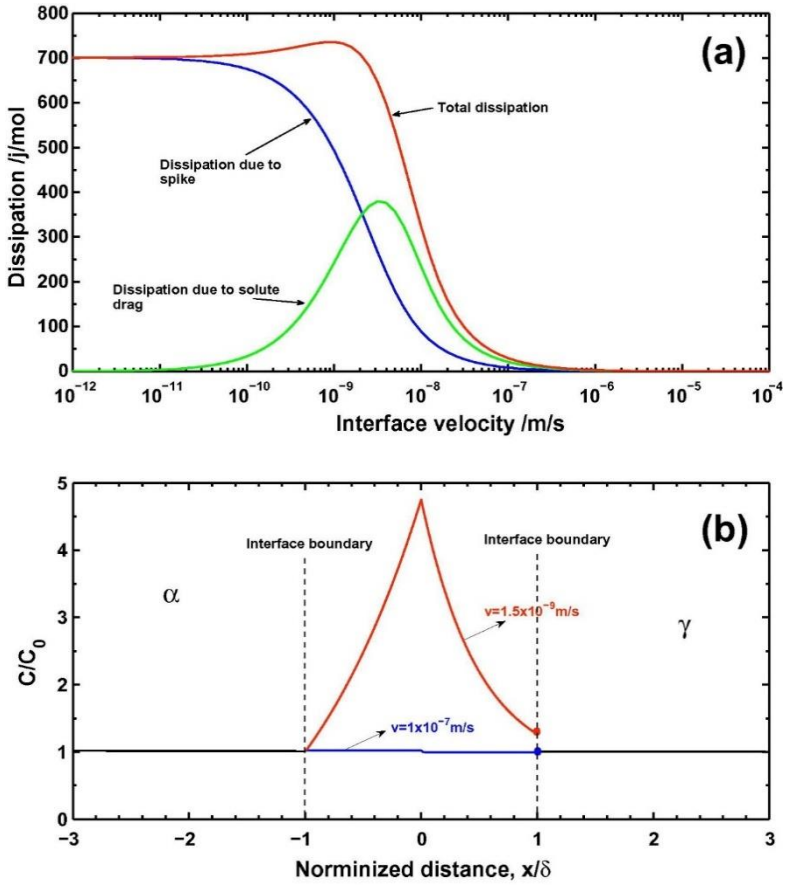

Fig. 13. (a) The total energy dissipation, dissipation due to the spike and dissipation due to the solute drag effect as a function of interface velocity for the ternary Fe-0.1C-3Mn steel at 550°C. (b) The normalized Mn profiles inside the bainitic ferrite/austenite interface for two different interface velocities [127].

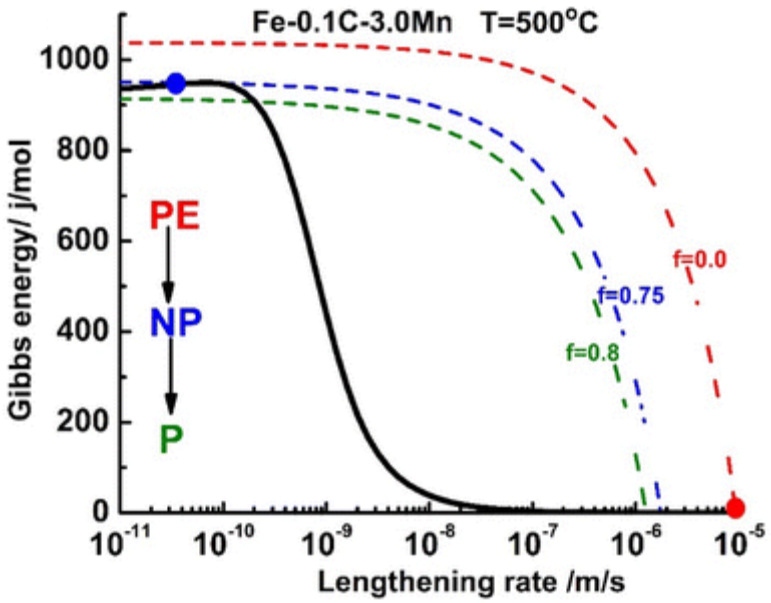

Fig. 14. The chemical driving force and total dissipation for the ternary Fe-0.1C-3.0Mn alloy at 500°C [128]. PE: paraequilibrium; NP: Negligible partitioning; P: Partitioning. f: Volume fraction of bainitic ferrite.

The degree of incomplete transformation as a function of the alloy composition and the temperature for ternary Fe-C-M (M=Mn, Ni, Si, Mo) alloys was well predicted by the GEB model [127, 129]. The GEB model predicts that the bainitic ferrite fraction at the stasis state is strongly affected by the Mn content while it is marginally affected by the Si content. It was found in [127, 129] that the strong dependence of bainitic ferrite fraction at the stasis on Mn content and temperature in the Fe-C-Mn and Fe-C-Mn-Si alloys can be well captured by the GEB model, while the T_0' model (and the PE model) only predicts the correct stasis fraction for one Mn concentration.

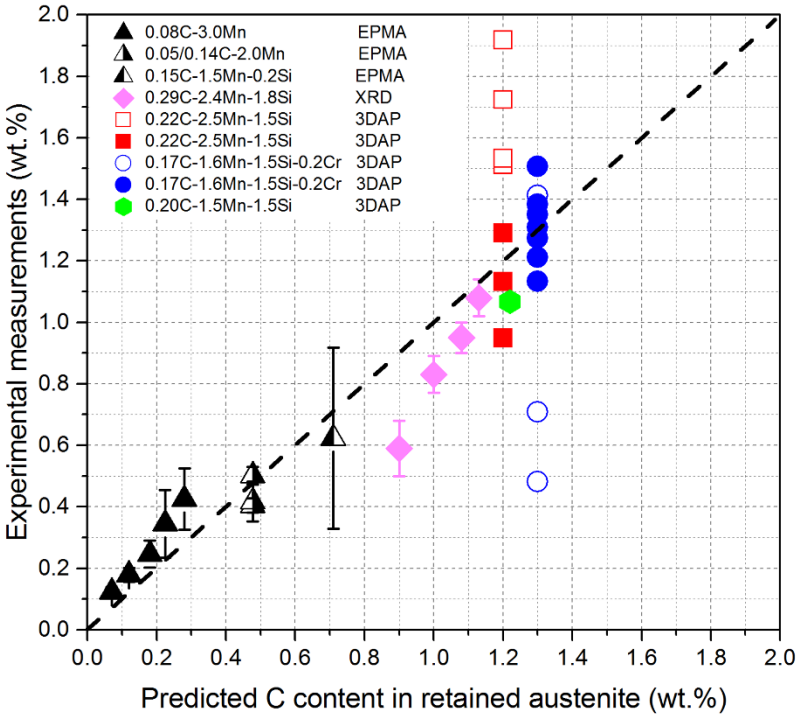

Fig. 15. Comparison between the carbon content in RA measured by different experimental technology and predicted by the NPLE/PLE concept [44].

For the Fe-C-Mn and Fe-C-Mn-Si systems, the GEB model predicts that the incomplete transformation stage is reached when the growth mode switches from PE into NP. In the NP mode, the dissipation of Gibbs energy is mainly attributed to the Mn spike development in the Fe-C-Mn and Fe-C-Mn-Si alloys, which implies that the simple NPLE/PLE concept should be applicable to those alloy systems. Dai et al. [44] found that the RA fraction and its carbon content for a series of Fe-C-Mn and Fe-C-Mn-Si steels containing different Mn contents can be well predicted by the NPLE/PLE concept, as shown in **Fig. 15**. It is worth noting that the carbon content in RA grains as measured using 3DAPT in a Fe-0.17C-1.6Mn-1.5Si-0.2Cr steel is much larger than that predicted by either the T_0 or T_0' theory [131]. Similarly, Wu et al. [120] observed that carbon content in untransformed austenite in the ternary Fe-0.4C-(1.5, 3) Si alloys is also much larger than that predicted by the T_0 and T_0' lines.

As mentioned above, the incomplete bainitic transformation in the Fe-C-M and Fe-C-Mn-Si systems can be explained by one or more theories. However, Xia et al. [111] found a unique experimental result on the incomplete transformation phenomenon in the quaternary Fe-0.1C-1.5Mn-(0, 0.03, 0.3, 0.5, 1) Mo alloys. They reported that, based on the carbon content in untransformed austenite as measured using Electron probe microanalysis (EPMA), the transformation barrier is estimated to be strongly dependent on the Mo content, which dependence is not included in the T_0' theory. The value of transformation barrier is also larger than that estimated by both the WBs and solute drag theories. Furthermore, Furuhara et al. [109] found that for an Fe-0.15C-1.5Mn-0.5Mo alloy at the beginning of stasis a small amount of Mn atoms had segregated to the interface while Mo atoms had not accumulated significantly at the interface. The above experiments for the Fe-C-Mn-Mo systems seem to be against the solute drag theory. In order to explain the above experiments, Sun et al. [132] argued that the bainitic stasis is controlled by the evolution of the derivative of total dissipation with the interface velocity, $\frac{\partial \Delta G^{total-diss}}{\partial v}$, instead of the absolute magnitude of the total dissipation, $\Delta G^{total-diss}$. The simulation results show that the kinetics of carbon diffusion in austenite is slow while carbon concentration in austenite at the interface changes quickly. When a local carbon profile inversion near the interface occurs, the transformation stasis is attained. Simulation results by Sun et al. [132] showed that both the coupled solute drag effect and the interface friction play an important role in the total energy dissipation. Using this fact, the dependence of bainitic ferrite fraction on Mo content and temperature in the Fe-0.1C-1.5Mn-*x*Mo alloys could be well explained.

In summary, the T_0', the WBs and the GEB models all can explain the incomplete bainitic transformation qualitatively, even though the physical origin of these models are different. In the T_0' theory, the energy barrier for the growth of bainitic ferrite is related to the transformation strain. In the WBs theory, the energy barrier is considered as a resistance to the movement of

bainitic ferrite/austenite interface, which could be due to interface friction, transformation strain, accumulation of dislocations, solute drag, etc. [133]. The GEB model argues that the stasis should be attributed to the dissipation of Gibbs energy due to solute diffusion inside the interface. More dedicated experiments and/or alternative characterisation techniques are required to better understand the mechanism of incomplete bainitic transformation.

Furthermore, although the incomplete bainitic transformation has been extensively investigated for engineering steels in general, only few investigations were made specifically for Fe-C-Mn-Si/Al based automotive CFB steels [22, 73, 134]. While the GEB model does not capture any of the crystallographic features of the bainite formed, out of the existing models it seems to capture the compositional and transformation temperature dependence best and can be used to guide the optimisation of the composition and processing temperature of CFB steels.

4. Quenching and partitioning (Q&P) steels

4.1. Desired microstructures and required chemical composition

Quenching & Partitioning (Q&P) is a novel heat treatment to obtain a considerable amount of RA in AHSSs having a (tempered) martensitic microstructure. The route dates from a key publication by Speer et al. [10]. The Q&P concept was originally proposed for automotive steels, but at later stages has been extended to other types of steels, such as ultrahigh strength steels [135], nanobainite steels [96, 136] and stainless steels [137-139]. These latter steels are outside the scope of this review. The typical microstructure of Q&P steels shown in **Fig. 16a** consists of a martensitic matrix containing a significant amount of carbon enriched RA. The RA can be of a blocky type or be film-like. The ultrafine martensite laths with a high density of dislocations can provide superior strength in comparison to the bainitic ferrite matrices in TRIP steels and CFB steels. As for the TRIP and CFB steels the RA improves both the strength and elongation due to it transforming to fresh martensite upon deformation. In commercial Q&P steels, some soft ferrite may also be present to optimize the formability and elongation. **Fig. 16b** and **c** show the microstructures of commercial QP980 and QP1180 grades produced by Baosteel. Generally, the tensile strength value decreases significantly when the ferrite fraction increases.

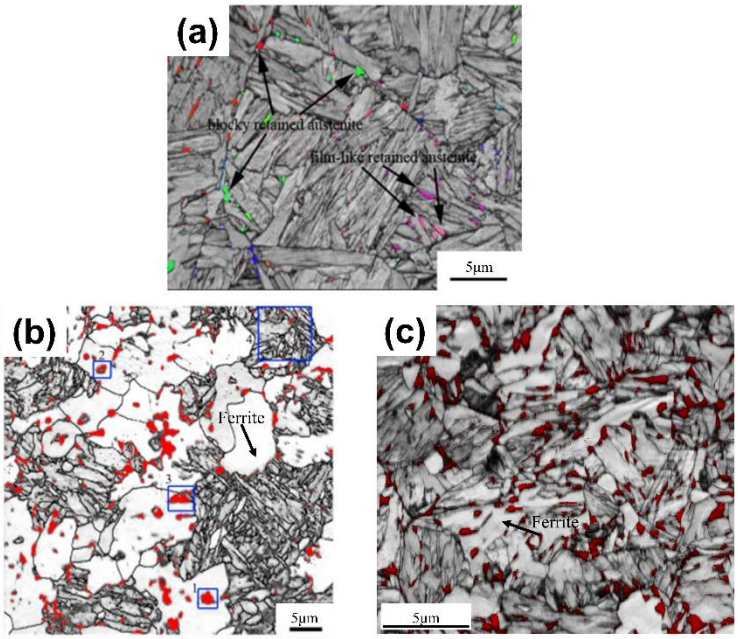

Fig. 16. EBSD images of (a) typical Fe-0.20C-1.57Mn-1.55Si Q&P steels [140], commercial (b) Fe-0.22C-1.80Mn-1.40Si Q&P980 steels [141] and (c) Fe-0.18C-2.8Mn-1.3Si Q&P1180 steels. Colored phases in (a) and red phases in (b) and (c) represent RA.

The key alloying elements in typical Q&P steels are C, Mn, Si, while other elements could also be added for different purposes. Conventional Q&P steels usually contain about 0.18~0.5 wt.% C. A higher C content is likely to increase the fraction of RA, while it could also promote the formation of brittle twin martensite and lead to a decrease in (spot) weldability. Typically, 1.5~2.5 wt.% Mn is present to tailor the hardenability. Usually about 1.5 wt.% Si is added to suppress the formation of cementite and promote carbon partitioning into austenite, and this element could also enhance the strength of the ferrite/martensite matrix via solid solution strengthening. However, Si addition was found to deteriorate the galvanizability of such steels [142]. Al could also be added to suppress cementite precipitation and to maintain galvanizability [142]. As a strong ferrite stabilizer, Al addition reduces the hardenability. Cr is also frequently added into Q&P steels as it was found to be effective in stabilizing the austenite during partitioning [93, 94, 143-147]. In order to further enhance the strength of Q&P steels,

micro-alloying elements, such as Nb, V, Ti and Mo, are added to form nano-precipitates [148, 149]. The composition ranges of the automotive Q&P steels have been reviewed by De Moor and Speer [150] and Jin et al. [149]. In general, the compositions of Q&P steels do not differ much from those of TRIP and CFB steels.

4.2. Starting microstructures and processing routes

Given their composition, the starting microstructure of Q&P steels is usually a mixture of ferrite and pearlite, while some Q&P steels with a higher C or Mn content could also contain a certain amount of martensite. The starting microstructure of Q&P steel, either in a hot-rolled state or a cold-rolled state, is expected to affect the characteristics of austenite formed during the austenisation step, which would definitely play a significant role in phase transformations and microstructure evolution during the subsequent Q&P process. Mn segregation bands have frequently been observed in the starting microstructure, which is expected to affect the final microstructure of Q&P steels as the phase transformations and the carbon partitioning behaviour are strongly dependent on the local Mn content [151, 152].

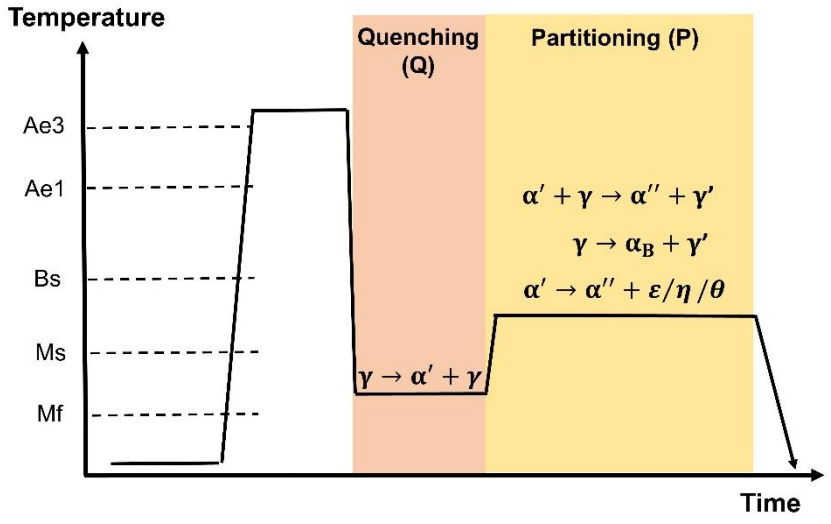

Fig. 17. Thermo-mechanical processing of Q&P steels. α': un-tempered martensite; α'': tempered martensite; α_B: bainitic ferrite; γ: austenite; γ': carbon-enriched austenite; ε/η: transition carbides; θ: cementite.

The original Q&P process shown in **Fig. 17** consists of four steps: *(i)* the austenisation step, during which the steel is either fully or partially austenitic. The characteristics of the austenite (uniformity of chemical composition, morphology and grain size, spatial distribution etc.) formed in this step can be tailored via the initial microstructure [153, 154], the heating rate [155, 156], the annealing temperature [156-162], the annealing time [156] and thermo-mechanical processing technologies [156, 163, 164]; *(ii)* the quenching step, during which the steel is quenched from the fully or partially austenitic state to a temperature between the M_s and M_f temperatures. Aim of this part of the Q&P treatment is to get a fine and spatially homogeneous martensite-austenite mixture or martensite-austenite-ferrite mixture; *(iii)* the partitioning step, during which the steel is kept at the quenching temperature (one-step Q&P) or at a higher temperature often selected to be above the M_s (two-step Q&P) to facilitate carbon partitioning from the martensite into the austenite, while keeping the martensite volume fraction more or less constant. Apart from carbon partitioning into the remaining austenite, other kinds of phase transformations can also occur during the partitioning step; *(iv)* the final cooling step, during which additional martensite formation is to be avoided as fresh martensite would reduce the ductility of the steels.

Several variants of the original Q&P process, e.g. stepping-quenching and partitioning (S-Q&P) [165], quenching-partitioning-tempering (Q&P-T) [148, 166], quenching-tempering and partitioning (Q-T&P) [167, 168] and Quenching and flash-partitioning (QFP) [169], have been proposed and explored more recently. During the S-Q-P process, the steels are repeatedly quenched to a final temperature between M_s and M_f while the carbon is partitioned at a higher

temperature [165]. After several thermal cycles, blocky austenite with a lower carbon content is divided into film-like austenite by martensite lath and thus a refined microstructure is obtained. In all Q&P variants, carbide precipitation is usually to be prevented as the formation of carbides would reduce the amount of carbon available for the partitioning process. Hsu et al. [148] proposed a novel quenching-partitioning-tempering (Q&P-T) process to enhance the matrix strength via formation of nano-precipitates, e.g. NbC and VC, in the tempered martensitic matrix. The method certainly works but requires an even tighter control of the partitioning temperature and time. Yi et al. [167, 168] proposed a Q-T&P process, in which the initial quenching temperature is fixed at ambient temperature. In order to ensure the ambient temperature is located between martensite start temperature and martensite finish temperature, the alloying composition or intercritical annealing process must be tailored carefully. For the Q&P variants mentioned above, the carbon partitioning and martensite formation is decoupled. However, once the martensitic lath is formed, carbon partitioning from the supersaturated martensite lath to the neighbouring untransformed austenite could possibly occur just after the martensite formation took place [170-172]. Recently, Yi and his co-workers [169] proposed a novel Quenching and flash-partitioning (Q&FP) concept to allow dynamic carbon partitioning from martensite into austenite as martensite formation proceeds during the press-hardening process. In order to ensure carbon flash-partitioning occurs during continuously cooling, a considerable amount of Si is added to retard cementite precipitation while a smaller amount of Mn is added in order to have a relatively higher M_s temperature.

Assuming a regular equiaxed austenite grain structure is formed during the austenisation step, the final microstructure of Q&P steels is mainly tuned via phase transformations during the subsequent Q&P process, as shown in **Fig. 17**. Extensive studies have been performed to investigate the influence of processing parameters, e.g. quenching temperature [145, 173-175], partitioning temperature [174, 176] and partitioning time [174, 175, 177], as well as alloying

elements additions on the phase transformations in Q&P steels. The fundamentals of the key phase transformations during the conventional Q&P process are reviewed below.

4.3. Critical phase transformations

4.3.1. Martensite formation during quenching

A major benefit of the Q&P process over the bainite formation process in TRIP and CFB steels is that the formation of the martensitic matrix and the carbon partitioning from the martensite into the remaining austenite are separated via the quenching and partitioning steps, respectively. The martensite formation upon quenching definitely affects the microstructure evolution during the following partitioning process. Hence, a precise control of the martensite formation is of great importance for Q&P steels.

4.3.1.1. Martensite start temperature

The martensite start temperature (M_s), being a critical physical parameter in the martensite formation, is strongly affected by the chemical composition of the austenite present at the start of the quench. As the austenite grain size is relatively large (typically d_γ > 10 μm), the actual grain size does not play an important role in setting the conditions for the martensitic transformation. In principle, from a thermodynamic point of view, the diffusionless martensitic transformation is expected to occur when the temperature is brought to a value below T_0. T_0 is the critical temperature, at which FCC and BCC phase of the same (i.e. nominal steel) composition have the same Gibbs free energy. However, due to various additional transformation barriers (mainly related to the accommodation of the elastic strain as a result of the volumetric expansion), martensite formation generally occurs at a temperature lower than T_0. The chemical driving force at the highest temperature at which martensite can form, the

martensite start temperature, M_s, equals this energy barrier B, and thus the M_s can be determined by:

$$\Delta G^{\gamma\rightarrow\alpha'} = -B \quad (6)$$

When assuming the martensite as a carbon-supersaturated ferrite, i.e. excluding the effects of local ordering of the carbon, the chemical driving force $\Delta G^{\gamma\rightarrow\alpha'}$ can be calculated by the difference between the Gibbs free energy of austenite and (cubic) carbon-supersaturated ferrite of the same composition. Taking the effect of carbon ordering in tetragonally distorted martensite into account, Fisher [178] modified the Gibbs free energy expression of martensite and found that carbon ordering leads to an increase in the $\Delta G^{\gamma\rightarrow\alpha'}$ value.

While the thermodynamic driving force is relatively easy to calculate, it is more challenging to estimate the value of the transformation barriers. Hsu and Chang [179] were the first to estimate the energy barrier for the binary Fe-C system by taking into account the temperature-dependent shear strain energy and the solute-solution strengthening effect of carbon. Later, the analysis of energy barrier was extended to the ternary Fe-C-M systems [180]. For the multicomponent systems, Ghosh and Olson [181] estimated the energy barrier based on a model for heterogeneous martensitic nucleation. In the Ghosh-Olson model, it is assumed that the martensite interface is generated by the dissociation of an array of pre-existing dislocations, which leads to a transformation strain. Apart from the interaction between the alloying elements and the martensitic interface the presence of a long-range stress field leads to an increased energy barrier for martensite formation. The energy barrier was suggested by Ghosh and Olson as follows:

$$B = K_1 + W_F^{SS} \quad (7)$$

where K_1 accounts for the fault energy and shear strain energy, and W_F^{SS} is the solid solution friction work. K_1 is a constant as the shear module and interfacial energy are assumed to be not or only weakly dependent on temperature and composition. It has been reported that the friction

stress due to solid solution hardening is approximately proportional to the square-root of alloying element concentration, and thus the solid solution friction work was given by:

$$W_F^{SS} = \sqrt{\sum_i (K_\mu^i x_i^{0.5})^2} + \sqrt{\sum_j (K_\mu^j x_j^{0.5})^2} + K_\mu^{\mathrm{Co}} x_{\mathrm{Co}}^{0.5} \quad (8)$$

where $x_{i\ or\ j}$ is the concentration of element i or j (i represents C and N; j represents Mn, Si, Cr, Ni, Mo, Nb, V, Ti, Cu, W and Al), and K_μ is a constant coefficient accounting for the solute-solution strengthening effect of additional elements. The parameters K_1 and K_μ were obtained by fitting model predictions with experimental data. The uncertainty of M_s predicted by the Ghosh and Olson's model was within ±40°C. Later Ghosh and Olson [182, 183] further modified the solid solution friction work by considering the dependence of the shear modulus μ on composition and temperature via:

$$W_F^{SS} = A_\mu \mu(x_i, T) \quad (9)$$

$$A_\mu = \sqrt{\sum_i (k_\mu^i x_i^{0.5})^2} + \sqrt{\sum_j (k_\mu^j x_j^{0.5})^2} + k_\mu^{\mathrm{Co}} x_{\mathrm{Co}}^{0.5} \quad (10)$$

where the value of the parameter k_μ was optimized via fitting with experimental data.

Unlike the Ghosh-Olson model, Stormvinter et al. [184] proposed a thermodynamic model to describe the energy barrier, which was expressed as the interaction between the various alloying elements and the interstitial carbon atom. The thermodynamic interaction parameters were evaluated by Stormvinter et al. [184] from experimental databases based on a number of binary Fe-M (M=C, Cr, Mn and Ni) systems. The uncertainty of M_s for the total of 180 commercial steels predicted by the Stormvinter et al. model was within ±23°C, which is better than the Ghosh-Olson model prediction [181, 184].

Recently Galindo-Nava [185] assumed that the energy barrier is equal to the total strain energy caused by the atomic shear displacement and the substitutional/interstitial lattice distortions. In the Galindo-Nava model, the strain energy is strongly affected by the composition itself and the composition and temperature dependence of the shear modulus.

Unlike the Ghosh-Olson model [181] and the Stormvinter et al. model [184], there are no fitting parameters in the Galindo-Nava model. The differences between the experimental data and the M_s values predicted by the Galindo-Nava model for the Fe-M (M= Ni, Mn, Cr, Co) systems were within a range of ±50°C while the predictions for the Fe-C and Fe-N systems were accurate up to ±30°C.

In addition to the reported compositional effects, for small grain sizes ($d_\gamma < 10$ μm) the M_s can also be affected by the austenite grain size [186-189]. Jimenez-Melero et al. [188] were the first to quantitatively determine the contribution of smaller austenite grain size to the decrease of M_s. Since the specific surface area increases with decreasing equiaxed austenite grain size, it was suggested that the energy barrier related to the interfacial energy would increase for a smaller austenite grain size if the equiaxed austenite grain transforms into martensite completely. Compared with the austenite grains with a relatively large size, the decrease of M_s for austenite grains with a smaller size can be given by $-AV_\gamma^{-1/3}$ [188]. The proportionality factor A is related to the change in the interfacial energy due to martensite formation and V_γ is the transforming spherical austenite grain volume. Recently, Van Bohemen and Morsdorf [189] analysed in detail the influence of the austenite grain size on the energy barrier for martensite formation from other two perspectives:

(i) The yield strength of austenite depends on its grain size as predicted by the Hall-Petch relation and a higher yield strength induces an extra barrier for martensite formation. The decrease in M_s due to the enhanced yield strength of parent austenite was found to be proportional to ${d_\gamma}^{-0.5}$ [190], where d_γ is the average grain size. As the change in energy barrier scales linearly with a change in M_s, the increased energy barrier can be estimated as: $W_{HP} = K_{HP}{d_\gamma}^{-0.5}$, in which K_{HP} is a proportionality factor.

(ii) The aspect ratio *c*/*a* of martensite lath increases when the austenite grain size is below a

critical value of $d_\gamma^C = 15\mu m$. The change of martensite lath morphology would introduce an additional energy barrier $W_C = K_C \exp(-6d_\gamma/d_\gamma^C)$, in which K_C is a proportionality constant.

By considering the effects of both composition and austenite grain size, Van Bohemen and Morsdorf [189] derived a new model for calculating the energy barrier and M_s for martensite formation. The model was found to predict the M_s of 121 steels (0.1~0.7 wt.% C, <3 wt.% Mn, <2 wt.% Si, <3 wt.% Cr, <1 wt.% Mo and <5 wt.% Ni, d_γ>6μm) with an accuracy of ± 7°C.

Based on the geometric partitioning concept that the volume fraction of newly formed martensite is proportional to the average volume of untransformed austenite grain [191], Yang and Bhadeshia [192] also estimated the effect of austenite grain size on the M_s and derived the following expression

$$M_s = M_s^0 - \frac{1}{b}\left[\frac{1}{aV_\gamma}\left\{\exp\left(-\frac{\ln(1-f)}{m}\right) - 1\right\} + 1\right] \quad (11)$$

where M_s^0 is the martensite start temperature corresponding to infinite prior austenite grain size, m=0.05 is the aspect ratio of the martensite plate, V_γ is the average volume of austenite grain, a and b are fitting parameters, f is the first detectable martensite fraction. Unlike the Jimenez-Melero et al. model [188] and the Van Bohemen-Morsdorf model [189], the Yang-Bhadeshia model lacks a clear thermodynamic basis. Adopting the Yang-Bhadeshia equation, Lee and Park [193] proposed an empirical equation including the effects of composition and prior austenite grain size to predict the M_s for the steels (0.1~1.0 wt.% C, 0.17~1.91 wt.% Mn, <0.38 wt.% Si, <2.42 wt.% Ni, <2.28 wt.% Cr, <1.96 wt.% Mo, <0.2 wt.% Cu, d_γ=7~255μm) with an accuracy of ±20 °C.

Although the thermodynamic models are physically clear, it is sometime challenging to calculate M_s due to a lack of proper data for the temperature and composition dependence of the shear modulus and the shear strain. Alternatively, many empirical formula for M_s have been

derived using various fitting protocols, e.g. linear regressions [194, 195], non-linear regressions [118, 196], artificial neural network [197, 198], machine learning [199, 200]. The most popular empirical equations of M_s as a function of alloying composition and/or grain size have been compared with each other and summarized by many researchers [118, 193, 196].

4.3.1.2. Temperature dependent martensite formation

In order to precisely control the microstructure of Q&P steels, it is also required to predict the kinetics of martensitic transformation. The martensite fraction as a function of the undercooling is usually described by the Koistinen-Marburger (K-M) equation, which was originally a very empirical model [201]. Taking into account the nucleation and growth of martensite laths, Magee [202] was the first to derive a physical justification for the K-M equation. It was assumed by Magee that the total number of newly formed martensite laths dN (all assumed to have a fixed volume Ω) is proportional to the increased chemical driving force for martensite formation due to a decrease of temperature:

$$dN = -\varphi d(\Delta G^{\gamma\rightarrow\alpha'}) \quad (12)$$

where φ is a proportionality constant. The increased fraction of martensite is described by:

$$df_m = \Omega(1-f_m)dN = -\varphi\Omega(1-f_m)\frac{d(\Delta G^{\gamma\rightarrow\alpha'})}{dT}dT \quad (13)$$

where $(1-f_m)$ is the remaining austenite fraction available for martensite formation. By integrating from M_s to T yields:

$$f_m = 1-\exp[-\alpha\cdot(M_s-T)] \quad (14)$$

$$\alpha = \varphi\Omega\frac{d(\Delta G^{\gamma\rightarrow\alpha'})}{dT} \quad (15)$$

Using experimental data for the binary Fe-C system a value for α of 0.011 was derived by Koistinen and Marburger [201]. The K-M equation with a constant α=0.011 and M_s values as suggested by the Andrew equation [195] was used by Speer et al. [203] to predict the martensite

fraction as a function of the quenching temperature in Q&P steels. However, extensive experiments showed that the parameter α is dependent on chemical composition, especially the carbon content. Van Bohemen and Sietsma [204] proposed a modified K-M equation (VB-S equation), in which the expressions for α and M_s were assumed to be linear functions of carbon and alloying element concentrations:

$$\alpha(\times 10^{-3}\mathrm{K}^{-1}) = 22.4 - 10.7x_{\mathrm{C}} - 0.7x_{\mathrm{Mn}} - 0.12x_{\mathrm{Cr}} - 0.05x_{\mathrm{Ni}} - 0.1x_{\mathrm{Mo}} \quad (16)$$

$$M_s = 462 - 273x_{\mathrm{C}} - 26x_{\mathrm{Mn}} - 13x_{\mathrm{Cr}} - 16x_{\mathrm{Ni}} - 30x_{\mathrm{Mo}} \quad (17)$$

The VB-S equation can quantitatively predict the martensite fraction as a function of the quenching temperature for steels containing 0.3~1.1 wt. % C and Ni, Cr, Mn and Mo levels typically less than 3%. Van Bohemen [118] further proposed a modified K-M equation (VB equation), in which the expressions for α and M_s were assumed to be an exponential function of the carbon content and a linear function of the concentrations of the substitutional alloying elements:

$$\alpha(\times 10^{-3}\mathrm{K}^{-1}) = 27.2 - 19.8[1 - \exp(-1.56x_{\mathrm{C}})] - 0.14x_{\mathrm{Mn}} - 0.21x_{\mathrm{Si}} - 0.11x_{\mathrm{Cr}} - 0.08x_{\mathrm{Ni}} - 0.05x_{\mathrm{Mo}} \quad (18)$$

$$M_s = 565 - 600[1 - \exp(-0.96x_{\mathrm{C}})] - 31x_{\mathrm{Mn}} - 13x_{\mathrm{Si}} - 10x_{\mathrm{Cr}} - 18x_{\mathrm{Ni}} - 12x_{\mathrm{Mo}} \quad (19)$$

The VB equation can quantitatively predict the martensite fraction as a function of the quenching temperature for steels with a composition in the range of 0.1~1.9 wt. % C and a total of substitutional alloying elements less than 7 wt. %.

The K-M equation predicts a C-shaped curve for the martensite fraction as a function of temperature, while the experimentally measured martensite fraction as a function of temperature usually has a sigmoidal shape. In order to better predict the temperature dependence of the martensite fraction, another parameter β was introduced into the K-M equation by Lee and Van Tyne (L-VT equation) [205]:

$$f_m = 1 - \exp[-\alpha \cdot (M_s - T)^{\beta}] \quad (20)$$

In the L-VT equation, the effect of prior austenite grain size on M_s was considered using the M_s equation proposed by Capdevila et al. [206]. Values for α and β as a function of the alloying composition were obtained by fitting the model predictions with experimental data and the newly defined α and β were given as follows:

$$\alpha(\times 10^{-3}\mathrm{K}^{-1}) = 23.1 - 10.5x_{\mathrm{C}} + 7.4x_{\mathrm{Cr}} - 1.7x_{\mathrm{Ni}} - 19.3x_{\mathrm{Mo}} \quad (21)$$

$$\beta = 1.4304 - 1.1836x_{\mathrm{C}} + 0.7527x_{\mathrm{C}}^2 - 0.0739x_{\mathrm{Cr}} - 0.0258x_{\mathrm{Ni}} + 0.3108x_{\mathrm{Mo}} \quad (22)$$

It was found that the dependence of martensite fraction on quenching temperature, especially at a smaller undercooling below M_s, can be better predicted by the L-VT equation. In addition to alloying composition, it was also found that the parameter α in the L-VT equation is temperature [207] and austenite grain size [208] dependent.

The (modified) K-M equations discussed above are empirical. Huyan et al. [209] developed a thermodynamic model based on the Magee model [202] to predict the martensite fraction, by further taking the martensitic autocatalysis nucleation effect and austenite stabilization effect into account. The former one is attributed to the increased nucleation sites provided by the previous martensite while the latter one is attributed to the enhanced deformation energy in the untransformed austenite, i.e. the hydrostatic pressure caused by martensitic transformation [210]. If the increase in martensite fraction was assumed to be inversely proportional to the deformation energy in untransformed austenite, and the latter one was further assumed to be proportional to the chemical driving force $\Delta G^{\gamma\rightarrow\alpha'}$, the volume fraction of newly formed martensite in Eq. (13) becomes:

$$df_m = K(1-f_m)f_m \frac{1}{\Delta G^{\gamma\rightarrow\alpha'}} d(\Delta G^{\gamma\rightarrow\alpha'}) \quad (23)$$

where K is a material parameter. Integration of the chemical driving force from M_s to that at a certain temperature T yields:

$$f_m = \frac{1}{1+A^{-1}(\Delta G^{ex})^{-K}} \quad (24)$$

where A is constant and ΔG^{ex} is the difference between the chemical driving force at M_s and that at a certain temperature below M_s. After fitting the model predictions to experimental data, Eq. (24) was further modified as:

$$f_m = \frac{1}{1+20(\frac{\Delta G^{ex}}{100})^{-0.006M_S+0.1369}} \quad (25)$$

This thermodynamic model describes the martensite fraction as a function of the chemical driving force, instead of the degree of undercooling. Although this model has fewer fitting parameters, its predictions are quite comparable with those of the VB-S and L-VT models.

4.3.2. Phase transformations during partitioning

4.3.2.1. Immobile martensite/austenite interface

In order to retain the austenite present just after quenching and to make it survives from the further cooling to room temperature, the stability of austenite must be enhanced via carbon partitioning from the martensite into the austenite during the partitioning process. Speer et al. [10, 203] initially proposed a 'Constrained Para-Equilibrium' (CPE) model to predict the endpoint of carbon partitioning in the binary Fe-C system. The CPE model includes three critical assumptions:

(i) There is no migration of the martensite/austenite interface migration as a result of the short-range diffusion of iron atoms and lattice changes during partitioning;

(ii) Carbon partitioning from martensite into austenite will continue until the chemical potential of carbon in martensite and that in austenite are equal.

(iii) Other competitive reactions, e.g. carbides precipitation and austenite decomposition, are fully suspended;

For ternary and higher order alloys it is assumed that substitutional alloying elements M do not diffuse across the interface and thus the Fe/M ratio is identical for martensite and austenite. Hillert and Ågren [40] argued that the CPE term introduced by Speer et al. should not be confused with the para-equilibrium concept as [211]:

" *(a) Paraequilibrium is already a constrained equilibrium;*

(b) Paraequilibrium refers to conditions at a migrating interface;

(c) Due to a requirement of minimum free energy, CPE is applicable only to the final state, whereas paraequilibrium applies to growth of a new phase;

(d) Redistribution of (substitutional) alloying elements close to the interface is nearly unavoidable;

(e) Any redistribution of alloying elements at the martensite/austenite interface would have a substantial influence at the interface, but only a negligible effect on the overall carbon distribution throughout the bulk."

In a reply to Hillert and Ågren's argument, Speer et al. further clarified the definition of their CPE concept and changed their original classification 'Constrained Para-Equilibrium' to 'Constrained Carbon Equilibrium' (CCE) [211, 212]. A comparison between the CCE, PE and LE conditions will be discussed in next section.

Speer et al. [203] used the CCE model to predict the dependence of RA fraction on quenching/partitioning temperatures by coupling the martensite formation to the K-M equation. **Fig. 18a** shows the fraction of RA as a function of the quenching temperature as predicted by the CCE model for the binary Fe-C system. As carbon solubility in partitioned martensite is negligible and full partitioning of carbon from martensite into austenite is assumed, the carbon content in austenite after partitioning is expected to decrease with increasing quenching temperature. At lower quenching temperatures (<~280°C), carbon enrichment in austenite after partitioning is sufficient to retain all austenite to room temperature. However, when the

quenching temperature exceeds this critical value (~280°C), due to insufficient carbon enrichment, the austenite is partially transformed to fresh martensite during the final quenching step. As a result, there is an optimum quenching temperature of about 280°C to obtain a maximal amount of RA, as indicated in **Fig. 18a**.

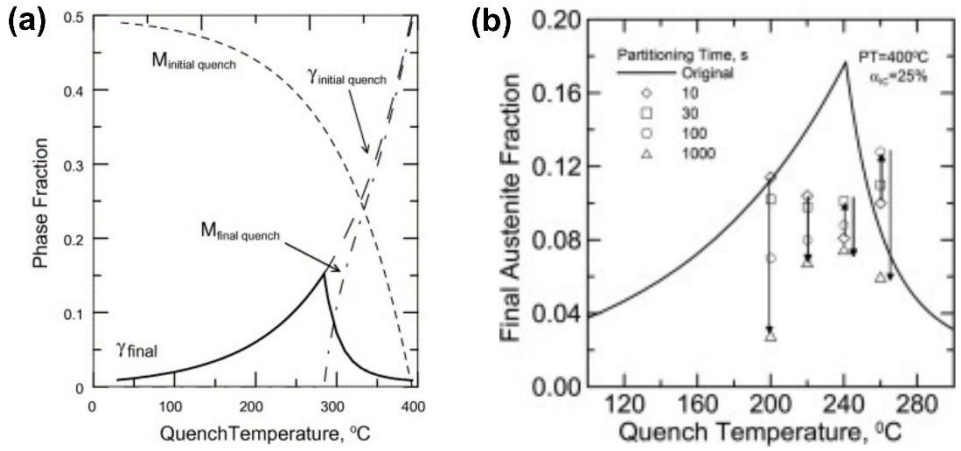

Fig. 18. (a) Phase fraction as a function of quenching temperature predicted by the CCE model for an intercritical annealed Fe-0.19C-1.46Mn-1.96Al steel containing 50% vol. ferrite [203]. (b) Experimental RA fraction as a function of quenching temperature and partitioning time for an intercritical annealed Fe-0.19C-1.59Mn-1.63Si steel containing 25% vol. ferrite and partitioned at 400°C [213].

It has been validated in several studies that the method proposed by Speer et al. can provide a practical and useful guide for the selection of optimum quenching temperature [144, 145, 203, 214, 215]. However, the method does not allow predicting the fraction of RA and its carbon content as a function of the partitioning time, since the kinetics of carbon partitioning was not considered in the CCE model. Assuming that carbon is in local equilibrium at the immobile interface, Hillert et al. [216] investigated the kinetics of carbon partitioning from carbon-supersaturated ferrite into austenite for a binary Fe-C system. Using the Hillert et al. concept, the kinetics of carbon partitioning from martensite into austenite in an Fe-0.19C-1.59Mn-1.63Si

alloy was simulated using DICTRA software by Clark et al. [11, 213]. **Fig. 18b** shows the experimentally measured fraction of RA as a function of partitioning time and quenching temperature, and the results are in good agreement with the model predictions by Clark et al. [213]. The RA fraction seems to be less sensitive to the quenching temperature when taking the kinetics of carbon partitioning into account.

Most simulations for the Q&P process were performed for (dimensionless) 1D conditions, which are helpful to present the implications of carbon partitioning. However, the microstructure evolution in Q&P steels is taking place in three dimensions and the degree of carbon partitioning is expected to be strongly dependent on austenite grain size and its surroundings. Mecozzi et al. [217] simulated the microstructure evolution during the Q&P process of a Fe-0.25C-3Mn-1.5Si steel using a 2/3D phase field model. They predicted that the carbon content in austenite is not just a function of the steel composition and the quenching conditions but is also strongly dependent on the size of austenite grain and its surrounding phases. In particular, it takes time for carbon to reach a homogenous state in large austenite grains, and thus it would lead to a carbon gradient in austenite if the partitioning time is too short. Austenite with a carbon gradient might partially transform into martensite during the final quenching as the core of the austenite grain having a lower carbon content could still transform to martensite.

4.3.2.2. Mobile martensite/austenite interface

One of the key assumptions in the CCE model was that the martensite/austenite interface is immobile during partitioning. Despite abundant efforts, there is a lively debate whether the martensite/austenite interface is mobile or not during partitioning. In many cases using indirect experimental data [144, 145, 215, 218, 219], the martensite/austenite interface was found to be

immobile, in agreement with the CCE model. However, Zhong et al. [220] were the first to observe an initially straight martensite/austenite interface to become curved after partitioning using ex-situ TEM measurements, which was regarded as semi-direct evidence that the martensite/austenite interface is mobile. Similar observations have also been made by other authors [221-224]. However, the direction of the martensite/austenite migration could not be deduced unambiguously from these studies. In some dilatometric studies [174, 207, 225], the volume of the sample was detected to expand during partitioning, which could be regarded as proof of an increase in the fraction of the BCC phase, e.g. continued austenite decomposition. Carbon partitioning should also cause volume expansion, but its effect on dilatation was considered to be negligible [174, 207, 226]. The BCC phase fraction was also found to increase during partitioning by in-situ HE-XRD measurements [146, 227, 228]. However, both in dilatometry and in HE-XRD it is impossible to distinguish austenite decomposition into bainite from that into martensite, so both experiments do not give hard evidence of a moving austenite-martensite interface.

Austenite formation during partitioning has also been observed in steels with a higher carbon or higher manganese content than that of the conventional (automotive) Q&P steels [218, 229, 230]. Bigg et al. [229] indirectly observed austenite formation during reheating from the quenching temperature to the partitioning temperature in an Fe-0.64C-4.57Mn-1.30Si steel using in-situ neutron diffraction. Direct observation of the martensite/austenite interface migration into martensite has been made in an Fe-1.0C-3Mn-1.5Si steel partitioned at 400°C using in-situ high resolution TEM by De Knijf et al. [230].

Zhong et al. [220] and Speer et al. [231] reanalysed the thermodynamic conditions at the martensite/austenite interface and deduced that the interface could migrate bi-directionally during partitioning. In order to explain the interface migration behaviour, Santofimia et al. [232] proposed a Q&P model based on the mixed-mode concept to quantitatively describe the kinetics

of martensite/austenite interface migration and carbon partitioning during partitioning in a binary Fe-C system. In the mixed-mode concept, the kinetics of interface migration is determined by both diffusion and interface mobility. As the mobility of the martensite/austenite interface at the partitioning temperatures is *a priori* unknown, three different activation energies for interface mobility corresponding to different interface crystallography structures were assumed in Santofimia et al.'s calculations: *(i)* an infinite value representing an immobile interface; *(ii)* a value of 180kJ/mol corresponding to a semi-coherent interface; *(iii)* a value of 140kJ/mol corresponding to an incoherent ferrite/austenite interface [233]. **Fig. 19a-c** show the predicted evolution of the carbon profiles and the interface migration during partitioning at 450°C for these three activation energies, and **Fig. 19d** shows the corresponding RA fraction as a function of the partitioning time. It was found that the CCE model prediction is quite comparable with that of the mixed-mode model when the activation energy is infinite (see **Fig. 19a**). When activation energy decreases to 180kJ/mol, the interface slowly migrates into austenite (see **Fig. 19c**). When the activation energy is 140kJ/mol, a bi-directional interface migration is predicted before equilibrium is reached (see **Fig. 19b**). The Q&P model proposed by Santofimia et al. was originally developed for binary Fe-C alloys, and it was later extended to multi-component system by assuming only carbon is in local equilibrium at the interface and the chemical driving force is proportional to the derivation from paraequilibrium state. Given such assumptions, the Santofimia et al. model has further been coupled with a 2D phase field model to simulate the microstructure evolution during partitioning in an Fe-0.19C-1.6Mn-0.35Si-1.1Al alloy with partial austenisation [234]. It was predicted that the carbon content in austenite is strongly affected by its surrounding phase distributions, and that any contacting ferrite grain is also an effective passage for carbon partitioning from martensite into its non-adjacent austenite.

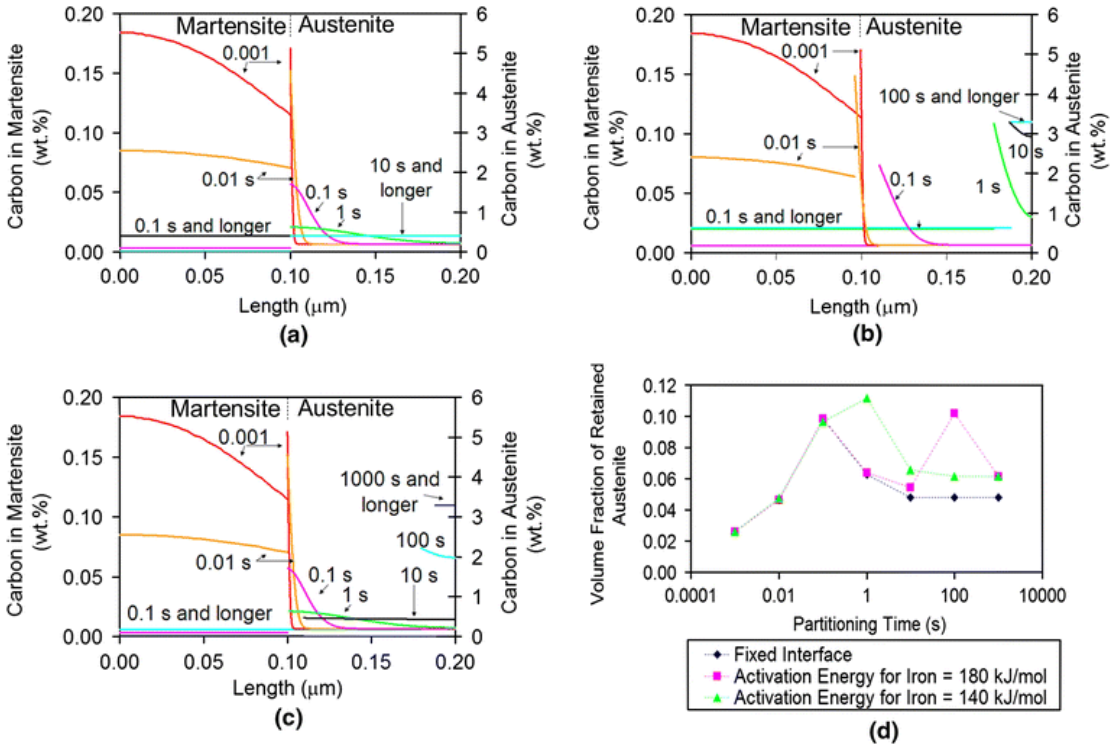

Fig. 19. Evolution of carbon profiles in martensite and austenite during partitioning at 450°C for a binary Fe-0.2C alloy. The activation energies for interface mobility are (a) infinite, (b) 140kJ/mol and (c) 180kJ/mol, respectively. (d) The RA fraction as a function of partitioning time for the three different activation energies [235].

As the mobility of the martensite/austenite interface was considered to play a significant role in the kinetics of carbon partitioning, much effort was made to determine the martensite/austenite interface mobility. Santofimia et al. [174] investigated the martensite/austenite interface migration behaviour during the Q&P process in an Fe-0.2C-2.5Mn-1.5Si-1.47Ni-1.01Cr steel. They found that the martensite/austenite interface migrated from martensite into austenite during partitioning, and the activation energy of interface mobility was estimated to be 215 kJ/mol by fitting experimental data with model simulations. De Knijf et al. [230] used in-situ high resolution TEM to measure the kinetics of interface migration from austenite into martensite during partitioning in an Fe-1.0C-3Mn-1.5Si high carbon steel, and they estimated the activation energy of the martensite/austenite interface

mobility to be about 165~170 kJ/mol, a value smaller than that measured by Santofimia et al. [174]. The mobility for the martensite/austenite interface was usually smaller than that of the ferrite/austenite interface, which could be attributed to the difference in the crystallographic structure of ferrite and martensite. As described above, the value of interface mobility is usually obtained by fitting (indirect) experimental data with model predictions, but it is very challenging to accurately measure the kinetics of interface migration during the Q&P process directly. As a result, there is still a very large uncertainty in the value of the martensite/austenite interface mobility.

In the Santofimia et al. model, the kinetics of carbon partitioning and interface migration during partitioning is strongly affected by the value of the martensite/austenite interface mobility, while carbon content in austenite at the endpoint of partitioning is determined by the paraequilibrium conditions. Based on the paraequilibrium assumption, martensite after partitioning should contain negligible carbon while carbon content in austenite could be as high as ~3 wt.% for most Q&P steels. However, the experimentally measured carbon content in RA is usually much lower than the paraequilibrium value [236]. In order to explain this discrepancy, Behera and Olson [147, 237] modified the Gibbs free energy of martensite with an additional effective stored energy, which is composed of elastic strain energy G_{el}, solid solution frictional work W_F^{SS} and friction work W_F^D dissipated due to interface migration across forest dislocations. **Fig. 20a** illustrates that the carbon content in austenite in its paraequilibrium state would decrease from Cγ to Cγ' when taking the effective stored energy concept into account. In the Behera-Olson model, the contribution due to the elastic strain energy was considered to be negligible and the solid solution friction work was calculated by $W_F^{SS} = A_\mu \mu(x_i, T)$ (see Eq. (9)). The friction work W_F^D dissipated due to interface migration across forest dislocations was then obtained via a comparison between the model predicted and experimentally measured Cγ' value. **Fig. 20b** shows that the friction work W_F^D is a linear function of the partitioning

temperature and quite comparable with that for bainite formation. **Fig. 20c** shows that the carbon content in RA predicted by the Behera-Olson model is in reasonable agreement with experiments.

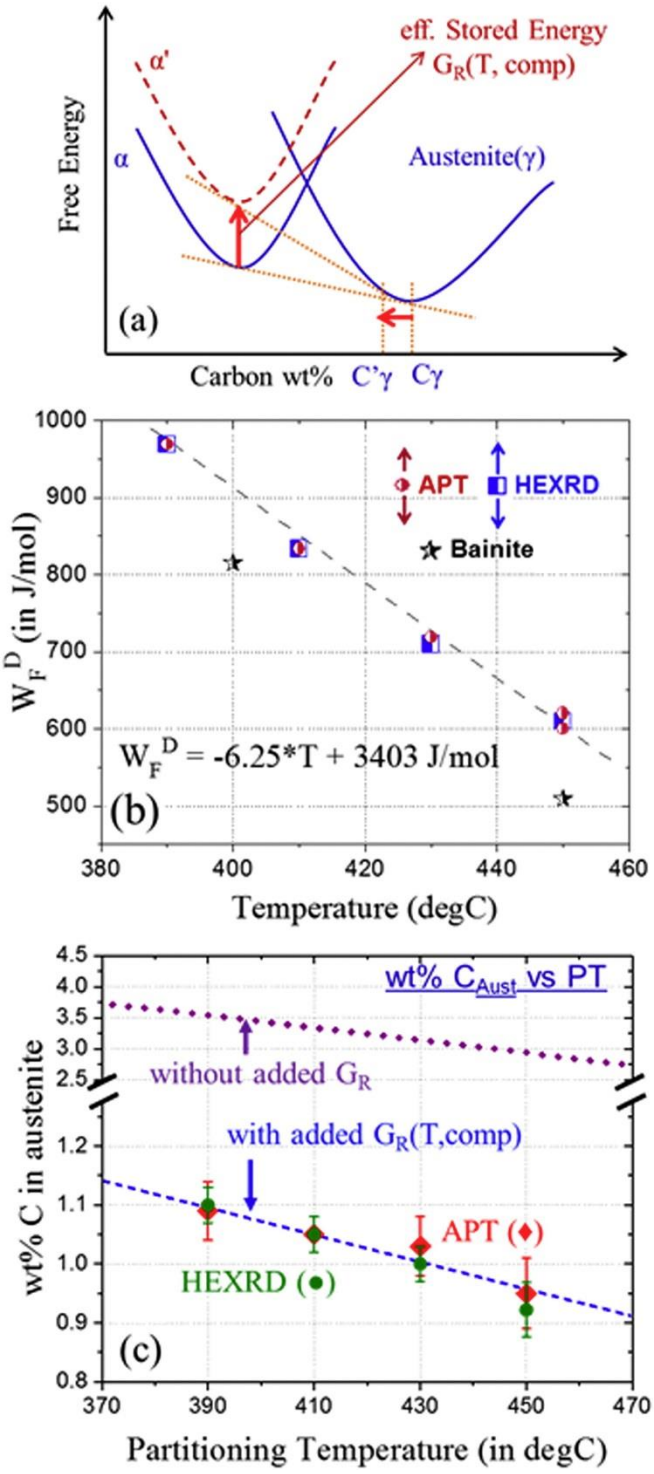

Fig. 20. (a) Schematic curves of the Gibbs free energy as a function of carbon content showing the effect of effective stored energy on the paraequilibrium carbon content in austenite. (b) The

friction work dissipated due to interface migration across forest dislocations W_F^D as a function of temperature. (c) Comparison between the predicted and measured carbon content in RA as a function of partitioning temperature [147].

The diffusivity of substitutional alloying element at a low partitioning temperature is extremely sluggish in comparison to that of the interstitial carbon. Hence, in most Q&P models it is assumed that the substitutional alloying elements do not partition between martensite and austenite. However, as shown in **Fig. 21a** and **b**, significant redistribution of substitutional alloying elements across the martensite/austenite interface during partitioning has been detected by several research groups using 3DAPT [141, 144, 145, 147, 164, 238-240]. Seo et al. [144, 145] argued that the substitutional alloying elements do not redistribute until carbon has fully partitioned fully from martensite into austenite under the CCE condition. In contrast to the CCE model assumptions, the diffusion of substitutional alloying atoms during partitioning indirectly indicates that the martensite/austenite interface can migrate. Besides, the interaction between substitutional alloying elements partitioning and martensite/austenite interface is expected to strongly affect the kinetics of carbon partitioning and interface migration [43].

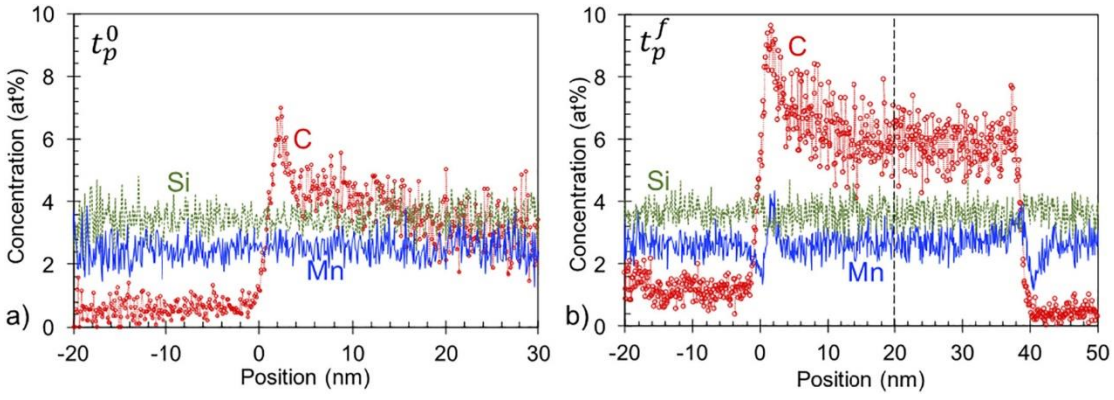

Fig. 21. Concentration profiles of C, Mn and Si in martensite and austenite for an Fe-0.3wt%C-2.5wt%Mn-1.5wt%Si alloy during partitioning at 400°C. (a) t_p^0, at the beginning of the partitioning process. (b) t_p^f, after partitioning for 200s [240].

In order to elucidate the role of substitutional alloying element partitioning in the kinetics of interface migration and carbon partitioning, Dai et al. [241, 242] developed a so-called quenching and partitioning-local equilibrium (QP-LE) model based on the local equilibrium assumption. In the QP-LE model, all elements are assumed to be in equilibrium at the moving martensite/austenite interface. Besides, carbides precipitation and austenite decomposition into bainite are fully suspended. **Fig. 22a** shows the kinetics of interface migration and carbon partitioning as predicted by the QP-LE model for an Fe-0.25C-2.1Mn-1.1Si steel during partitioning at 400°C after quenching to 230°C. It shows that the martensite/austenite interface migrates into martensite under the NPLE-($\alpha'\rightarrow\gamma$) mode firstly and then under the PLE-($\alpha'\rightarrow\gamma$) mode. Both the duration of the NPLE-($\alpha'\rightarrow\gamma$) stage and the distance of interface migration are very short, which could hardly be experimentally observed. For this case, the "*immobile interface*" assumption in the CCE model seems to be acceptable. Although the martensite/austenite interface migration predicted by the QP-LE model is phenomenologically comparable with the CCE predictions, these models have totally different physical origins. According to the QP-LE model, the "*immobile interface*" is physically attributed to the significant partitioning of substitutional alloying elements across the martensite/austenite interface. It is predicted by the QP-LE model that carbon content in austenite after partitioning is located between the NPLE/PLE transition for $\gamma\rightarrow\alpha$ transformation and NPLE/PLE transition for $\alpha\rightarrow\gamma$ transformation, which is strongly dependent on the quenching temperature. The fraction of RA and its carbon content predicted by the QP-LE model for Q&P steels quenched to lower temperatures are quite comparable with the CCE model (see **Fig. 23a**, **d**, **e** and **f**) [44].

Fig. 22b shows the kinetics of interface migration and carbon partitioning predicted by the QP-LE model for an Fe-0.25C-2.1Mn-1.1Si steel during partitioning at 400°C after quenching to 290°C. The QP-LE model predicts that at a higher quenching temperature the

martensite/austenite interface first migrates into the martensite and then in the opposite direction, which is different from the CCE model assumption. At the endpoint of carbon partitioning, the carbon content in austenite predicted by the QP-LE model is determined by the NPLE/PLE transition for $\gamma \rightarrow \alpha$ transformation, which depends on the partitioning temperature (see **Fig. 23c**) and the Mn content (see **Fig. 23b** and **e**) but is independent of the quenching temperature [44]. In general, the QP-LE model predicts that the martensite/austenite interface could migrate either into the martensite or into the austenite, depending on the quenching temperature, the partitioning temperature and the alloy composition.

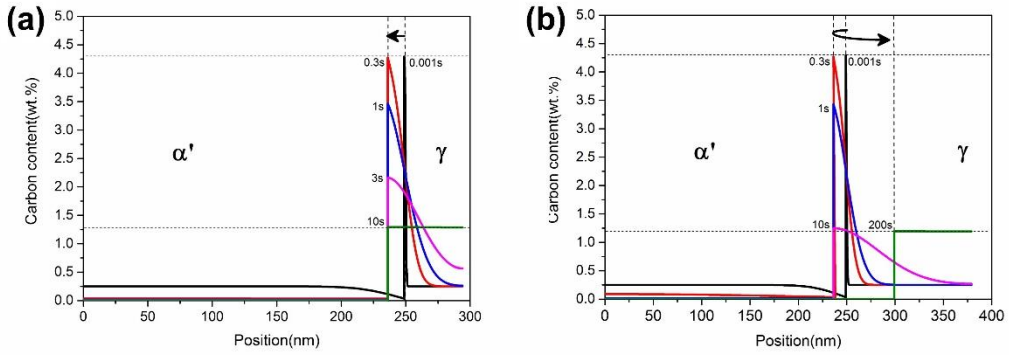

Fig. 22. Kinetics of interface migration and carbon partitioning predicted by the QP-LE model for an Fe-0.25C-2.1Mn-1.1Si steel partitioning at 400°C after quenching to (a) 230°C or (b) 290°C [242]. Arrows indicate the direction of interface migration. α': martensite; γ: austenite.

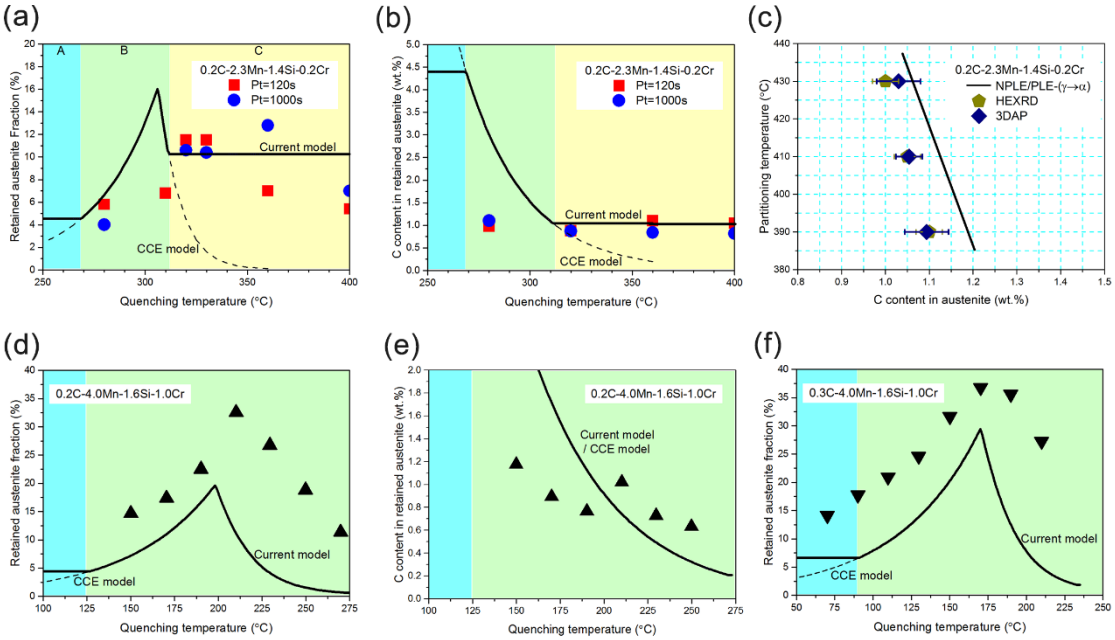

Fig. 23. (a, d, f) Comparison between the measured and predicted RA fraction as a function of the quenching temperature. Comparison between the measured and predicted carbon content in RA as a function of (b, e) the quenching temperature and (c) the partitioning temperature [44].

Given that the paraequilibrium state is commonly used to predict the endpoint of carbon partitioning during partitioning [147, 232, 233, 237], Dai et al. [241, 242] also proposed a so-called quenching and partitioning-paraequilibrium (QP-PE) model based on paraequilibrium assumption, in which only carbon is in local equilibrium while the substitutional alloying element is constrained. The QP-PE model predicts that for Q&P steels quenched to lower quenching temperatures the martensite/austenite interface can only migrate a very short distance during a very short period of time, while for Q&P steels quenched to higher quenching temperatures it first migrates into martensite and then in the opposite direction. In contrast to the QP-LE model predictions, the fraction of RA and its carbon content after partitioning predicted by the QP-PE model are independent on the quenching temperature and almost insensitive to the partitioning temperature and the alloying composition. Such predictions are obviously contrary to experiments [242]. Also, the significant redistribution of substitutional

alloying elements across the interface as detected using 3DAPT [141, 144, 145, 147, 164, 238-240] cannot be explained by the QP-PE model. Later Dai et al. [44] applied the QP-LE model to design the RA in Q&P steels. As shown in **Fig. 24a** and **b**, interestingly it was found that the processing window to obtain a maximal amount of RA in Q&P steels could shrink significantly with increasing Mn content. It means that increasing Mn content is not an effective route to enhance the RA fraction in Q&P steels despite the fact that Mn is a strong austenite stabilizer.

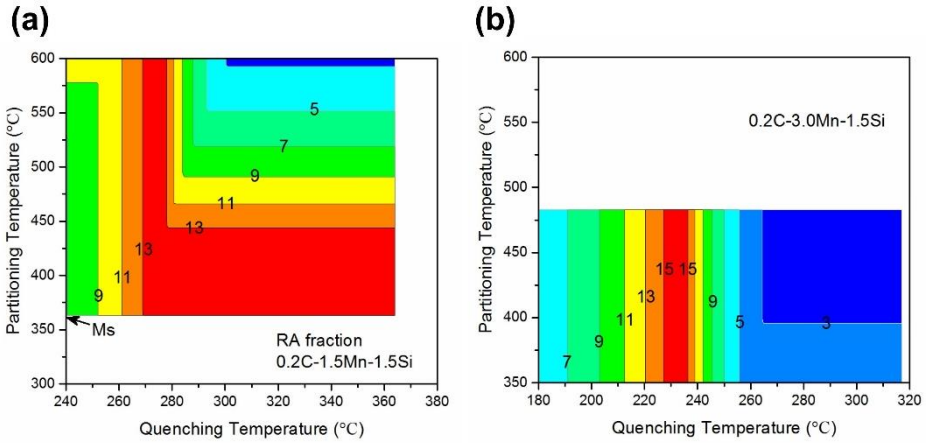

Fig. 24. Contour plots of the RA fraction as a function of the quenching temperature and the partitioning temperature. (a) Fe-0.2C-1.5Mn-1.5Si steel; (b) Fe-0.2C-3.0Mn-1.5Si steel [44].

4.3.2.3. Bainite formation

Besides the migration of martensite/austenite interface, bainite formation was also found to occur during the partitioning process [146, 243, 244]. The purpose of the Q&P process is to stabilize austenite down to ambient temperatures via carbon partitioning from the martensite into the austenite. However, it is unavoidable that austenite containing an insufficient percentage of carbon content would decompose into bainite during partitioning. Bainite formation during partitioning is expected to affect the final microstructures and mechanical properties significantly [245-251]. Hence, it is of great importance to clarify the mechanism of bainite formation during partitioning. We have discussed the mechanism of bainite formation

in the fully austenitic microstructure in CFB steels (see Chapter 3) or constrained by ferrite phase in TRIP steels (see Chapter 2). Compared with them, the mechanism of bainite formation in Q&P steels is more complex, as it is strongly affected by the presence of pre-existing martensite:

(i) Acceleration effects due to the presence of martensite/austenite interfaces, which could act as preferential nucleation sites for bainitic ferrite;

(ii) Acceleration effects due to the presence of a high density of dislocations induced by the martensite formation. Dislocations are regarded as preferential nucleation sites for bainite formation;

(iii) Deceleration effects due to the presence of the enhanced carbon concentrations around pre-existing martensite grains as a result of the ongoing carbon partitioning.

Kawata et al. [63] claimed that the kinetics of bainite formation is accelerated by the presence of martensite/austenite interfaces (i.e. in support of factor *(i)*). They compared the kinetics of bainite formation starting from a mixed microstructure consisting of 26 vol.% ferrite and 74 vol.% austenite in an Fe-0.3C-2.5Mn steel with that from a mixed microstructure consisting of 22 vol.% martensite and 78 vol.% austenite in an Fe-0.4C-2.5Mn steel. Due to Si being absent, excess carbon in the martensite was considered to be consumed by carbides precipitation. Hence, based on lever rule, the carbon content in untransformed austenite in the Fe-0.3C-2.5Mn steel after ferrite formation should be approximately equal to that in the Fe-0.4C-2.5Mn steel after quenching. Although the strain in the austenite introduced by the martensite formation is much larger than that by the ferrite formation, it was found that the pre-existing martensite on the kinetics of bainite formation is similar to that of pre-existing ferrite. Hence, it was suggested by Kawata et al. [63] that the acceleration effect of pre-existing martensite on bainite formation should be mainly attributed to the presence of martensite/austenite interfaces (i.e. factor *(i)*), instead of dislocation introduced by the prior

martensite formation (i.e. factor *(ii)*). It is worth pointing out that in Q&P processing the density of martensite/austenite interfaces is expected to be much higher than that of the ferrite-austenite microstructure present during TRIP processing, which means that the kinetics of bainite formation from a martensite-austenite microstructure should be faster than for a typical ferrite-austenite microstructure. Furthermore, Zhu et al. [65] found the kinetics of bainite formation was even retarded by pre-existing ferrite and attributed this to alloying elements enrichment near the interface reducing the driving force for bainite formation.

In order to clarify the effect of pre-existing martensite on bainite formation, Gong et al. [96] investigated the kinetics of bainite formation in an Fe-0.79C-1.98Mn-1.51Si-0.98Cr-0.24Mo-1.06Al-1.58Co nano-bainite steel with and without pre-existing martensite using in-situ neutron diffraction. To exclude the influence of carbon partitioning from pre-existing martensite into austenite on bainite formation, a very small amount of pre-existing martensite was obtained via a quenching step. Bainitic ferrite was found to form adjacent to the pre-existing martensite and both of them have an almost identical orientation relationship. In-situ neutron diffraction results showed that the dislocation density in austenite after martensite formation is very high and of the same order of magnitude as that in martensite, which is in agreement with the investigations by Shibata et al. [252] and Miyamoto et al. [253]. Therefore, Gong et al. [96] argued that dislocations in austenite introduced by prior martensite formation serve as nucleation sites for bainitic ferrite and promote the kinetics of bainite formation (i.e. factor *(ii)*).

Toji et al. [243] further investigated the competition between the acceleration effects due to the presence of martensite/austenite interface or dislocation (i.e. factor *(i)* or *(ii)*) and the deceleration effects of carbon partitioning from pre-existing martensite into austenite (i.e. factor *(iii)*) in two high carbon steels with and without Si addition, i.e. Fe-1.1C-3.0Mn-(0, 2.0)Si. Dilatometry results showed that the kinetics of bainite formation in the Si-added steels with or

without pre-existing martensite is lower than that in the Si-free steels due to significant carbon partitioning into austenite in the Si-added steels. However, the kinetics of bainite formation is accelerated by pre-existing martensite regardless of Si addition, which could be attributed to the presence of dislocations and/or the pre-existing martensite/austenite interfaces. The effect of pre-existing martensite on the kinetics of bainite formation in the Si-free and Si-added steels was further illustrated in **Fig. 25a** and **b**, respectively. As shown in **Fig. 25a**, in the Si-free steels, the kinetics of bainite formation for the sample containing 30% pre-existing martensite is similar to that already containing 30% bainite. However, **Fig. 25b** shows that the kinetics of bainite formation in the Si-containing sample with 30% pre-existing martensite is faster than that containing 30% bainite. The significant acceleration effect of pre-existing martensite on the bainite formation kinetics in the Si-added steels could be because carbides are easier to precipitate in the pre-existing martensite than in the pre-existing bainite. Carbides precipitation near the martensite/austenite interface in the Si-added steels was indeed detected using 3DAPT, which is expected to decrease carbon enrichment in austenite near the interface to some extent and to promote bainite formation. However, the carbon content near the martensite/austenite interfaces could be still high enough to inhibit the nucleation of bainitic ferrite. Thus, Toji et al. [243] suggested that bainitic ferrite plates initially nucleate at the dislocation introduced by martensite formation in austenite slightly away from the martensite/austenite interface. Subsequently, some of nucleated bainitic ferrite plates grow to impinge the martensite/austenite interface while others grow into the interior of austenite. Hence, Toji et al. [243] suggested the high density of dislocations introduced by pre-existing martensite (i.e. factor *(ii)*) plays a significant role in the bainite formation, which supports the view of Gong et al. [96].

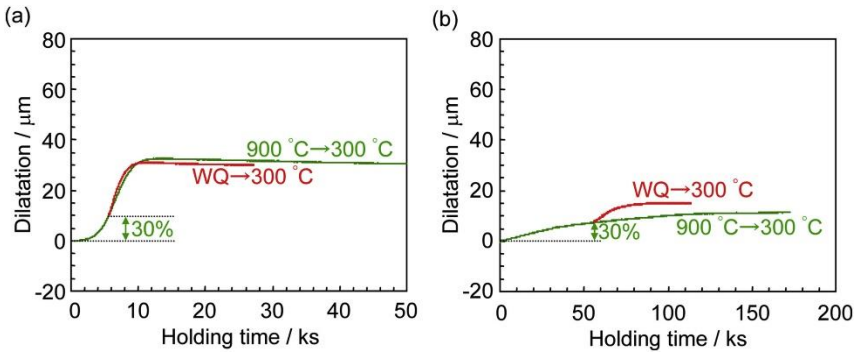

Fig. 25. Comparison of the kinetics of bainite formation with (red line) and without (green line) the presence of pre-existing martensite in (a) Fe-1.1C-3.0Mn and (b) Fe-1.1C-3.0Mn-2.0Si steels. WQ: water quenching [243].

In addition to experimental investigations, bainite formation during the Q&P process was also analysed based on diffusionless [151, 251, 254, 255] or diffusional theories [256]. HajyAkbary et al. [151] studied the influence of carbon partitioning from martensite into austenite on bainite formation in an Fe-0.3C-3.5Mn-1.6Si steel. They regarded the expansion of samples during partitioning as indicative of bainite formation. Assuming the martensite/austenite interface to be immobile, it was predicted that carbon atoms in martensite could escape into austenite within several seconds, while it takes much longer time to reach the homogeneous state due to low diffusivities of carbon in austenite. Due to the heterogeneous carbon distribution in the many different austenite grains present, austenite grains with sufficient carbon are retained to room temperature while those containing lower carbon content are transformed into bainite during the partitioning process. It is known that bainitic ferrite prefers to nucleate either at a martensite/austenite interface, a bainitic ferrite/austenite interface, or a prior austenite grain boundary. As the proportion of prior austenite gain boundary area is negligible, only the martensite/austenite and bainitic ferrite/austenite interfaces were considered as effective nucleation sites. Based on the kinetic model for bainite formation

proposed by Van Bohemen et al. [257, 258], the increased bainite fraction during partitioning was calculated by:

$$\frac{df_B}{dt} = (1 - f_B - f_{M1} - f_{RA})(1 + \lambda_{M1} f_{M1} + \lambda_B f_B) k_f \quad (26)$$

where f_{M1} is the fraction of primary martensite formed during the first quenching step, f_{RA} is the fraction of austenite stabilized by carbon partitioning from martensite into austenite, f_B is the fraction of bainite, k_f is a rate parameter dependent on temperature and composition, λ_{M1} and λ_B are the autocatalysis coefficients for martensite/austenite interface and bainitic ferrite/austenite interface, respectively. They found that kinetics of bainite formation can be fitted well by the diffusionless model when the autocatalysis coefficients for bainite nucleation at martensite/austenite interface and bainitic ferrite/austenite interface are assumed to be 13 and 6, respectively. The autocatalysis coefficients indicate that the acceleration effect due to the presence of a pre-existing martensite/austenite interface is stronger than that due to a bainitic ferrite/austenite interface.

In the study of HajyAkbary et al. [151], it was assumed that bainite formation takes place once carbon partitioning from martensite into austenite has taken place. However, bainite formation and carbon partitioning from martensite are expected to occur simultaneously, and these two kinetic processes are highly correlated. Nishikawa et al. [256] attempted to simulate the interaction between carbon partitioning and bainite formation in the binary Fe-C system using an 1D model. In their simulations, the martensite/austenite interface was assumed to be immobile in line with the CCE theory, and a mixed-mode model was used to simulate thickening kinetics of bainitic ferrite while lengthening kinetics was not considered. It was assumed that thermodynamic limit of bainite formation is determined by the WBs theory [114], and that the driving force for bainitic ferrite formation is proportional to the deviation from the WBs limit. It was predicted that the kinetics of carbon partitioning plays an important role in bainite formation during the Q&P process. The kinetics of bainite formation in an Fe-0.25C

alloy can be decelerated by soft impingement of carbon diffusion in austenite. Interestingly it was also predicted that austenite formation instead of bainite formation could occur during partitioning in an Fe-0.8C high carbon steel, which is because that the carbon enrichment in the austenite partitioned from the martensite exceeds the WBs limit and thus results in a negative driving force for bainite formation, but in a positive driving force for austenite formation. In general, Nishikawa et al.'s simulations indicated that the kinetics of bainite formation is decelerated by carbon partitioning from martensite in both low and high carbon steels.

Until now, most of the attention has been focused on the effect of pre-existing martensite on bainite formation. The competition between martensite/austenite interface migration and bainite formation during the Q&P process has not been properly investigated yet, as it is quite difficult to experimentally distinguish the bainitic ferrite from the tempered martensite in a convincing way, since both of them have a similar crystal structure and morphology. Some researchers believed that the increase of BCC phase during the partitioning process was due to bainite formation [146, 151, 227, 228, 259], while the possibility of martensite/austenite interface migration was supported in [218, 220-222, 230].

4.3.2.4. Carbide precipitation

In some specific cases, micro-alloyed carbides MC (M=Nb, V, Mo, etc.) were intentionally introduced in order to improve the strength of Q&P steels, as proposed by Hsu and his co-workers [148, 149]. However, in conventional Q&P steels, η (or ε) transition carbide and cementite precipitation will reduce the amount of carbon available for carbon partitioning, without making a significant contribution to the flow stress. The competition between carbide precipitation (-dissolution) and carbon partitioning into austenite plays an important role in controlling the RA fraction and its carbon content. Despite much effort to optimize the alloying

composition and processing parameters, η (or ε) transition carbide and even cementite formation cannot be completely avoided in conventional Q&P steels [260-265]. The plate-like η (or ε) transition carbide has a typical thickness of 10~30 nm and a diameter of 100~400 nm. Some researchers [140, 151, 221, 260, 266-268] using TEM observed that ε transition carbide precipitates formed in Q&P steels while others [143, 269-271] regarded the precipitates found as η transition carbides. Given that the crystal structure of hexagonal ε transition carbide is quite similar to that of orthorhombic η transition carbide, it is usually difficult to distinguish them from each other. In some cases, cementite could also be observed in Q&P steels [145, 164, 239, 270, 272], especially for high carbon steels [238], after partitioning at higher temperatures [145, 270] or at longer partitioning times [270].

Carbides prefer to nucleate at defects in martensite, i.e. at dislocations, twins and interface boundaries. A high carbon content not only increases the driving force, but also increases the density of nucleation sites for transition carbides [273]. First-principle calculations indicated that both Mn and Si additions could stabilize ε transition carbides in martensite. However, the role of them in the ε transition carbide precipitation is different. Substitution of Fe by Mn decreases the formation energies of ε transition carbide. Although Si addition is not thermodynamically favourable for ε transition carbide formation, Si would decrease the misfit of the carbides/martensite interface and thus indirectly promote the kinetics of ε transition carbide precipitation [274, 275]. As discussed above, ε transition carbide precipitation is inevitable and even accelerated by typical alloying elements in conventional Q&P steels.

Compared with transition carbides, cementite precipitation in Q&P steels can be effectively retarded by Si addition. Miyamoto et al. [276] found that cementite nucleates in tempered martensite under the PLE mode in ternary Fe-C-Si alloy, as the chemical driving force for cementite nucleation under the PE mode is much smaller than that under the PLE mode. When the misfit strain energy between cementite and martensite was also considered, Kim et

al. [277] found that the driving force for cementite nucleation under the PE mode would be further reduced. Hence, it is generally recognized that the nucleation and growth of cementite in martensite is accompanied with Si redistribution, which would significantly reduce the kinetics of cementite precipitation. However, some researchers [278-281] found that cementite could precipitate under the PE mode during tempering in the quaternary Fe-C-Mn-Si systems using atom probe field-ion microscopy (APFIM), although Si addition reduces the chemical driving force for para-cementite precipitation. The discrepancy between cementite precipitation behaviour in the Fe-C-Si and Fe-C-Mn-Si systems during tempering was explained by Miyamoto et al. [276] that the driving force for para-cementite precipitation is enhanced by Mn addition. As discussed above, the mechanism of Si inhibiting cementite precipitation in martensite without considering carbon escaping from martensite into austenite has been investigated widely. However, significant carbon escaping from martensite during the Q&P process could reduce the driving force for cementite precipitation. Therefore, it is expected that partitioning of Si between cementite and martensite is required for the further growth of cementite during partitioning, even if the cementite precipitates under the PE mode at the early stage of Q&P process [145, 272].

In general, Si addition was found to be very effective in retarding cementite precipitation, but less effective in inhibiting transition carbide precipitation. In order to avoid carbide precipitation, substitution of Si by Al in Q&P steels was also proposed [167, 262, 282]. However, both first-principle calculations [274] and experimental studies [262, 283] indicate that Al addition could be relatively less effective in suppressing transition carbide and cementite precipitation than Si does at relatively low temperatures. The effects of Si and Al addition on the carbide precipitation and RA decomposition during continuous heating was systematically compared by Zhu et al. [283]. As shown in **Fig. 26**, decomposition of RA into carbides and ferrite was almost not affected by Al addition while it was significantly retarded by Si addition.

The temperature range for ε transition carbide precipitation is greatly enlarged by the addition of either Si or Al. In Al-added steels, there is a rather wide temperature range from 350°C to 430°C, in which both ε transition carbide and cementite could form. In the Si-added steels ε transition carbide and cementite could hardly form at the same time. Given that the typical partitioning temperature for Q&P steels is 400°C, Al could be less effective in suppressing cementite precipitation than Si does. However, Zhu et al. [283] found that Al could be more effectively in retarding the growth and coarsening of cementite at higher temperatures or longer time.

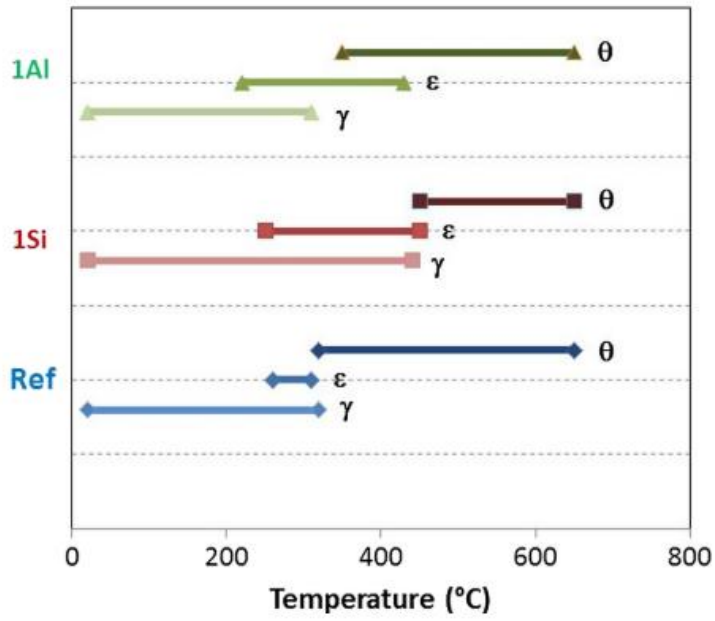

Fig. 26. The evolution of carbides and RA during continuous heating at a rate of 0.5°C/s for three steels: Fe-0.25C-2.1Mn (denoted as Ref), Fe-0.25C-2.1Mn-1.1Si (denoted as 1Si) and Fe-0.25C-2.1Mn-1.1Al (denoted as 1Al) [283]. γ: austenite; ε: transition carbide; θ: cementite.

In addition to alloying composition, the processing conditions also play an important role in the complex evolution of carbide precipitation in Q&P steels. However, due to the low fraction and nanometer size of transition carbide, it is usually challenging to directly observe their formation during the Q&P process using existing physical characterisation techniques.

Based on their TEM measurements HajyAkbary et al. [151] and Edmonds et al. [260] deduced that transition carbides could form during quenching via auto-tempering and then dissolve in the initial stage of the partitioning process. A similar phenomenon was observed by Pierce et al. [270] using Mössbauer effect spectroscopy (MES). In contrast, using HE-XRD, Allain et al. [271] found that transition carbide forms during reheating from quenching temperature to partitioning temperature and its amount almost stays constant during the partitioning process in an Fe-0.3C-2.5Mn-1.5Si steel. Systematic studies were performed by Pierce et al. [143, 269, 270] to investigate the evolution of carbide precipitation and its effects on RA in Fe-0.38C-1.5Mn-1.5Si and Fe-0.2C-1.5Mn-1.5Si-1.5Cr (or 1.5Ni) steels using MES. The influence of the quenching process on the amount of transition carbide can be interpreted from two perspectives. One perspective is that a considerable amount of transition carbide could precipitate in martensite via auto-tempering [151, 269, 270], which is expected to be strongly dependent on quenching temperature and holding time. Another perspective is that the fraction of pre-existed austenite before the partitioning process can be tuned by adjusting the quenching temperature. As a reservoir of carbon atoms but also containing carbon trapping sites, the pre-existing austenite can attract carbon from the neighbouring martensite. Hence, the amount of carbide measured by Pierce et al. [269] decreases with increasing the pre-existing austenite fraction, i.e. the quenching temperature. Additionally, the competition between carbides precipitation (-dissolution) and carbon partitioning into austenite is strongly affected by the partitioning temperature. **Fig. 27** shows the evolution of (a, d) the carbide fraction, (b, e) the RA fraction, the carbon content in RA and (c, f) the fraction of the total bulk carbon in each phase during partitioning at 400°C or 450°C for an Fe-0.38C-1.5Mn-1.5Si steel [270]. It shows that the kinetics of carbon partitioning from martensite into austenite could be effectively enhanced at the early stages of partitioning by raising the partitioning temperature, which leads to a lower transition carbide fraction and a higher RA fraction. However, during a longer partitioning time

at a higher partitioning temperature, the amount of carbides increases significantly due to the austenite decomposition into a mixture of ferrite and cementite. A recent work by Pierce et al. [143] shows that, when the thermal stability of austenite is enhanced via Cr addition, the amount of RA and its carbon content can be effectively improved by increasing the partitioning temperature or the partitioning time.

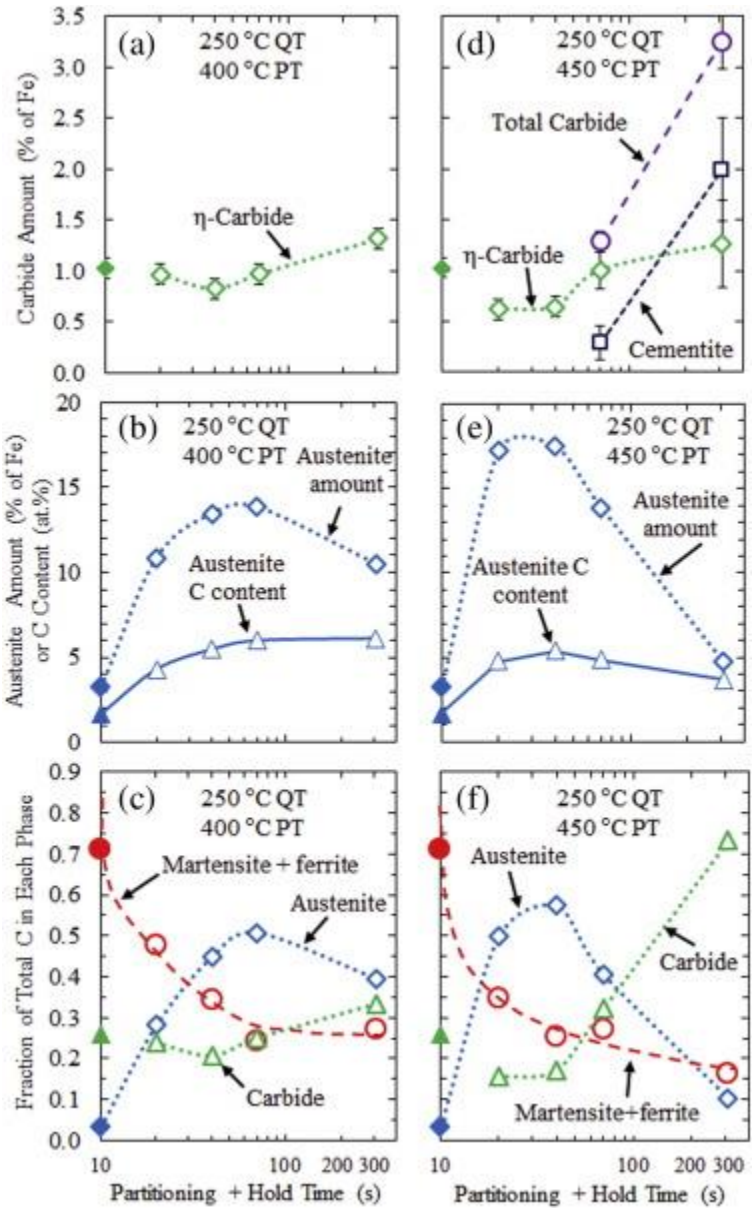

Fig. 27. The evolution of (a, d) carbide amount, (b, e) RA amount and carbon content in RA and (c, f) fraction of total carbon in each phase during partitioning at (a,b,c) 400°C or (d,e,f) 450°C after quenching to 250°C and holing at quenching temperature for 10s [270].

As discussed above, the formation of carbide is expected to change the behaviour of carbon partitioning during the Q&P process. As carbide precipitation reduces the carbon enrichment in austenite and thus enhances the driving force for the austenite decomposition, e.g. the martensite/austenite interface migration into austenite and/or the bainite formation, it would definitely affect the final microstructure of Q&P steels [243]. Toji et al. [272] investigated the cementite precipitation behaviour and its effects on carbon enrichment in austenite in an Fe-0.6C-2.9Mn-2.0Si steel. Using 3DAPT, they observed that the Mn and Si contents in cementite gradually decrease with increasing the partitioning time, indicating that the cementite precipitates under the PE mode at the early stage of the partitioning process, which is in agreement with other experiments [278-280]. However, as the driving force for para-cementite precipitation is reduced significantly by both Si in cementite and carbon escaping from martensite, significant Si partitioning between cementite and martensite is necessary for the further growth of cementite. Toji et al. [272] also proposed a modified CCE model, i.e. CCEθ model, to describe the effect of cementite precipitation on the carbon enrichment in austenite during the Q&P process. In the CCEθ model it is assumed that at the endpoint of carbon partitioning carbon has an equal chemical potential in cementite, martensite and austenite. Based on the growth behavior of cementite, two conditions were taken into account in the CCEθ model. One is termed as CCEθ-I, in which the cementite is assumed to precipitate under the PE mode. The other one is termed as CCEθ-II, in which the growth of cementite is accompanied with the redistribution of substitutional alloying elements. Compared with CCEθ-I, the carbon content in RA predicted by the CCEθ-II was found to be in reasonable agreement with experiments. It was also predicted by the CCEθ model that for high carbon Q&P steels the carbon content in RA after partitioning is insensitive to the bulk carbon content and the quenching temperature, which is in good agreement with their experiments. The CCEθ model

was proposed to describe the endpoint of carbon partitioning while the kinetics of cementite precipitation, carbon partitioning and austenite decomposition was not considered. Recently, Nishikawa et al. [284] discussed the effects of carbide precipitation on the kinetics of bainite formation in a Q&P processed ductile cast iron by coupling the CCEθ and WBs theories. They assumed that carbides are already precipitate and an equilibrium between martensite and carbide is reached before partitioning. It was found that stable carbides precipitation during quenching would prevent carbon partitioning from martensite, while less stable carbides would dissolve gradually and retard bainite formation during partitioning.

In summary, carbide precipitation is a common yet hard to capture phenomenon in Q&P steels, and it can strongly affect the kinetic processes of carbon partitioning, martensite/austenite interface migration and bainite formation. It thus enhances the complexity of microstructure evolution in Q&P steels. The mechanism of carbide precipitation, in particular transition carbides, is not well understood due to intrinsic limitations in the available characterisation techniques, and further research is required.

5. Medium Mn steels

5.1. Desired microstructures and required chemical composition

As stated earlier the strength-elongation product in AHSSs has been found to be generally proportional to the fraction and stability of RA [13, 285]. However, the volume fraction of RA in TRIP steels, CFB steels and Q&P steels is usually less than 0.2 due to their lean composition. C and Mn are both well-known austenite stabilizers in AHSSs, and thus increasing Mn and C content in steels is expected to be an effective route to enhance the fraction of RA. However, there is a strict limit on carbon content in automotive steels as good (spot-) weldability is of similar importance as excellent mechanical properties. Thus, increasing the Mn content is another practical option to increase the RA fraction and this has led to the well-known medium Mn steels. The typical microstructures of hot-rolled and cold-rolled medium Mn steels are shown in **Fig. 28a** and **b**, respectively. Medium Mn steels usually have an ultrafine dual phase microstructure, containing 20~50 vol. % C- and Mn- enriched RA and a ferrite matrix (i.e. a heavily tempered martensite). Compared with Q&P steels also having a tempered martensite matrix, the ultrafine-grained ferrite in medium Mn steels is softer. Therefore, the strength of medium Mn steels is usually somewhat lower than that of Q&P steels, but they have a much better elongation due to a higher RA fraction. To achieve more excellent balance between strength and elongation, some efforts [286-289] have also been made to obtain a mixed microstructure containing of martensite and retained austenite in medium Mn steels.

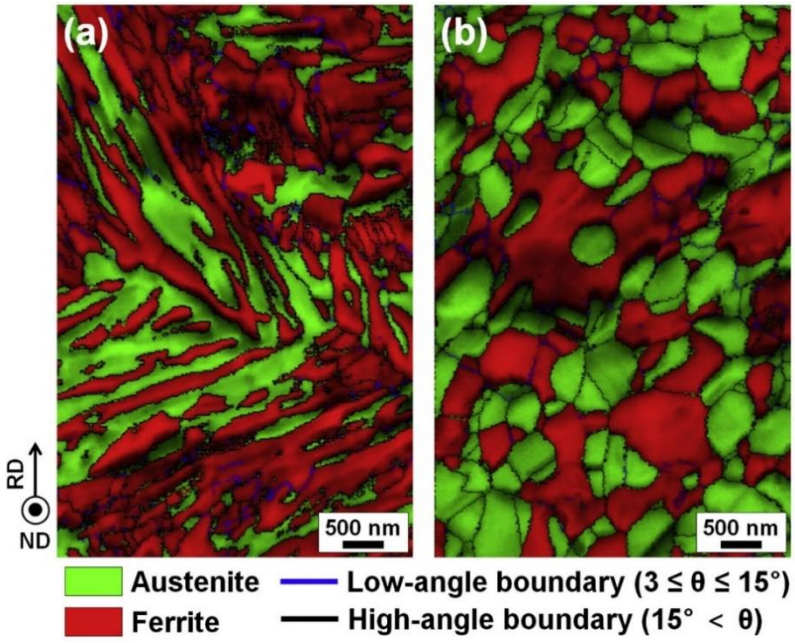

Fig. 28. EBSD images of (a) hot-rolled and (b) cold-rolled medium Mn steels [290].

Medium Mn steels usually contain 0.05~0.4 wt.% C and 3~10 wt.% Mn. For some medium Mn steels, Si or Al is also added to suppress the formation of cementite and thus to promote the partitioning of C into austenite. **Fig. 29a** and **b** show the effects of C and Mn additions on the phase diagram of Fe-C-Mn alloy, respectively. C addition narrows the intercritical annealing temperature region and promotes carbides precipitation at low temperatures. Mn addition shifts the intercritical annealing region to a lower temperature region. **Fig. 29c** and **d** show the effects of Si and Al additions on the phase diagram of Fe-0.2C-5Mn alloy, respectively. Besides suppressing carbide formation, Si and Al both increase the Ae_1 and Ae_3 temperatures [291]. Si addition enhances the tensile strength via solid solution strengthening, while it deteriorates the surface quality due to the formation of Si enriched oxide, which negatively influences the Zn coating process. A high content of Al causes the formation of coarse δ-ferrite during solidification [291-293]. The effects of C, Mn, Si and Al content on the microstructure and properties of medium Mn steels have been reviewed in more detail in [294-296]. In order to enhance the strength of medium Mn steels, nano-sized carbide or coherent B2 ordered NiAl

nanoparticles can be introduced via micro-alloying elements addition, such as Mo, Ti, Nb and V [286, 295, 297-302], or Ni and Al addition [303-307], respectively. In addition, the addition of micro-alloying elements is also beneficial to the refinement of prior austenite grain [308].

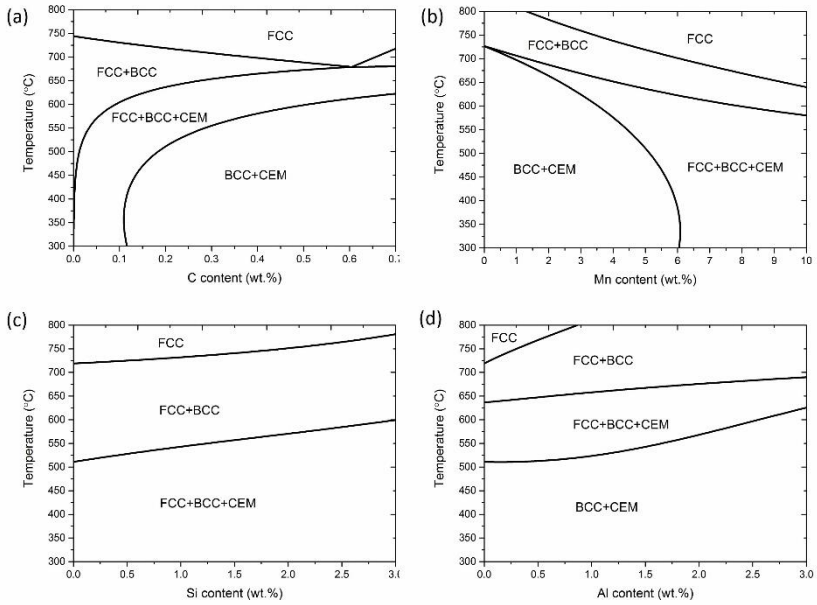

Fig. 29. The effects of C, Mn, Si and Al content on the phase diagram of medium Mn steels. (a) Fe-*x*C-5Mn; (b) Fe-0.2C-*x*Mn; (c) Fe-0.2C-5Mn-*x*Si; (d) Fe-0.2C-5Mn-*x*Al.

5.2. Starting microstructures and processing routes

The starting microstructure of medium Mn steels is usually fully martensitic due to the high hardenability of such steels but some medium Mn steels with a very high Mn content can even contain a small amount of pre-existing austenite in the martensite matrix [309]. To achieve the desired microstructure consisting of ultrafine-grained ferrite and significant amounts of RA, in 1970s the austenite reversion treatment (ART) was proposed by Miller [310] to process medium Mn steels. He was the first to develop a microstructure consisting of an ultrafine-grained ferrite matrix with 10~30 vol. % RA in an Fe-0.11C-5.7Mn steel via austenite reversion starting from an as-quenched martensitic microstructure. **Fig. 30** shows the thermo-mechanical

process for medium Mn steel production routes. The initial martensitic microstructures can be generally divided into two types: hot-rolled and cold-rolled microstructures, which leads to different final microstructures and mechanical properties [290, 311]. The typical microstructure of hot-rolled medium Mn steels after austenite reversion treatment consists of lath-shaped austenite and ferrite (see **Fig. 28a**). For cold-rolled medium Mn steels, recrystallization of the heavily deformed martensite microstructure will proceed simultaneously with austenite formation during ART, leading to ultrafine globular austenite and ferrite (see **Fig. 28b**). Due to the recrystallization, the dislocation density in ferrite of cold-rolled medium Mn steels is often lower than that for hot-rolled grades [311]. In general, two kinds of reverted austenite morphologies, i.e. lath and globular, can be observed [290, 311-314], and the final morphology is strongly affected by the initial microstructure. In addition to hot rolling and cold rolling processes, the warm rolling process was also adopted to control the morphology and sizes of reverted austenite through partial recrystallization [295, 315]. In the conventional ART, the selection of intercritical annealing temperature is essential to control the fraction and stability of the RA. At a higher ART temperature, the kinetics of austenite reversion is fast and as a result the reverted austenite has a relatively low C and Mn content and a larger grain size. This will lead to a low stability of the reverted austenite, of which some will transform into fresh martensite during quenching. At a lower ART temperature, the fraction of reverted austenite is relatively low, although the stability is increased due to a higher degree of C and Mn enrichment and a smaller grain size. At an optimized ART temperature, a desirable balance between the reverted austenite fraction and its thermomechanical stability is achieved, and a maximum amount of austenite upon cooling to ambient temperature can be retained. The ART duration is expected to have a similar effect on the microstructural evolution as the ART temperature. Increasing the ART time would result in more reverted austenite, while it decreases its average C content. As far as the Mn partitioning kinetics is concerned, it is found that the enrichment

of Mn in reverted austenite can approach the equilibrium value within just several minutes [316, 317]. Furthermore, the average grain size of both ferrite and austenite is expected to increase with a longer ART time.

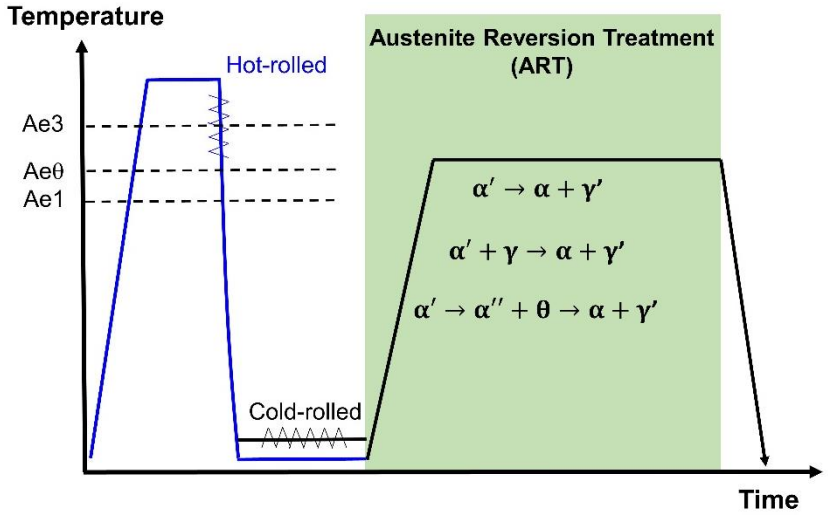

Fig. 30. Thermo-mechanical processing of medium Mn steels via the hot-rolling and the cold rolling routes. α: ferrite; α′: martensite; α″: tempered martensite; γ: austenite; γ′: carbon- and Mn- enriched austenite; θ: cementite.

Several variants of the conventional ART, e.g. double annealing [299, 318-324], cyclic-ART [325], Flash-ART [326], Quenching-ART [327, 328], Intercritical annealing Q&P [326, 329, 330] and two-step intercritical annealing [331] have also been proposed to process medium Mn steels. In the double annealing treatment [318], a first intercritical annealing at a higher temperature is performed to facilitate C and Mn partitioning into the reverted austenite, resulting in the reverted austenite having a large grain size. Due to the insufficient stability, the austenite reverted during the first intercritical annealing would partially transform into fresh martensite during quenching to room temperature. The microstructure after the first intercritical annealing consists of fresh martensite and the recrystallized globular ferrite. Subsequently, during the second annealing at a lower temperature, austenite reverts primarily from the C and Mn enriched fresh martensite, and the newly formed austenite is stabilized by further C and Mn

enrichment. Medium Mn steels processed by the double annealing treatment have a hierarchical microstructure consisting of coarse globular ferrite, ultrafine-grained lath-shaped ferrite and RA. The double annealing treatment, which fine tunes the stability of the reverted austenite, was also found to be effective in eliminating the Lüders band phenomenon in medium Mn steels [332]. Zhu et al. [32] proposed a cyclic austenite reversion treatment to process medium Mn steels. In this variant, the steels are repeatedly heated to a certain intercritical annealing temperature and then quenched to ambient temperature. After several thermal cycles, an increased amount of RA is obtained and the corresponding intercritical annealing time is effectively shortened, as compared with conventional ART, but of course the total processing cycle takes much longer and is more complicated. The Flash-ART process proposed by Wan et al. [326] is another method to obtain more retained austenite effectively. In the Flash-ART process, the cold-rolled steel is flash-heated to a higher intercritical annealing temperature, during which a considerable amount of carbon-enriched austenite is reverted. Subsequently, it is cooled to a lower intercritical annealing temperature and hold for Mn partitioning from martensite into austenite. During this stage, a Mn-enriched shell is formed due to sluggish kinetics of Mn partitioning. It is found that reverted austenite with a core-shell structure can be effectively retained to ambient temperature. It is also expected that mechanical stability of the core-shell RA grains could be different from the conventional RAs, which would affect mechanical performance. This needs to be further investigated.

The Quenching-ART [327, 328] and Intercritical annealing-Q&P [329, 330] processes were proposed to process medium Mn steels by combining the advantages of conventional Q&P and ART processes. During the Quenching-ART process, the steels are firstly turned into a fully austenitic state and then quenched to a temperature between Ms and M_f in order to obtain a mixed microstructure of martensite and pre-existing austenite, and the subsequent austenite reversion proceeds via new nucleation of reverted austenite and the growth of pre-existing

austenite. It was found that the newly formed Mn enriched shell adjacent to the pre-existing austenite was retained to room temperature while the pre-existing austenite core was back transformed into martensite because of its lower thermal stability. The final microstructure of the Quenching-ART processed steels consists of ultrafine-grained ferrite and austenite, as well as a small amount of fresh martensite. The observed increase in strength of the Quenching-ART processed steels was attributed to the presence of a small amount of fresh martensite. During the Intercritical annealing-Q&P process [329], the medium Mn steels are first intercritically annealed to obtain an austenite-ferrite mixture, which is followed by a Q&P treatment to further enhance austenite stability via additional carbon partitioning. The Intercritical annealing-Q&P processed medium Mn steels, which consist of ultrafine-grained ferrite, RA and tempered martensite, show no Portevin-Le Chatelier (PLC) effect and have a higher ultimate strength than the conventional ART processed counterparts.

Actually, cementite precipitation could also occur during the processing of medium Mn steels. Taking the advantage of cementite precipitation before austenite reversion, Hu and Luo [331] proposed a two-step intercritical annealing process to obtain retained austenite in medium Mn steels. In the two-step intercritical annealing process, cementite precipitation is carefully tailored via annealing at a lower temperature before austenite reversion, and then reverted austenite can nucleate at the cementite/martensite interfaces during a shorter intercritical annealing at a higher temperature. The growth of reverted austenite from the mixture of cementite and tempered martensite led to the heterogeneous Mn distribution in reverted austenite after the two-step intercritical annealing process. The reverted austenite is partially transformed into martensite during quenching to ambient temperature, which results in a considerable amount of retained austenite with adjacent to martensite. It was found that such a microstructure is beneficial to both the strength and the ductility of medium Mn steels.

In summary, the microstructure of medium Mn steels either processed from a hot-rolled or cold rolled starting state is mainly tuned via phase transformations during the subsequent ART process, as shown in **Fig. 30**. The fundamentals of the key phase transformations during the ART process are reviewed below.

5.3. Critical phase transformations

The simultaneous partitioning of C and Mn from the initial martensite into the transient austenite during ART significantly enhances the thermal stability of the reverted austenite, and thus a certain amount of austenite is retained upon quenching to ambient temperatures. It can be easily expected that for a certain composition the amount of RA that can be achieved is strongly linked to the ART temperature. De Moor et al. [333] proposed a simplified thermodynamic method to predict the fraction of RA as a function of intercritical annealing temperature. First the fraction of reverted austenite and its composition after intercritical annealing is estimated by assuming full equilibrium, and then the amount of austenite that can be retained to room temperature is further estimated by the K-M equation considering the composition of the reverted austenite. As shown in **Fig. 31**, the fraction of RA is predicted to reach a maximum value at an optimum intercritical annealing temperature, which is in qualitatively agreement with the experiments. As such the concept of the optimal annealing temperature resembles that for Q&P steels explained in chapter 4. Using this thermodynamic approach, systematic calculations were performed to investigate the effects of C, Mn, Al, Si and Cr partitioning on the fraction of RA [334]. It was predicted that Mn is much more effective than C in enhancing the final RA fraction. This is because the equilibrium Mn content in reverted austenite decreases with increasing C content. Addition of ferrite stabilizers (e.g. Al or Si) could decrease the maximum amount of RA and increase the optimum intercritical

annealing temperature. The processing window to obtain a considerable amount of RA was predicted to be enlarged by Cr addition. The thermodynamic method proposed by De Moor et al. has been used widely to optimize processing parameters for medium Mn steels [335-342].

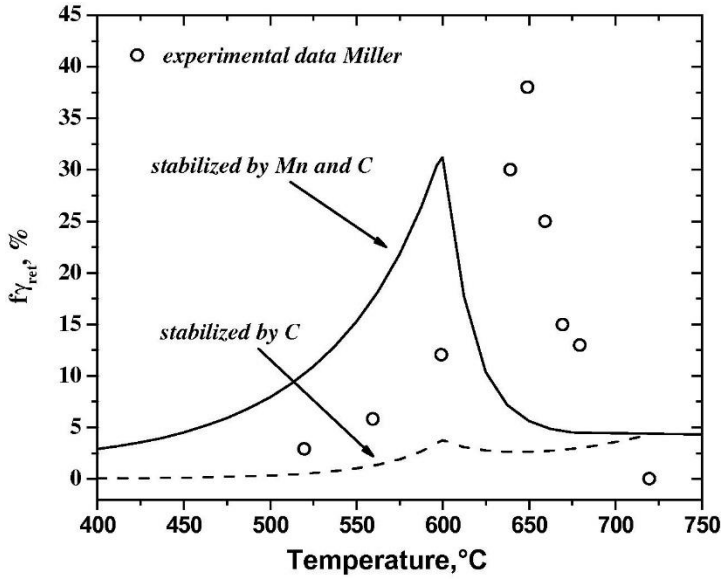

Fig. 31. RA fraction as a function of intercritical annealing temperature based on the full equilibrium thermodynamics and K-M equation calculation [333].

In general, thermodynamic calculations are expected to be in reasonable agreement with experiments when the ART time is long enough to reach the full equilibrium state. However, for industrial production schedules the ART time is limited, and thus kinetic details should be carefully considered. Actually, besides austenite formation, carbide precipitation/dissolution could also occur during ART, which would affect the kinetics of austenite formation and the final microstructure. Therefore, the phase transformation behaviour in medium Mn steels during ART is much more complex than we expected, and a self-consistent understanding is still lacking. In the literature, much effort has been paid to investigate the kinetics of martensite/austenite interface migration and alloying elements partitioning, carbide precipitation/dissolution and their effects on austenite formation, etc., which are all important issues for precisely controlling the microstructure of medium Mn steels.

5.3.1. Austenite reversion from martensite or martensite-austenite mixture

The kinetics of austenite growth (e.g. the martensite/austenite interface migration) and alloying elements partitioning during austenite reversion of medium Mn steels usually have been simulated using the local equilibrium (LE) model [57, 299, 343-346]. **Fig. 32a** shows the kinetics of austenite reversion in an Fe-0.2C-5Mn medium Mn steel simulated by the LE model.

(i) NPLE-($\alpha' \rightarrow \gamma$), i.e. Stage I in **Fig. 32a**, during which the kinetics of martensite/austenite interface migration is controlled by carbon diffusion in martensite while a concentration spike of Mn forms ahead of the interface. In this stage, the kinetics of martensite/austenite interface migration is very fast and controlled by carbon diffusion in martensite (see **Fig. 32b**). Although the NPLE-($\alpha' \rightarrow \gamma$) stage is very short (about 10^{-3} second), the size of the reverted austenite at the end of this stage is significantly increased and is strongly affected by the initial thickness of martensite lath.

(ii) PLE-($\alpha' \rightarrow \gamma$), i.e. Stage II and III in **Fig. 32a**, during which the kinetics of martensite/austenite interface migration is controlled by Mn diffusion in martensite and as a result the Mn concentration in the reverted austenite is gradually enhanced (see **Fig. 32c**). A kinetic plateau was predicted to occur due to the NPLE/PLE transition [343, 344].

(iii) PLE-($\gamma \rightarrow \alpha'$), i.e. Stage IV in **Fig. 32a**, during which the martensite/austenite interface migrates backward into the austenite. Its kinetics is very sluggish and controlled by Mn diffusion in austenite (see **Fig. 32a** and **c**). Hence, the growing fraction of reverted austenite first exceeds the full equilibrium fraction and then approaches it by shrinking.

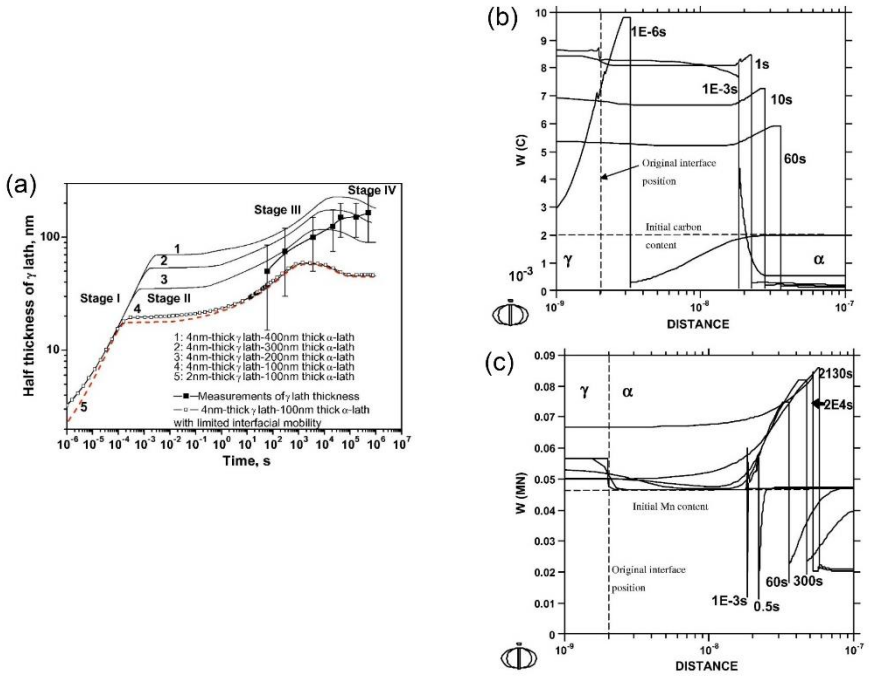

Fig. 32. (a) The influences of simulation cells on the kinetics of austenite reversion at 650°C in an Fe-0.2C-5Mn steel simulated by DICTRA based on LE model. Evolution of (b) C and (c) Mn profiles across the interface during intercritical annealing, corresponding to curve No. 5 in (a) [343].

In general, the LE model can qualitatively predict the basic features of austenite reversion [342, 343]. However, the thickening kinetics of reverted austenite predicted by the LE model, in particular at the early stage of austenite reversion, is usually much faster than that measured in experiments. This could be attributed to the infinite interface mobility of martensite/austenite assumption in the LE model. The mobility of martensite/austenite interface in medium Mn steels may not be infinite either, and thus a certain amount of Gibbs energy would be dissipated due to interface friction. As shown in **Fig. 32a**, Luo et al. [343] found that the kinetics of austenite reversion is marginally affected by interface mobility if the mobility of martensite/austenite interface is assumed to be identical to that of the ferrite/austenite interface. Zhang et al. [312, 313] found that the lath-shaped reverted austenite usually holds a near K-S

orientation relationship with all the adjacent martensite in an Fe-0.3C-2Mn-1.5Si steel. The interface with K-S orientation relationship has a better coherent interfacial structure when compared to the non-K-S orientation relationship. Thus, it is reasonable to assume that the mobility of the martensite/austenite interface could be lower than that of the ferrite/austenite interface. Taking the mobility of ferrite/austenite interface ($M_0 = 4 \times 10^{-7} \exp(-140000/RT)\, m^4/Js$) as a reference, Zhang et al. [313] utilized a mixed-mode model to simulate the kinetics of austenite reversion and alloying elements partitioning behaviour in an Fe-0.3C-2Mn-1.5Si steel. The comparison between the predicted and measured thickness of lath-shaped austenite annealed at 750°C and 775°C are shown in **Fig. 33a** and **b**, respectively. It was found that the kinetic plateau caused by the NPLE/PLE transition at the early stage disappears and the kinetics of austenite reversion is significantly decelerated by decreasing the value of interface mobility. Mn and Si partitioning behaviour across the interface at 775°C for the M_0 and $0.001M_0$ cases is shown in **Fig. 33c** and **d**, respectively. It can be seen that a more significant partitioning of Mn and Si across the interface occurs with a lower interface mobility. The model predictions are found to be in good agreement with experiments when interface mobility was assumed to be about $0.001M_0$. Technically, the steel used by Zhang et al. does not belong to the class of medium Mn steels, but the basic features of austenite reversion should be similar as that in medium Mn steels.

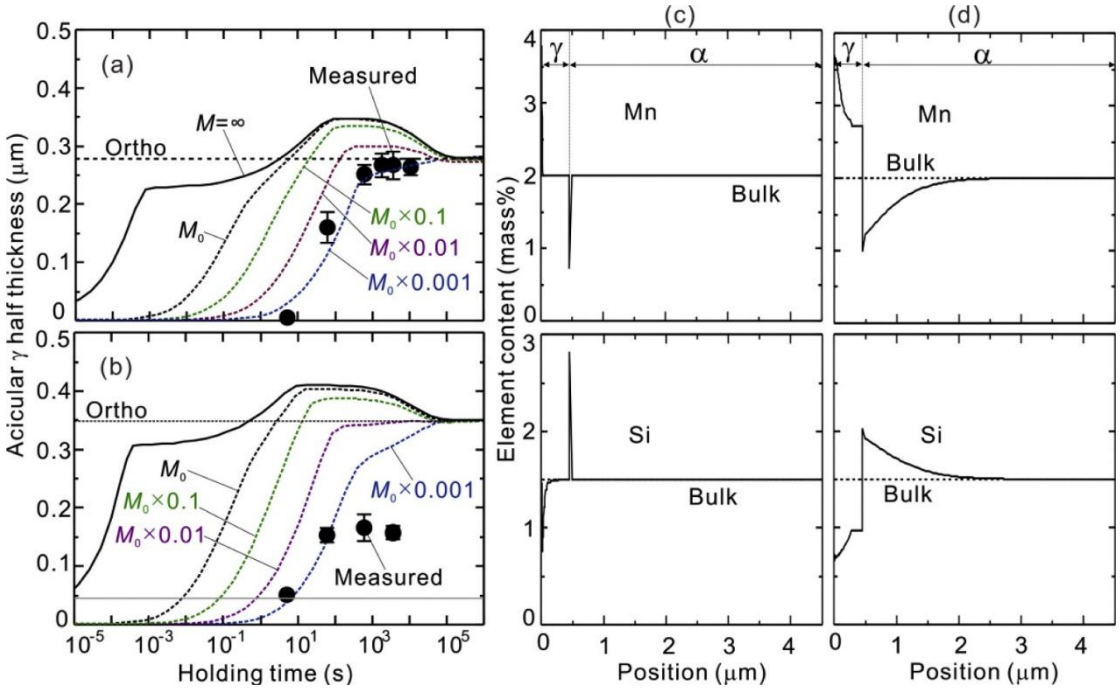

Fig. 33. The effects of interface mobility on the kinetics of austenite reversion at (a) 750°C and (b) 775°C in an Fe-0.3C-2Mn-1.5Si steel. Solid circles in (a) and (b) indicate the experimentally measured thickness of austenite lath. Mn and Si profiles in austenite and martensite at 775°C when the interface mobility is (c) M_0 and (d) $0.001M_0$. [313]

In medium Mn steels with a high Mn content, the initial microstructure before ART could be a martensite-austenite mixture instead of a full martensite microstructure. The kinetics of austenite reversion and alloying elements partitioning behaviour from the mixed microstructures consisting of martensite and pre-existing austenite can be expected to be different from that starting from a fully martensitic microstructure [327, 328]. Dmitrieva et al. [347] investigated the growth of pre-existing austenite into martensite in a so-called maraging-TRIP steel with 12 wt. % Mn. As shown in **Fig. 34a** and **b**, a Mn enriched layer with a thickness of ~10 nm enveloping the pre-existing austenite was experimentally identified after annealing at 450°C for 48 hours, which leads to a special type of RA with a Mn gradient. DICTRA simulations based on the LE assumption were performed to replicate this type of RA, and it was

found that the simulations could fit with experiments when diffusivity of Mn in martensite is artificially increased by a factor of 45. Alternatively, a mixed-mode model, using the mobility of martensite/austenite interface as an adaptable parameter, has also been used to successfully mimic the Mn profile in this RA. It is worth noting that the effective mobility of martensite/austenite interface used by Dmitrieva et al. [347] is only smaller than that estimated using $0.001M_0$, as suggested by Zhang et al. [313], in an order of magnitude, although the chemical composition and processing condition for two cases are quite different.

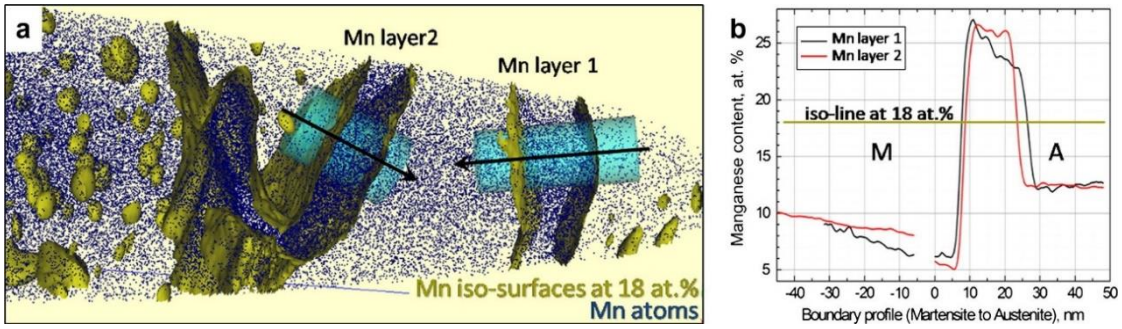

Fig. 34. (a) Mn atoms and 18 at. % Mn iso-concentration surfaces from a mar-aging TRIP steel annealed at 450°C. (b) The Mn concentration gradient across the martensite/austenite interface [347].

Tsuchiyama et al. [327] intentionally created an initial microstructure consisting of martensite and pre-existing austenite in an Fe-0.1C-5Mn-1.2Si-0.02Al steel by quenching the steel from a fully austenitic state to a temperature between the Ms and the M_f temperature. 20% of pre-existing austenite was preserved before austenite reversion at 650°C. DICTRA simulations based on the LE model indicated that the growth of pre-existing austenite is accompanied by C and Mn partitioning from martensite into the austenite present. Due to the low diffusivity of Mn in austenite and the fast martensite/austenite interface migration, the Mn content in the austenite near the interface is much higher than that in the centre of the austenite, which leads to a Mn gradient in the austenite grain. The Mn enriched region of austenite is

retained upon quenching to room temperature while the central low Mn region is transformed into fresh martensite. A systematic study on an Fe-0.2C-8Mn-2Al steel was performed by Ding et al. [328] to investigate the kinetics of austenite reversion from a mixture of pre-existing austenite and martensite with various amounts of pre-existing austenite. It was interestingly found that austenite reversion would still proceed even when the fraction of the pre-existing austenite is already higher than the equilibrium value at the intercritical annealing temperature.

Austenite reversion is usually considered to be a diffusion-controlled reaction, but the other mechanisms, e.g. diffusionless or diffusional massive, have also been discussed in the literature [348-350]. Han et al. [348] investigated the influence of heating rate on austenite reversion in a series of cold-rolled Fe-0.05C-(5, 7, 9) Mn steels. The initial microstructure consisted of a deformed martensite without carbides and some RA. It was found that when heating rate is higher than 15°C/s, the austenite starting temperature became heating rate independent, and reverted austenite without Mn enrichment was observed in the final microstructure. Hence, Han et al. [348] suggested that austenite reversion occurs in a diffusionless way in case the heating rate exceeds 15°C/s. Recently, Yang et al. [350] further found that the start temperature of austenite reversion is located between T_0 and T_0', and the kinetics of austenite reversion is accelerated by pre-deformation during heating at a rate of 50°C/s in the cold-rolled Fe-0.05C-9Mn steel. As these phenomena are inconsistent with the diffusionless mechanism assumptions, they argued that austenite reversion occurs in the diffusional massive mechanism, rather than the diffusionless mechanism, during rapid heating. Yang et al. [349] also investigated the mechanism of austenite reversion during continuous heating from a microstructure consisting of ferrite and deformation-induced martensite in an Fe-0.28C-6.22Mn-1.57Si steel. They found that the amount of austenite reverted between 300°C and 500°C is not dependent on heating rate (see **Fig. 35b** and **c**), while it is reduced by increasing the rolling reduction of the steels (see **Fig. 35a**). The later phenomenon was also

termed ‘mechanical stabilization of martensite’, which the authors regarded as a unique feature of diffusionless phase transformation. Hence, Yang et al. [349] suggested that austenite reversion during heating from 300°C to 500°C occurs in a diffusionless way. At higher annealing temperatures, the amount of reverted austenite was found to be dependent on heating rate and to be enhanced by increasing rolling reduction, which indicates that under these conditions austenite reversion proceeds in a diffusional manner.

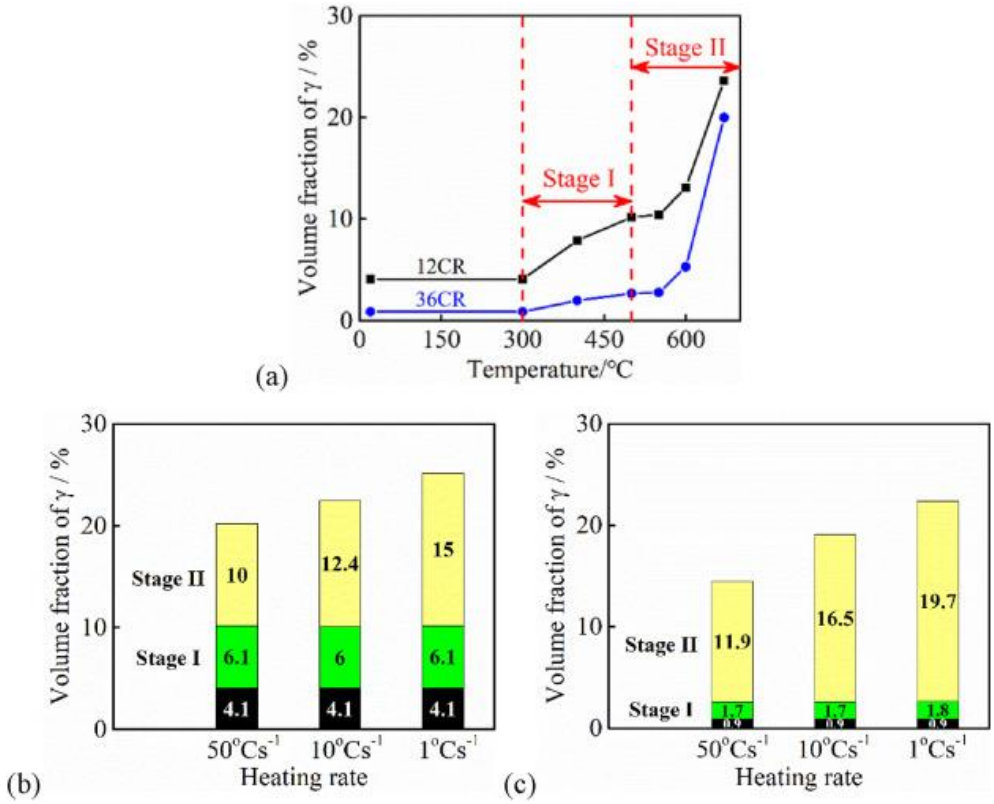

Fig. 35. (a) The evolution of reverted austenite fraction during continuous heating at a heating rate of 10°C/s for the Fe-0.28C-6.22Mn-1.57Si steels with a thickness reduction of 12% (12CR) and 36% (36CR). Reverted austenite fraction during continuous heating as a function of heating rate for (b) 12CR and (c) 36CR steels [349].

5.3.2. Interaction between carbide precipitation-dissolution and austenite reversion

Carbide precipitation-dissolution and austenite reversion are expected to interact with each other, which significantly increases the complexity of the analysis and prediction of the microstructure evolution during ART. The kinetic competition between carbide precipitation and austenite reversion in a cold-rolled Fe-0.1C-7Mn-0.5Si medium Mn steel annealed at 450°C ($\alpha+\gamma+M_{23}C_6$ region in phase diagram) was studied by Kwiatkowski da Silva et al. [351] They found that, due to co-segregation of C and Mn into grain boundaries and dislocations, carbides were found to precipitate before the onset of austenite reversion and retard the nucleation of austenite. Wu et al. [352] investigated the interaction between carbide precipitation-dissolution and austenite reversion in an as-quenched Fe-0.2C-5Mn medium Mn steels annealed at 600°C ($\alpha+\gamma$+cementite region in phase diagram). Cementite was also found to form prior to the austenite revision, while the cementite/martensite interface served as the nucleation site for austenite reversion. The composition of the cementite is expected to play an important role in the subsequent austenite reversion from martensite-cementite mixture, and thus the effect of bulk C and Mn content on the composition of cementite was investigated by Wu et al. [352]. It was found that the C level has a marginal effect on the Mn partitioning into cementite while the Mn level in cementite was found to increase with increasing bulk Mn concentration.

In principle, medium Mn steels are usually processed via intercritical annealing at two phase ($\alpha+\gamma$) annealing region. Cementite precipitation could take place during heating to intercritical annealing region and/or holding at the early stage of intercritical annealing. Lee et al. [353] found that cementite could still form before austenite reversion during continuous heating at a rate of 4 °C/s in a medium Mn steel containing a higher amount of Si and Al (Fe-0.3C-10Mn-2Si-3Al, wt. %). This is because the retarding effect of Si and/or Al on cementite precipitation is decreased by the enhanced diffusivity of Si and/or Al at higher annealing

temperature [313, 353]. Lee et al. [353] found that the derivative of the dilatation to temperature during heating can be divided into two distinct stages. The first stage was ascribed to the formation of cementite while the second stage was attributed to austenite reversion [353, 354]. It was further confirmed by Lee et al. [353] that spherical cementite with a diameter of 20~50 nm preferentially nucleates at the low-angle sub-grain boundaries and martensite lath boundaries in the first stage, and then austenite nucleates at cementite/martensite interface in the second stage. Han and Lee [348] investigated the influence of heating rate on cementite precipitation and austenite reversion in a series of cold-rolled Fe-0.05C-(5, 7, 9)Mn steels. They found that cementite precipitation could occur when the heating rate was less than 15°C/s. Both the starting temperatures of the cementite precipitation and austenite reversion were found to increase with increasing heating rate. At heating rates above 15°C/s, cementite precipitation was found to be fully inhibited, and the starting temperature of austenite reversion then became independent of the heating rate. Luo et al. [309, 343, 355] systematically investigated the influence of heating rate on carbide precipitation-dissolution and austenite reversion in an as-quenched Fe-0.2C-5Mn steel annealed at 650°C. It was found that a low heating rate of 1°C/s would allow sufficient time for cementite precipitation and alloying elements partitioning from martensite into cementite. Cementite should provide nucleation sites for the subsequent austenite reversion, while the driving force for austenite reversion was reduced due to Mn enrichment in cementite and a reduced carbon content in martensite. Hence, it was found that the overall kinetics of austenite reversion was decelerated by cementite precipitation. With an increasing heating rate (from 1 °C/s to 10, 50 or 100 °C/s), cementite was still found to form within the martensite matrix, while there is no Mn partitioning into cementite due to the time available being insufficient. As a result, the kinetics of austenite reversion at 650°C with a heating rate of 10, 50 or 100 °C/s was found to be much faster than that with a heating rate of 1°C/s. It is expected that carbide formation upon heating could be fully suppressed by an ultra-

fast heating rate, while carbides form during the isothermal intercritical annealing [309, 313]. Indeed, Luo et al. [309] found that cementite could still precipitate at the early stage of isothermal intercritical annealing after rapid heating of 300°C/s. As shown in **Fig. 36**, rod-like cementite with a diameter of 15~35 nm could precipitate in martensite (see **Fig. 36a**) and some reverted austenite could nucleate at cementite/martensite interface (see **Fig. 36b** and **c**) in an Fe-0.2C-5Mn steel after intercritical annealing at 650°C for 5 minutes. It was suggested that cementite seems to have a kinetic advantage over austenite to precipitate in martensite matrix containing a high density of defects and super-saturated carbon at the early stage of intercritical annealing [309, 355], although cementite is not thermodynamically stable in the intercritical two phase ($\alpha+\gamma$) annealing region.

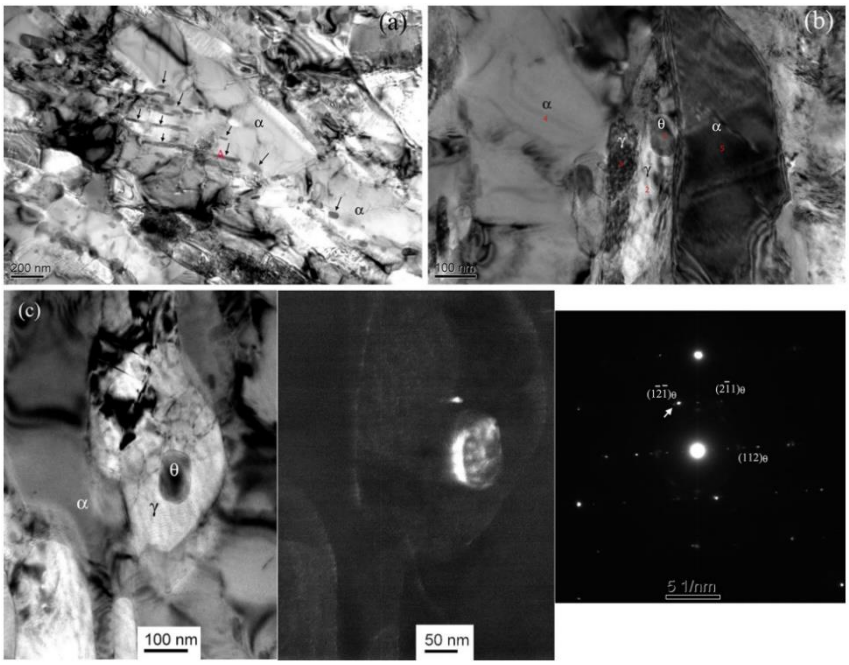

Fig. 36. TEM images of the microstructures after intercritical annealing at 650°C for 5 min in an Fe-0.2C-5Mn steel. (a) Cementite precipitation in martensite. Cementite is indicated by arrows in (a). (b) and (c) Cementite particles surrounded by reverted austenite [309].

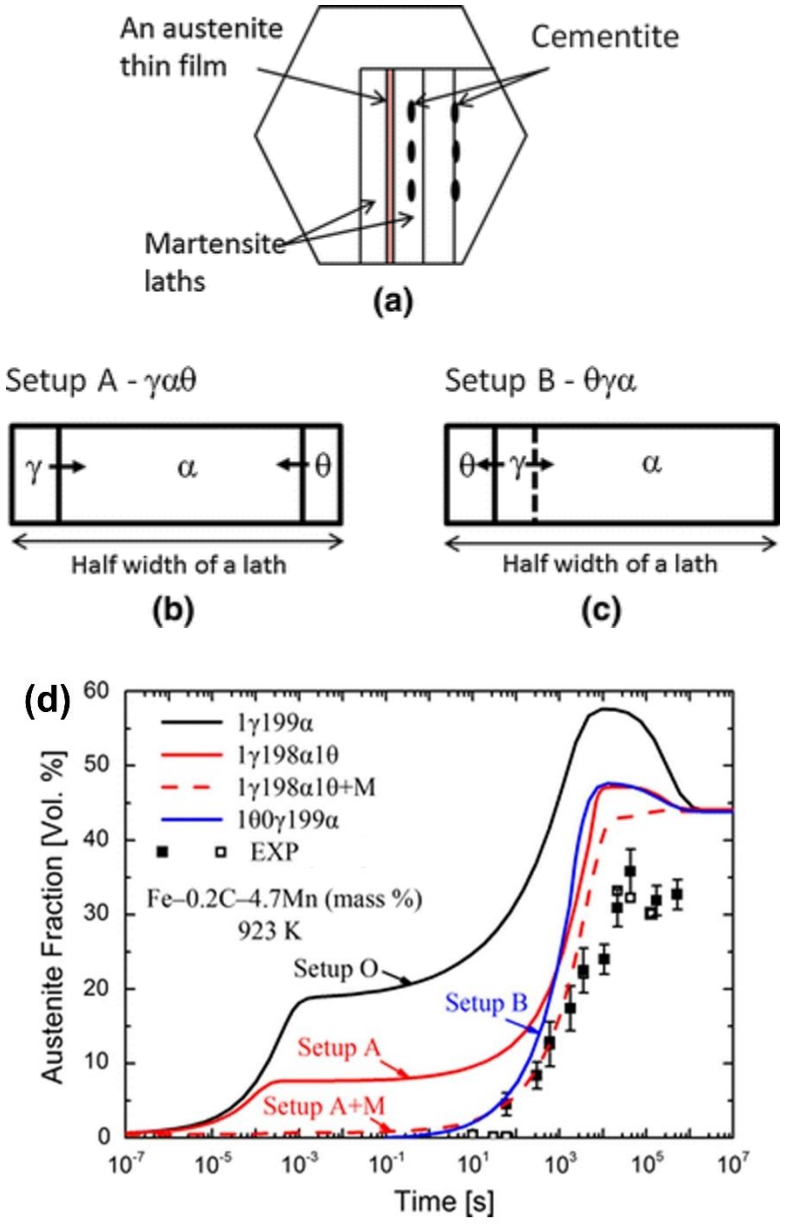

Fig. 37. (a) Schematic illustration showing the microstructures during intercritical annealing. Simulation conditions for austenite nucleation at (b) martensite laths (Setup A) and (c) martensite/cementite interface (Setup B). (d) The kinetics of austenite reversion under different simulation conditions simulated by DICTRA. Setup O: austenite nucleation at martensite lath and no cementite precipitation is assumed. Setup A+M: martensite/austenite interface mobility effect included [356].

As discussed above, the interaction between carbide precipitation-dissolution and austenite reversion during ART depends on many factors and is very complex. In order to better understand this complex phenomenon, many efforts were made to simulate carbide precipitation-dissolution and austenite reversion using DICTRA software [331, 356-361]. As shown in **Fig. 37a**, there are various setups for the simulations of austenite reversion from martensite-cementite mixture:

(i) Setup A, reverted austenite nucleates at martensite lath boundaries and its growth is affected by cementite precipitation-dissolution in martensite (see **Fig. 37b**). As discussed in section 5.3.1, the effect of martensite/austenite interface mobility on the kinetics of austenite reversion can also be considered, i.e. Setup A+M.

(ii) Setup B, cementite precipitates in martensite at the early stage of annealing. Subsequently, reverted austenite nucleates at martensite/cementite interface and then envelops cementite (see **Fig. 37c**). However, due to the limitation of the DICTRA software, the effect of martensite/austenite interface mobility on the kinetics of austenite reversion could not be considered.

Huyan et al. [356] simulated the kinetics of austenite reversion of an as-quenched Fe-0.2C-5Mn medium Mn steel annealed at 650°C using various setups, as shown in **Fig. 37d**. The growth kinetics of austenite reversion from martensite without considering cementite precipitation is shown there as Setup O. The simulations based on Setup A indicated that kinetics of austenite reversion can be divided into three stages, and a plateau due to the NPLE/PLE transition was also predicted. The kinetics of austenite reversion was predicted to be decelerated due to cementite precipitation. It was also found by Huyan et al. [356] that the predicted kinetics of austenite reversion can be in good agreement with experiments if a finite mobility of the martensite/austenite interfaces is assumed in the setup A simulations, e. g. Setup A+M. Zhang et al. [313] reported that the kinetics of lath-shaped austenite reversion and

alloying elements partitioning behaviour in the low Mn steels can also be well predicted based on Setup O+M, assuming the mobility of martensite/austenite interface is much lower than that of ferrite/austenite interface. It should be noted that the effect of cementite precipitation on the kinetics of austenite reversion was not considered in Setup O+M, although cementite precipitation was observed by Zhang et al. [313]. This could explain why the mobility of martensite/austenite interface adopted by Zhang et al. [313] is smaller than that adopted by Huyan et al. [356].

It has also been frequently observed that reverted austenite could nucleate at a martensite/cementite interface and envelops the cementite at a later stage [309, 355]. Setup B would be appropriate for this case. Huyan et al.'s simulations based on Setup B indicated that cementite could precipitate firstly under NPLE mode and then dissolve. Interestingly, it was found in the simulations based on setup B that austenite appears and grows only when cementite starts to dissolve, while austenite could start to grow from the beginning, as is assumed in the simulations based on setup A. In DICTRA simulations, cementite precipitation is usually predicted to proceed under NPLE mode. However, for many cases, Mn-enriched cementite could form before austenite reversion [353, 358]. Zhang et al. [313] simulated the kinetics of austenite reversion from martensite-cementite matrix with significant alloying elements redistribution, and found that the kinetics of austenite reversion is strongly retarded by Mn enrichment in cementite. Besides, it has also been reported by Lee et al. [353] that the growth of austenite is controlled by cementite dissolution, and the average C and Mn content in cementite is expected to play an important role in the kinetics of austenite reversion.

In summary, carbide precipitation and dissolution play a complex role in austenite reversion. For most cases, the overall kinetics of austenite reversion in conventional ART was decelerated by carbide precipitations, as C and Mn enrichment in carbides reduces the driving force for austenite growth. However, it has also been reported by Luo et al. [331, 355] and Liu

et al. [362] that the overall kinetics of austenite reversion can be accelerated by transition carbides or para-cementite precipitation without Mn enrichment being formed at lower pre-tempering temperatures. This implies that the provision of enough nucleation sites would be of dominant importance. The mechanism of carbide precipitation-dissolution and its effects on austenite reversion still needs further investigation.

6. Summary and prospects

Mechanical properties of AHSSs are strongly linked to the properties of the matrix but also to the amount of RA and its stability, and thus a precise control of RA is of great importance. Here we reviewed the relationship between steel composition, processing routes and resulting microstructures for the TRIP steels, CFB steels, Q&P steels and medium Mn steels, with an emphasis on the critical solid-state phase transformations involved in the different processing routes to tune the fraction and the stability RA. In general, RA can be introduced into the various matrix options, e.g. ferrite, bainitic ferrite, or tempered martensite. These AHSSs all having comparable compositions and belonging to the Fe-C-Mn or Fe-C-Mn-Si/Al systems but are created via different phase transformations. Conceptually, the phase transformations responsible for the final RA obtained in the various processing routes can be divided into two categories: austenite decomposition and austenite reversion. The RA in TRIP, CFB and Q&P steels is mainly tuned via austenite decomposition (e.g. austenite-ferrite transformation, bainitic transformation and martensitic transformation), while austenite reversion treatment is used to control the RA in medium Mn steels. Austenite decomposition and reversion are all accompanied by carbon and alloying elements partitioning, which is the key to stabilize whatever austenite is present at the end of the higher temperature heat treatment upon cooling to room temperature. Carbide formation in or around the RA is generally seen as undesirable as its formation consumes carbon atoms and reduces the thermal stability of austenite. It can be suppressed by the current alloying strategy (adding Si, Al or P).

While the main phase transformation concepts behind the multi-stage heat treatments in the generation of the four AHSS families presented are well enough understood, there are still a number of unresolved issues regarding the principal phase transformations for each steel grade that require further exploration:

TRIP steels: As TRIP steels were the first generation of AHSS families using controlled amounts of RA as a means to get more attractive combinations of tensile strength and ductility, they have been well studied and we understand a lot of the principal phase transformations. While conceptually attractive, it is also clear that the shape and property diversity in the various phases to be created (ferrite, bainite, martensite and RA) and the mutual dependence of their formation, made it hard to develop stable production protocols for commercial production lines. As a result, the commercial production of TRIP steels did not reach the production volumes once anticipated. A particular aspect which would have been nice to understand better is how the preceding intercritical annealing treatment influences the following bainite formation as well as the size and carbon concentration of the austenite at the end of the IBT process.

CFB steels: The mechanism of bainite formation in CFB steels as well as in TRIP steels is still controversial. More dedicated experiments/characterisation and more realistic models are required to quantify the dependence of energy barrier for bainitic transformation on both the temperature and alloying composition. Similar to Fe-C-Mn-Si based CFB steels, Fe-C-Mn-Al based CFB steels are expected to be of practical interest. However, bainite formation in Fe-C-Mn-Al steels has not been investigated extensively. In particular, the effects of Al addition on the kinetics of bainitic transformation and carbon partitioning need to be further explored. The effects of Al addition on carbide formation during bainitic transformation, as well as the influence on the stability of RA also need to be investigated.

Q&P steels: While the Q&P process seems relatively straightforward we still need to resolve the following key issues: *(i)* Austenite decomposition due to bainitic transformation and/or martensite/austenite interface migration has been experimentally detected during partitioning. Further experimental and modelling studies are required to improve our understanding of austenite decomposition behaviour during the Q&P process. *(ii)* It has been widely observed that carbide formation could not be fully suspended by Si or Al addition.

However, there are conflicting views about the mechanism of carbide precipitation, in particular that of the transition carbides, as it is quite challenging to precisely measure carbide precipitation behaviour during the Q&P process even with the most modern characterisation techniques. Therefore, further efforts are required to reveal the mechanism of carbide precipitation to yield a quantitative understanding of the effects of Al/Si on carbide formation in Q&P steels. *(iii)* Carbon partitioning, carbide formation, bainitic transformation and martensite/austenite interface migration are expected to interact with each other, which makes the microstructure evolution during the Q&P process very complex. A self-consistent model is required to describe the complex kinetic interactions during the Q&P process.

Medium Mn steels: The principle phase transformation behaviour during the processing of medium Mn steels is relatively clear, but carbide precipitation/dissolution and its effects on austenite reversion is still barely understood. The effects of heating rate and austenite reversion temperature on carbide precipitation/dissolution and austenite reversion still need to be further investigated, which would provide new insights for the novel microstructure designs in medium Mn steels.

Some common issues for all AHSSs which need to be explored are listed below:

2 or 3D computational simulations of microstructure evolution of AHSSs. Up to now mainly 1D thermo-kinetic models have been developed to predict the phase constituents and the partitioning of alloying elements as a function of the alloy composition and processing parameters. However, in addition to phase fractions and their separate compositions, the morphology/size of RA as well as the phase distribution have been found to play a significant role in the mechanical behaviour of the modern AHSSs. 2D or 3D thermo-kinetic models, which could provide details of their morphology and spatial arrangement, are required to design the complex microstructure of AHSSs in a more precise manner.

Phase transformations during flash annealing of AHSSs. During the conventional processing of AHSSs, the heating rate is relatively slow, and phase transformations and microstructure evolution upon heating proceed in a near-equilibrium manner. Recently, flash heating technology has been successfully applied to process AHSSs including DP, TRIP, Q&P and medium Mn steels, and it was found that mechanical properties of flash annealed steels could be remarkably improved. Flash heating leads to very complex interactions between recrystallization, carbide formation/dissolution, austenite formation and elements partitioning during heating of AHSSs, and the relevant phase transformations and microstructure evolution are far-from-equilibrium. This affects the phase transformations and microstructure evolution during the subsequent heat treatments. While flash heating enhances the complexity of phase transformations and microstructure evolution, it indeed opens a new dimensionality of microstructural architecturing in steels and provides large opportunities to create novel and interesting microstructures which cannot be obtained by the conventional processing. Efforts are required to improve the qualitative and quantitative understanding of the complex phase transformations and microstructure evolution during flash annealing of AHSSs.

Acknowledgements

H. Chen acknowledges financial support from the National Natural Science Foundation of China (Grant 51922054, U1860109, U1808208 and U1764252), Beijing Natural Science Foundation (2182024), National Key R&D program of 6Y7 China (2016YFB0300104). Z.-G. Yang acknowledges financial support from the National Natural Science Foundation of China (Grant 51771100). S. van der Zwaag acknowledges a Chinese National 1000 Talent Foreign Scholar grant awarded in 2018.

References

[1] N. Fonstein, Evolution of Strength of Automotive Steels to Meet Customer Challenges, Advanced High Strength Sheet Steels, Springer, Cham, 2015, pp. 1-16.

[2] C.C. Tasan, M. Diehl, D. Yan, M. Bechtold, F. Roters, L. Schemmann, C. Zheng, N. Peranio, D. Ponge, M. Koyama, K. Tsuzaki, D. Raabe, Annu. Rev. Mater. Res. 45 (2015) 391-431.

[3] O. Bouaziz, H. Zurob, M. Huang, Steel Res. Int. 84 (2013) 937-947.

[4] N. Fonstein, Advanced high strength sheet steels：Physical Metallurgy, Design, Processing,and Properties, Springer.

[5] J.M. Rigsbee, P.J. VanderArend, Formable HSLA and Dual Phase Steels, in: A.T. Davenport (Ed.) The Metallurgical Sociey of AIME, 1979, p. 56.

[6] P. Jacques, Q. Furnémont, A. Mertens, F. Delannay, Philos. Mag. A 81 (2001) 1789-1812.

[7] O. Grässel, L. Krüger, G. Frommeyer, L.W. Meyer, Int. J. Plast. 16 (2000) 1391-1409.

[8] B.C. De Cooman, Curr. Opin. Solid State Mater. Sci. 8 (2004) 285-303.

[9] K.-i. Sugimoto, T. Hojo, J. Kobayashi, Mater. Sci. Technol. 33 (2017) 2005-2009.

[10] J. Speer, D.K. Matlock, B.C. De Cooman, J.G. Schroth, Acta Mater. 51 (2003) 2611-2622.

[11] A.J. Clarke, J.G. Speer, M.K. Miller, R.E. Hackenberg, D.V. Edmonds, D.K. Matlock, F.C. Rizzo, K.D. Clarke, E. De Moor, Acta Mater. 56 (2008) 16-22.

[12] D.W. Suh, J.H. Ryu, M.S. Joo, H.S. Yang, K. Lee, H.K.D.H. Bhadeshia, Metall. Mater. Trans. A 44 (2012) 286-293.

[13] D.-W. Suh, S.-J. Kim, Scr. Mater. 126 (2017) 63-67.

[14] J. Zhao, Z. Jiang, Prog. Mater. Sci. 94 (2018) 174-242.

[15] P.J. Jacques, Curr. Opin. Solid State Mater. Sci. 8 (2004) 259-265.

[16] R. Kuziak, R. Kawalla, S. Waengler, Arch. Civ. Mech. Eng. 8 (2008) 103-117.

[17] X. Zhu, W. Li, H. Zhao, X. Jin, Int. J. Hydrogen Energy 38 (2013) 10694-10703.

[18] D.J. Dyson, J. Iron Steel Res. Int. 208 (1970) 469-474.

[19] M. Onink, C.M. Brakman, F.D. Tichelaar, E.J. Mittemeijer, S. van der Zwaag, J.H. Root, N.B. Konyer, Scr. Metall. Mater. 29 (1993) 1011-1016.

[20] N. Vandijk, A. Butt, L. Zhao, J. Sietsma, S. Offerman, J. Wright, S. Vanderzwaag, Acta Mater. 53 (2005) 5439-5447.

[21] C.P. Scott, J. Drillet, Scr. Mater. 56 (2007) 489-492.

[22] K.Y. Zhu, C. Mager, M.X. Huang, J. Mater. Sci. Technol. 33 (2017) 1475-1486.

[23] S.-J. Kim, C. Gil Lee, T.-H. Lee, C.-S. Oh, Scr. Mater. 48 (2003) 539-544.

[24] I.B. Timokhina, P.D. Hodgson, E.V. Pereloma, Metall. Mater. Trans. A 35 (2004) 2331-2341.

[25] H.W. Luo, H. Dong, Mater. Sci. Eng. A 626 (2015) 207-212.

[26] G. Ghosh, G.B. Olson, Metall. Mater. Trans. A 32 (2001) 455-467.

[27] S. Zaefferer, J. Ohlert, W. Bleck, Acta Mater. 52 (2004) 2765-2778.

[28] H.J. Jun, S.H. Park, S.D. Choi, C.G. Park, Mater. Sci. Eng. A 379 (2004) 204-209.
[29] J. Huang, W.J. Poole, M. Militzer, Metall. Mater. Trans. A 35 (2004) 3363-3375.
[30] P. Jacques, E. Girault, T. Catlin, N. Geerlofs, T. Kop, S. van der Zwaag, F. Delannay, Mater. Sci. Eng. A 273-275 (1999) 475-479.
[31] E. Jimenez-Melero, N.H. van Dijk, L. Zhao, J. Sietsma, S.E. Offerman, J.P. Wright, S. van der Zwaag, Acta Mater. 55 (2007) 6713-6723.
[32] S.v.d. Zwaag, L. Zhao, S.O. Kruijver, J. Sietsma, ISIJ Int. 42 (2002) 1565-1570.
[33] R. Blonde, E. Jimenez-Melero, L. Zhao, J.P. Wright, E. Bruck, S. van der Zwaag, N.H. van Dijk, Acta Mater. 60 (2012) 565-577.
[34] R. Blonde, E. Jimenez-Melero, L. Zhao, N. Schell, E. Bruck, S. van der Zwaag, N.H. van Dijk, Mater. Sci. Eng. A 594 (2014) 125-134.
[35] R. Blonde, E. Jimenez-Melero, L. Zhao, J.P. Wright, E. Bruck, S. van der Zwaag, N.H. van Dijk, Mater. Sci. Eng. A 618 (2014) 280-287.
[36] S. Turteltaub, A.S.J. Suiker, J. Mech. Phys. Solids 53 (2005) 1747-1788.
[37] D.D. Tjahjanto, A.S.J. Suiker, S. Turteltaub, P.E.J.R.D. del Castillo, S. van der Zwaag, Comp. Mater. Sci. 41 (2007) 107-116.
[38] C. Zener, J. Appl. Phys. 20 (1949) 950-953.
[39] M. Hillert, Scr. Mater. 46 (2002) 447-453.
[40] M. Hillert, J. Ågren, Scr. Mater. 50 (2004) 697-699.
[41] D.E. Coates, Metall. Trans. 3 (1972) 1203-1212.
[42] D.E. Coates, Metall. Trans. 4 (1973) 1077-1086.
[43] M. Goune, F. Danoix, J. Agren, Y. Brechet, C.R. Hutchinson, M. Militzer, G. Purdy, S. van der Zwaag, H. Zurob, Mater. Sci. Eng. R 92 (2015) 1-38.
[44] Z.B. Dai, R. Ding, Z.G. Yang, C. Zhang, H. Chen, Acta Mater. 152 (2018) 288-299.
[45] C. Bos, J. Sietsma, Scr. Mater. 57 (2007) 1085-1088.
[46] J. Sietsma, S. van der Zwaag, Acta Mater. 52 (2004) 4143-4152.
[47] H. Chen, S. van der Zwaag, J. Mater. Sci. 46 (2011) 1328-1336.
[48] J. Zhu, H. Luo, Z. Yang, C. Zhang, S.v.d. Zwaag, H. Chen, Acta Mater. 133 (2017) 258-268.
[49] H. Chen, S. van der Zwaag, Acta Mater. 72 (2014) 1-12.
[50] Y. van Leeuwen, S. Vooijs, J. Sietsma, S. Van Der Zwaag, Metall. Mater. Trans. A 29 (1998) 2925-2931.
[51] M. Militzer, M.G. Mecozzi, J. Sietsma, S. van der Zwaag, Acta Mater. 54 (2006) 3961-3972.
[52] H. Fang, M.G. Mecozzi, E. Brück, S. van der Zwaag, N.H. van Dijk, Metall. Mater. Trans. A 49 (2017) 41-53.
[53] M. Toloui, M. Militzer, Acta Mater. 144 (2018) 786-800.
[54] G.R. Speich, V.A. Demarest, R.L. Miller, Metall. Mater. Trans. A 12 (1981) 1419-1428.
[55] C. Atkinson, T. Akbay, R.C. Reed, Acta Metall. Mater. 43 (1995) 2013-2031.

[56] H. Chen, X. Xu, W. Xu, S. van der Zwaag, Metall. Mater. Trans. A 45 (2014) 1675-1679.
[57] H. Farahani, W. Xu, S. Van der Zwaag, Metall. Mater. Trans. A 46 (2015) 4978-4985.
[58] M.G. Mecozzi, C. Bos, J. Sietsma, Acta Mater. 88 (2015) 302-313.
[59] M. Ollat, M. Militzer, V. Massardier, D. Fabregue, E. Buscarlet, F. Keovilay, M. Perez, Comp. Mater. Sci. 149 (2018) 282-290.
[60] D. An, S. Pan, Q. Ren, Q. Li, B.W. Krakauer, M. Zhu, Scr. Mater. 178 (2020) 207-210.
[61] E. Gamsjager, H. Chen, S. van der Zwaag, Comp. Mater. Sci. 83 (2014) 92-100.
[62] A.M. Ravi, A. Kumar, M. Herbig, J. Sietsma, M.J. Santofimia, Acta Mater. 188 (2020) 424-434.
[63] H. Kawata, K. Hayashi, N. Sugiura, N. Yoshinaga, M. Takahashi, Mater. Sci. Forum 638-642 (2010) 3307-3312.
[64] D. Quidort, Y.J.M. Brechet, Acta Mater. 49 (2001) 4161-4170.
[65] K.Y. Zhu, H. Chen, J.P. Masse, O. Bouaziz, G. Gachet, Acta Mater. 61 (2013) 6025-6036.
[66] E. Girault, P. Jacques, P. Ratchev, J. Van Humbeeck, B. Verlinden, E. Aernoudt, Mater. Sci. Eng. A 273-275 (1999) 471-474.
[67] J.B. Li, J. Zhang, Q.H. Li, D. Guo, Y.D. Liu, Q.G. Meng, J. Mater. Sci. 53 (2018) 15667-15678.
[68] E. Jimenez-Melero, N.H. van Dijk, L. Zhao, J. Sietsma, S.E. Offerman, J.P. Wright, S. van der Zwaag, Acta Mater. 57 (2009) 533-543.
[69] K. Hasegawa, K. Kawamura, T. Urabe, Y. Hosoya, ISIJ Int. 44 (2004) 603-609.
[70] K.-i. Sugimoto, T. Iida, J. Sakaguchi, T. Kashima, ISIJ Int. 40 (2000) 902-908.
[71] F.G. Caballero, C. Garcia-Mateo, J. Chao, M.J. Santofimia, C. Capdevila, C.G. de Andres, ISIJ Int. 48 (2008) 1256-1262.
[72] K. Sugimoto, M. Tsunezawa, T. Hojo, S. Ikeda, ISIJ Int. 44 (2004) 1608-1614.
[73] J.-B. Seol, D. Raabe, P.-P. Choi, Y.-R. Im, C.-G. Park, Acta Mater. 60 (2012) 6183-6199.
[74] F.G. Caballero, S. Allain, J. Cornide, J.D.P. Velasquez, C. Garcia-Mateo, M.K. Miller, Mater. Des. 49 (2013) 667-680.
[75] F.G. Caballero, H.K.D.H. Bhadeshia, K.J.A. Mawella, D.G. Jones, P. Brown, Mater. Sci. Technol. 18 (2013) 279-284.
[76] X.Y. Long, F.C. Zhang, Z.N. Yang, B. Lv, Mater. Sci. Eng. A 715 (2018) 10-16.
[77] K. Sugimoto, A. Kanda, R. Kikuchi, S. Hashimoto, T. Kashima, S. Ikeda, ISIJ Int. 42 (2002) 910-915.
[78] K. Sugimoto, K. Nakano, S.M. Song, T. Kashima, ISIJ Int. 42 (2002) 450-455.
[79] L.H. Qian, Q. Zhou, F.C. Zhang, J.Y. Meng, M. Zhang, Y. Tian, Mater. Des. 39 (2012) 264-268.
[80] F.G. Caballero, S. Allain, J.D. Puerta-Velasquez, C. Garcia-Mate, ISIJ Int. 53 (2013) 1253-1259.
[81] F.G. Caballero, M.J. Santofimia, C. Capdevila, C. García-Mateo, C. García de Andrés, ISIJ Int. 46 (2006) 1479-1488.
[82] F.G. Caballero, M.J. Santofimia, C. Garcia-Mateo, J. Chao, C.G. de Andres, Mater. Des. 30 (2009) 2077-2083.

[83] X. Zhang, G. Xu, X. Wang, D. Embury, O. Bouaziz, G.R. Purdy, H.S. Zurob, Metall. Mater. Trans. A 45 (2013) 1352-1361.
[84] C. Hofer, F. Winkelhofer, H. Clemens, S. Primig, Mater. Sci. Eng. A 664 (2016) 236-246.
[85] H.K.D.H. Bhadeshia, D.V. Edmonds, Acta Metall. 28 (1980) 1265-1273.
[86] K. Hase, C. Garcia-Mateo, H.K.D.H. Bhadeshia, Mater. Sci. Eng. A 438 (2006) 145-148.
[87] X.Y. Long, J. Kang, B. Lv, F.C. Zhang, Mater. Des. 64 (2014) 237-245.
[88] X.L. Wang, K.M. Wu, F. Hu, L. Yu, X.L. Wan, Scr. Mater. 74 (2014) 56-59.
[89] Y.H. Wang, F.C. Zhang, T.S. Wang, Scr. Mater. 68 (2013) 763-766.
[90] S. Chen, R. Rana, C. Lahaije, Metall. Mater. Trans. A 45 (2014) 2209-2218.
[91] S. Das, A. Haldar, Metall. Mater. Trans. A 45 (2014) 1844-1854.
[92] M. Shah, S.K. Das, S.G. Chowdhury, Metall. Mater. Trans. A (2019).
[93] G. Gao, H. Zhang, X. Gui, Z. Tan, B. Bai, Y. Weng, Acta Mater. 101 (2015) 31-39.
[94] G. Gao, H. Zhang, X. Gui, P. Luo, Z. Tan, B. Bai, Acta Mater. 76 (2014) 425-433.
[95] S. Sharma, S. Sangal, K. Mondal, Metall. Mater. Trans. A 42 (2011) 3921-3933.
[96] W. Gong, Y. Tomota, S. Harjo, Y.H. Su, K. Aizawa, Acta Mater. 85 (2015) 243-249.
[97] M. Hillert, Scr. Mater. 47 (2002) 137–138.
[98] Z.G. Yang, H.S. Fang, Curr. Opin. Solid State Mater. Sci. 9 (2005) 277-286.
[99] H.I. Aaronson, W.T. Reynolds, G.R. Purdy, Metall. Mater. Trans. A 37a (2006) 1731-1745.
[100] L.C.D. Fielding, Mater. Sci. Technol. 29 (2013) 383-399.
[101] A. Borgenstam, M. Hillert, J. Agren, Acta Mater. 57 (2009) 3242-3252.
[102] M. Hillert, ISIJ Int. 35 (1995) 1134-1140.
[103] H.K.D.H. Bhadeshia, Bainite in steels: theory and practice, Maney Publishing, 2015.
[104] G.I. Rees, H.K.D.H. Bhadeshia, Mater. Sci. Technol. 8 (2013) 985-993.
[105] F.G. Caballero, M.K. Miller, S.S. Babu, C. Garcia-Mateo, Acta Mater. 55 (2007) 381-390.
[106] F.G. Caballero, M.K. Miller, C. Garcia-Mateo, Acta Mater. 58 (2010) 2338-2343.
[107] R. Rementeria, J.A. Jimenez, S.Y.P. Allain, G. Geandier, J.D. Poplawsky, W. Guo, E. Urones-Garrote, C. Garcia-Mateo, F.G. Caballero, Acta Mater. 133 (2017) 333-345.
[108] N. Takayama, G. Miyamoto, T. Furuhara, Acta Mater. 145 (2018) 154-164.
[109] T. Furuhara, K. Tsuzumi, G. Miyamoto, T. Amino, G. Shigesato, Metall. Mater. Trans. A 45a (2014) 5990-5996.
[110] Z.Q. Liu, G. Miyamoto, Z.G. Yang, C. Zhang, T. Furuhara, Metall. Mater. Trans. A 46a (2015) 1544-1549.
[111] Y. Xia, G. Miyamoto, Z.G. Yang, C. Zhang, T. Furuhara, Acta Mater. 91 (2015) 10-18.
[112] T. Furuhara, T. Yamaguchi, G. Miyamoto, T. Maki, Mater. Sci. Technol. 26 (2013) 392-397.
[113] M. Hillert, Metall. Mater. Trans. A 25A (1994) 1957-1966.
[114] M. Hillert, L. Hoglund, J. Ågren, Metall. Mater. Trans. A 35A (2004) 3693-3700.
[115] M. Hillert, A. Borgenstam, J. Å gren, Scr. Mater. 62 (2010) 75-77.

[116] L. Leach, P. Kolmskog, L. Höglund, M. Hillert, A. Borgenstam, Metall. Mater. Trans. A 50 (2019) 4531-4540.
[117] L. Leach, P. Kolmskog, L. Hoglund, M. Hillert, A. Borgenstam, Metall. Mater. Trans. A 49a (2018) 4509-4520.
[118] S.M.C. van Bohemen, Mater. Sci. Technol. 28 (2012) 487-495.
[119] S.M.C. Van Bohemen, Metall. Mater. Trans. A 41a (2010) 285-296.
[120] H.D. Wu, G. Miyamoto, Z.G. Yang, C. Zhang, H. Chen, T. Furuhara, Acta Mater. 133 (2017) 1-9.
[121] H.I. Aaronson, W.T. Reynolds, G.R. Purdy, Metall. Mater. Trans. A 35a (2004) 1187-1210.
[122] H.I. Aaronson, G. Spanos, W.T. Reynolds, Scr. Mater. 47 (2002) 139-144.
[123] W.T. Reynolds, F.Z. Li, C.K. Shui, H.I. Aaronson, Metall. Trans. A 21 (1990) 1433-1463.
[124] H. Goldenstein, H.I. Aaronson, Metall. Trans. A 21 (1990) 1465-1478.
[125] H. Chen, A. Borgenstam, J. Odqvist, I. Zuazo, M. Goune, J. Agren, S. van der Zwaag, Acta Mater. 61 (2013) 4512-4523.
[126] H. Chen, Z. Yang, C. Zhang, K. Zhu, S. van der Zwaag, Acta Mater. 104 (2016) 62-71.
[127] H. Chen, K. Zhu, L. Zhao, S. van der Zwaag, Acta Mater. 61 (2013) 5458-5468.
[128] H. Chen, S. van der Zwaag, Jom 68 (2016) 1320-1328.
[129] H. Chen, S. van der Zwaag, Metall. Mater. Trans. A 45a (2014) 3429-3437.
[130] G.R. Purdy, Y.J.M. Brechet, Acta Metall. Mater. 43 (1995) 3763-3774.
[131] Z.P. Xiong, A.A. Saleh, R.K.W. Marceau, A.S. Taylor, N.E. Stanford, A.G. Kostryzhev, E.V. Pereloma, Acta Mater. 134 (2017) 1-15.
[132] W.W. Sun, H.S. Zurob, C.R. Hutchinson, Acta Mater. 139 (2017) 62-74.
[133] L. Leach, L. Höglund, A. Borgenstam, J. Ågren, Transformation barriers for growth of WS-ferrite and bainitic ferrite, 2017.
[134] T. Hojo, K.I. Sugimoto, Y. Mukai, S. Ikeda, ISIJ Int. 48 (2008) 824-829.
[135] R.W. Zhao, T.Q. Liu, X.Q. Zhao, Mater. Sci. Forum 749 (2013) 287-293.
[136] P. Zhou, H. Guo, A.M. Zhao, Z.K. Yin, J.X. Wang, Mater. Sci. Forum 898 (2017) 803-809.
[137] J. Mola, B.C. De Cooman, Scr. Mater. 65 (2011) 834-837.
[138] M. Wendler, C. Ullrich, M. Hauser, L. Krüger, O. Volkova, A. Weiß, J. Mola, Acta Mater. 133 (2017) 346-355.
[139] J. Mola, B.C. De Cooman, Metall. Mater. Trans. A 44 (2012) 946-967.
[140] S. Yan, X. Liu, W.J. Liu, H. Lan, H. Wu, Mater. Sci. Eng. A 620 (2015) 58-66.
[141] X. Zhu, W. Li, H.G. Zhao, L. Wang, X.J. Jin, Int. J. Hydrogen Energy 39 (2014) 13031-13040.
[142] L. Barbe, K. Verbeken, E. Wettinck, ISIJ Int. 46 (2006) 1251-1257.
[143] D.T. Pierce, D.R. Coughlin, K.D. Clarke, E. De Moor, J. Poplawsky, D.L. Williamson, B. Mazumder, J.G. Speer, A. Hood, A.J. Clarke, Acta Mater. 151 (2018) 454-469.
[144] E.J. Seo, L. Cho, B.C. De Cooman, Acta Mater. 107 (2016) 354-365.

[145] E.J. Seo, L. Cho, Y. Estrin, B.C. De Cooman, Acta Mater. 113 (2016) 124-139.
[146] S.Y.P. Allain, G. Geandier, J.C. Hell, M. Soler, F. Danoix, M. Goune, Scr. Mater. 131 (2017) 15-18.
[147] A.K. Behera, G.B. Olson, Scr. Mater. 147 (2018) 6-10.
[148] T.Y. Hsu, Z.Y. Xu, Mater. Sci. Forum 561-565 (2007) 2283-2286.
[149] X. Jin, Quenching and Partitioning Heat Treatment: High-Strength, Low-Alloy, in: G.E. Totten, R. Colas (Eds.), Encyclopedia of Iron, Steel, and Their Alloys, CRC Press, 2016, pp. 2761-2775.
[150] E. De Moor, J.G. Speer, Bainitic and quenching and partitioning steels, in: R. Rana, S.B. Singh (Eds.), Automotive Steels, Woodhead Publishing, 2017, pp. 289-316.
[151] F. HajyAkbary, J. Sietsma, G. Miyamoto, T. Furuhara, M.J. Santofimia, Acta Mater. 104 (2016) 72-83.
[152] J.S. Farideh HajyAkbary, Roumen H. Petrov, Goro Miyamoto, Tadashi Furuhara, Maria Jesus Santofimia, Scr. Mater. 137 (2017) 27-30.
[153] R. Ding, D. Tang, A.M. Zhao, R. Dong, J.Y. Cheng, X.Y. Zhang, Mater. Manuf. Process. 29 (2014) 704-709.
[154] R. Ding, D. Tang, A.M. Zhao, R. Dong, J.Y. Cheng, X. Meng, J. Mater. Res. 29 (2014) 2525-2533.
[155] D. De Knijf, A. Puype, C. Föjer, R. Petrov, Mater. Sci. Eng. A 627 (2015) 182-190.
[156] G. Liu, S.G. Zhang, J. Li, J. Wang, Q.G. Meng, Mater. Sci. Eng. A 669 (2016) 387-395.
[157] S. Yan, X. Liu, W.J. Liu, T. Liang, B. Zhang, L. Liu, Y. Zhao, Mater. Sci. Eng. A 684 (2017) 261-269.
[158] C.H. Song, H. Yu, L.L. Li, T. Zhou, J. Lu, X.H. Liu, Mater. Sci. Eng. A 670 (2016) 326-334.
[159] J. Sun, H. Yu, Mater. Sci. Eng. A 586 (2013) 100-107.
[160] J. Sun, H. Yu, S. Wang, Y. Fan, Mater. Sci. Eng. A 596 (2014) 89-97.
[161] L. Cho, E.J. Seo, B.C. De Cooman, Scr. Mater. 123 (2016) 69-72.
[162] C. Celada-Casero, C. Kwakernaak, J. Sietsma, M.J. Santofimia, Mater. Des. 178 (2019).
[163] E.A. Ariza, A.S. Nishikawa, H. Goldenstein, A.P. Tschiptschin, Mater. Sci. Eng. A 671 (2016) 54-69.
[164] E.A. Ariza, J. Poplawsky, W. Guo, K. Unocic, A.J. Ramirez, A.P. Tschiptschin, S.S. Babu, Metall. Mater. Trans. A 49 (2018) 4809-4823.
[165] F. Wang, Y. Zhu, H. Zhou, B. Jiang, G. Wang, Sci. China Technol. Sci. 56 (2013) 1847-1857.
[166] N. Zhong, X.D. Wang, L. Wang, Y.H. Rong, Mater. Sci. Eng. A 506 (2009) 111-116.
[167] H.L. Yi, P. Chen, Z.Y. Hou, N. Hong, H.L. Cai, Y.B. Xu, D. Wu, G.D. Wang, Scr. Mater. 68 (2013) 370-374.
[168] Z.R. Hou, T. Opitz, X.C. Xiong, X.M. Zhao, H.L. Yi, Scr. Mater. 162 (2019) 492-496.
[169] H.L. Cai, P. Chen, J.K. Oh, Y.R. Cho, D. Wu, H.L. Yi, Scr. Mater. 178 (2020) 77-81.
[170] T.Y. Hsu, L. Xuemin, Scr. Metall. 17 (1983) 1285-1288.

[171] J. Epp, T. Hirsch, C. Curfs, Metall. Mater. Trans. A 43 (2012) 2210-2217.
[172] P. Liu, B. Zhu, Y. Wang, Y. Zhang, Metall. Mater. Trans. A 47 (2016) 4325-4333.
[173] E.D. Moor, J.G. Speer, D.K. Matlock, J.-H. Kwak, S.-B. Lee, ISIJ Int. 51 (2011) 137-144.
[174] M.J. Santofimia, L. Zhao, R. Petrov, C. Kwakernaak, W.G. Sloof, J. Sietsma, Acta Mater. 59 (2011) 6059-6068.
[175] P. Huyghe, L. Malet, M. Caruso, C. Georges, S. Godet, Mater. Sci. Eng. A 701 (2017) 254-263.
[176] D. De Knijf, E.P. Da Silva, C. Föjer, R. Petrov, Mater. Sci. Technol. 31 (2015) 817-828.
[177] A. Arlazarov, M. Ollat, J.P. Masse, M. Bouzat, Mater. Sci. Eng. A 661 (2016) 79-86.
[178] J.C. Fisher, Trans. AIME. 185 (1949) 688-690.
[179] T.Y. Hsu, H.B. Chang, Acta Metall. 32 (1984) 343-348.
[180] T.Y. Hsu, J. Mater. Sci. 20 (1985) 23-31.
[181] G. Ghosh, G.B. Olson, Acta Metall. Mater. 42 (1994) 3361-3370.
[182] G. Ghosh, G.B. Olson, Acta Mater. 50 (2002) 2655-2675.
[183] G. Ghosh, G.B. Olson, J. Phase Equilibria 22 (2001) 199-207.
[184] A. Stormvinter, A. Borgenstam, J. Ågren, Metall. Mater. Trans. A 43 (2012) 3870-3879.
[185] E.I. Galindo-Nava, Scr. Mater. 138 (2017) 6-11.
[186] J. Wang, S. Van Der Zwaag, Metall. Mater. Trans. A 32 (2001) 1527-1539.
[187] A. García-Junceda, C. Capdevila, F.G. Caballero, C.G. de Andrés, Scr. Mater. 58 (2008) 134-137.
[188] E. Jimenez-Melero, N.H. van Dijk, L. Zhao, J. Sietsma, S.E. Offerman, J.P. Wright, S. van der Zwaag, Scr. Mater. 56 (2007) 421-424.
[189] S.M.C. van Bohemen, L. Morsdorf, Acta Mater. 125 (2017) 401-415.
[190] P.J. Brofman, G.S. Ansell, Metall. Trans. A 14 (1983) 1929-1931.
[191] J.C. Fisher, J.H. Hollomon, D. Turnbull, Jom 1 (2017) 691-700.
[192] H. Yang, H. Bhadeshia, Scr. Mater. 60 (2009) 493-495.
[193] S.-J. Lee, K.-S. Park, Metall. Mater. Trans. A 44 (2013) 3423-3427.
[194] W. Steven, A.G. Haynes, J. Iron Steel Res. Int. 183 (1956) 349-359.
[195] K.W. Andrews, J. Iron Steel Res. Int. 203 (1965) 721-727.
[196] D. Barbier, Adv. Eng. Mater. 16 (2014) 122-127.
[197] C. Garcia-Mateo, C. Capdevila, F.G. Caballero, C. de Andres, J. Mater. Sci. 42 (2007) 5391-5397.
[198] W.G. Vermeulen, P.F. Morris, A.P. deWeijer, S. vanderZwaag, Ironmak. Steelmak. 23 (1996) 433-437.
[199] M. Rahaman, W. Mu, J. Odqvist, P. Hedström, Metall. Mater. Trans. A 50 (2019) 2081-2091.
[200] E. Belisle, Z. Huang, S. Le Digabel, A.E. Gheribi, Comp. Mater. Sci. 98 (2015) 170-177.
[201] D.P. Koistinen, R.E. Marburger, Acta Metall. 7 (1959) 59-60.
[202] C.L. Magee, Phase Transformations (1970) 115-156.
[203] J.G. Speer, D.V. Edmonds, F.C. Rizzo, D.K. Matlock, Curr. Opin. Solid State Mater. Sci. 8 (2004) 219-237.

[204] S.M.C. van Bohemen, J. Sietsma, Mater. Sci. Technol. 25 (2009) 1009-1012.
[205] S.-J. Lee, C.J. Van Tyne, Metall. Mater. Trans. A 43 (2011) 422-427.
[206] C. Capdevila, F.G. Caballero, C.G. De Andres, ISIJ Int. 42 (2002) 894-902.
[207] S. Kim, J. Lee, F. Barlat, M.-G. Lee, Acta Mater. 109 (2016) 394-404.
[208] S.J. Lee, S. Lee, B.C. De Cooman, International J. Mater. Res. 104 (2013) 423-429.
[209] F. Huyan, P. Hedström, L. Höglund, A. Borgenstam, Metall. Mater. Trans. A 47 (2016) 4404-4410.
[210] N. Nakada, Y. Ishibashi, T. Tsuchiyama, S. Takaki, Acta Mater. 110 (2016) 95-102.
[211] J.G. Speer, D.K. Matlock, B.C. DeCooman, J.G. Schroth, Scr. Mater. 52 (2005) 83-85.
[212] M. Hillert, J. Ågren, Scr. Mater. 52 (2005) 87-88.
[213] A.J. Clarke, J.G. Speer, D.K. Matlock, F.C. Rizzo, D.V. Edmonds, M.J. Santofimia, Scr. Mater. 61 (2009) 149-152.
[214] E.J. Seo, L. Cho, B.C. De Cooman, Metall. Mater. Trans. A 46 (2015) 27-31.
[215] K. Kim, S.-J. Lee, Mater. Sci. Eng. A 698 (2017) 183-190.
[216] M. Hillert, L. Hoglund, J. Agren, Acta Metall. Mater. 41 (1993) 1951-1957.
[217] M.G. Mecozzi, J. Eiken, M.J. Santofimia, J. Sietsma, Comp. Mater. Sci. 112 (2016) 245-256.
[218] G.A. Thomas, J.G. Speer, Mater. Sci. Technol. 30 (2014) 998-1007.
[219] G.A. Thomas, F. Danoix, J.G. Speer, S.W. Thompson, F. Cuvilly, ISIJ Int. 54 (2014) 2900-2906.
[220] N. Zhong, X. Wang, Y. Rong, L. Wang, J. Mater. Sci. Technol. 22 (2006) 751-754.
[221] H.Y. Li, X.W. Lu, W.J. Li, X.J. Jin, Metall. Mater. Trans. A 41 (2010) 1284-1300.
[222] D. Kim, S.-J. Lee, B.C. De Cooman, Metall. Mater. Trans. A 43 (2012) 4967-4983.
[223] X. Tan, Y. Xu, X. Yang, D. Wu, Mater. Sci. Eng. A 589 (2014) 101-111.
[224] D. Kim, J.G. Speer, B.C. De Cooman, Metall. Mater. Trans. A 42 (2010) 1575-1585.
[225] M.J. Santofimia, T. Nguyen-Minh, L. Zhao, R. Petrov, I. Sabirov, J. Sietsma, Mater. Sci. Eng. A 527 (2010) 6429-6439.
[226] M.J. Santofimia, L. Zhao, J. Sietsma, Mater. Sci. Forum 706-709 (2012) 2290-2295.
[227] S.Y.P. Allain, S. Gaudez, G. Geandier, J.-C. Hell, M. Gouné, F. Danoix, M. Soler, S. Aoued, A. Poulon-Quintin, Mater. Sci. Eng. A 710 (2018) 245-250.
[228] S.Y.P. Allain, G. Geandier, J.C. Hell, M. Soler, F. Danoix, M. Gouné, Metals 7 (2017).
[229] T.D. Bigg, D.V. Edmonds, E.S. Eardley, J. Alloys Compd. 577 (2013) S695-S698.
[230] D. De Knijf, M.J. Santofimia, H. Shi, V. Bliznuk, C. Föjer, R. Petrov, W. Xu, Acta Mater. 90 (2015) 161-168.
[231] J.G. Speer, R.E. Hackenberg, B.C. Decooman, D.K. Matlock, Philos. Mag. Lett. 87 (2007) 379-382.
[232] M.J. Santofimia, L. Zhao, J. Sietsma, Scr. Mater. 59 (2008) 159-162.
[233] M.J. Santofimia, J.G. Speer, A.J. Clarke, L. Zhao, J. Sietsma, Acta Mater. 57 (2009) 4548-4557.

[234] Y. Takahama, M.J. Santofimia, M.G. Mecozzi, L. Zhao, J. Sietsma, Acta Mater. 60 (2012) 2916-2926.
[235] M.J. Santofimia, L. Zhao, J. Sietsma, Metall. Mater. Trans. A 42 (2011) 3620-3626.
[236] K.S. Choi, Z. Zhu, X. Sun, E. De Moor, M.D. Taylor, J.G. Speer, D.K. Matlock, Scr. Mater. 104 (2015) 79-82.
[237] A.K. Behera, G.B. Olson, Jom 71 (2019) 1375-1385.
[238] Y. Toji, H. Matsuda, M. Herbig, P.P. Choi, D. Raabe, Acta Mater. 65 (2014) 215-228.
[239] A. Devaraj, Z.R. Xu, F. Abu-Farha, X. Sun, L.G. Hector, Jom 70 (2018) 1752-1757.
[240] M. Gouné, S. Aoued, F. Danoix, G. Geandier, A. Poulon-Quintin, J.C. Hell, M. Soler, S.Y.P. Allain, Scr. Mater. 162 (2019) 181-184.
[241] Z. Dai, X. Wang, J. He, Z. Yang, C. Zhang, H. Chen, Metall. Mater. Trans. A 48 (2017) 3168-3174.
[242] Z.B. Dai, R. Ding, Z.G. Yang, C. Zhang, H. Chen, Acta Mater. 144 (2018) 666-678.
[243] Y. Toji, H. Matsuda, D. Raabe, Acta Mater. 116 (2016) 250-262.
[244] B. An, C. Zhang, G. Gao, X. Gui, Z. Tan, R.D.K. Misra, Z. Yang, Mater. Sci. Eng. A 757 (2019) 117-123.
[245] M.J. Santofimia, S.M.C. van Bohemen, J. Sietsma, J. South. Afr. Inst. Min. Metall. 113 (2013) 147-152.
[246] H.R. Guo, G.H. Gao, X.L. Gui, R.D.K. Misra, B.Z. Bai, Mater. Sci. Eng. A 667 (2016) 224-231.
[247] H.Y. Li, X.W. Lu, X.C. Wu, Y.A. Min, X.J. Jin, Mater. Sci. Eng. A 527 (2010) 6255-6259.
[248] S. Samanta, S. Das, D. Chakrabarti, I. Samajdar, S.B. Singh, A. Haldar, Metall. Mater. Trans. A 44 (2013) 5653-5664.
[249] M.C. Somani, D.A. Porter, L.P. Karjalainen, R.D.K. Misra, Metall. Mater. Trans. A 45a (2014) 1247-1257.
[250] S. Chen, G.Z. Wang, C. Liu, C.C. Wang, X.M. Zhao, W. Xu, J. Iron Steel Res. Int. 24 (2017) 1095-1103.
[251] C. Song, H. Yu, J. Lu, T. Zhou, Steel Res. Int. (2018).
[252] A. Shibata, S. Morito, T. Furuhara, T. Maki, Scr. Mater. 53 (2005) 597-602.
[253] G. Miyamoto, A. Shibata, T. Maki, T. Furuhara, Acta Mater. 57 (2009) 1120-1131.
[254] A.M. Ravi, A. Navarro-López, J. Sietsma, M.J. Santofimia, Acta Mater. 188 (2020) 394-405.
[255] Y. Li, S. Chen, C. Wang, D.S. Martín, W. Xu, Acta Mater. 188 (2020) 528-538.
[256] A.S. Nishikawa, M.J. Santofimia, J. Sietsma, H. Goldenstein, Acta Mater. 142 (2018) 142-151.
[257] S.M.C. van Bohemen, D.N. Hanlon, Int. J. Mater. Res. 103 (2012) 987-991.
[258] S.M.C. Van Bohemen, J. Sietsma, Metall. Mater. Trans. A 40 (2009) 1059-1068.
[259] P. Huyghe, M. Caruso, J.-L. Collet, S. Dépinoy, S. Godet, Mater. Sci. Eng. A 743 (2019) 175-184.

[260] D.V. Edmonds, K. He, F.C. Rizzo, B.C. De Cooman, D.K. Matlock, J.G. Speer, Mater. Sci. Eng. A 438-440 (2006) 25-34.
[261] B. Kim, J. Sietsma, M.J. Santofimia, Mater. Des. 127 (2017) 336-345.
[262] E.D. Moor, S. Lacroix, L. Samek, J. Penning, J.G. Speer, Dilatometric Study of the Quench and Partitioning Process, The 3rd International Conference on Advanced Structural Steels, Gyeongju, Korea, 2006.
[263] M.J. Santofimia, R.H. Petrov, L. Zhao, J. Sietsma, Mater. Charact. 92 (2014) 91-95.
[264] M.J. Santofimia, L. Zhao, J. Sietsma, Metall. Mater. Trans. A 40 (2009) 46-57.
[265] J.H. Jang, I.G. Kim, H.K.D.H. Bhadeshia, Comp. Mater. Sci. 44 (2009) 1319-1326.
[266] X. Zhu, W. Li, T.Y. Hsu, S. Zhou, L. Wang, X. Jin, Scr. Mater. 97 (2015) 21-24.
[267] F. HajyAkbary, J. Sietsma, G. Miyamoto, N. Kamikawa, R.H. Petrov, T. Furuhara, M.J. Santofimia, Mater. Sci. Eng. A 677 (2016) 505-514.
[268] S.S. Nayak, R. Anumolu, R.D.K. Misra, K.H. Kim, D.L. Lee, Mater. Sci. Eng. A 498 (2008) 442-456.
[269] D.T. Pierce, D.R. Coughlin, D.L. Williamson, K.D. Clarke, A.J. Clarke, J.G. Speer, E. De Moor, Acta Mater. 90 (2015) 417-430.
[270] D.T. Pierce, D.R. Coughlin, D.L. Williamson, J. Kähkönen, A.J. Clarke, K.D. Clarke, J.G. Speer, E. De Moor, Scr. Mater. 121 (2016) 5-9.
[271] S.Y.P. Allain, S. Aoued, A. Quintin-Poulon, M. Goune, F. Danoix, J.C. Hell, M. Bouzat, M. Soler, G. Geandier, Materials (Basel) 11 (2018).
[272] Y. Toji, G. Miyamoto, D. Raabe, Acta Mater. 86 (2015) 137-147.
[273] G. Gao, B. Gao, X. Gui, J. Hu, J. He, Z. Tan, B. Bai, Mater. Sci. Eng. A 753 (2019) 1-10.
[274] J.H. Jang, I.G. Kim, H.K.D.H. Bhadeshia, Scr. Mater. 63 (2010) 121-123.
[275] A.T.W. Barrow, J.H. Kang, P.E.J. Rivera-Díaz-del-Castillo, Acta Mater. 60 (2012) 2805-2815.
[276] G. Miyamoto, J. Oh, K. Hono, T. Furuhara, T. Maki, Acta Mater. 55 (2007) 5027-5038.
[277] B. Kim, C. Celada, D. San Martin, T. Sourmail, P.E.J. Rivera-Diaz-del-Castillo, Acta Mater. 61 (2013) 6983-6992.
[278] S.S. Babu, K. Hono, T. Sakurai, Metall. Mater. Trans. A 25 (1994) 499-508.
[279] S.S. Babu, K. Hono, T. Sakurai, Appl. Surf. Sci. 67 (1993) 321-327.
[280] G. Ghosh, G.B. Olson, Acta Mater. 50 (2002) 2099-2119.
[281] E. Kozeschnik, H.K.D.H. Bhadeshia, Mater. Sci. Technol. 24 (2013) 343-347.
[282] M.J. Santofimia, L. Zhao, R. Petrov, J. Sietsma, Mater. Charact. 59 (2008) 1758-1764.
[283] K.Y. Zhu, H. Shi, H. Chen, C. Jung, J. Mater. Sci. 53 (2018) 6951-6967.
[284] A.S. Nishikawa, G. Miyamoto, T. Furuhara, A.P. Tschiptschin, H. Goldenstein, Acta Mater. 179 (2019) 1-16.
[285] J. Shi, X. Sun, M. Wang, W. Hui, H. Dong, W. Cao, Scr. Mater. 63 (2010) 815-818.

[286] H. Lee, M.C. Jo, S.S. Sohn, A. Zargaran, J.H. Ryu, N.J. Kim, S. Lee, Acta Mater. 147 (2018) 247-260.
[287] W.W. Sun, Y.X. Wu, S.C. Yang, C.R. Hutchinson, Scr. Mater. 146 (2018) 60-63.
[288] R. Ding, Y. Yao, B. Sun, G. Liu, J. He, T. Li, X. Wan, Z. Dai, D. Ponge, D. Raabe, C. Zhang, A. Godfrey, G. Miyamoto, T. Furuhara, Z. Yang, S. van der Zwaag, H. Chen, Sci Adv 6 (2020) eaay1430.
[289] B.B. He, B. Hu, H.W. Yen, G.J. Cheng, Z.K. Wang, H.W. Luo, M.X. Huang, Science 357 (2017) 1029-1032.
[290] J. Han, A.K. da Silva, D. Ponge, D. Raabe, S.M. Lee, Y.K. Lee, S.I. Lee, B. Hwang, Acta Mater. 122 (2017) 199-206.
[291] B.H. Sun, F. Fazeli, C. Scott, N. Brodusch, R. Gauvin, S. Yue, Acta Mater. 148 (2018) 249-262.
[292] B. Sun, N. Vanderesse, F. Fazeli, C. Scott, J. Chen, P. Bocher, M. Jahazi, S. Yue, Scr. Mater. 133 (2017) 9-13.
[293] B. Sun, F. Fazeli, C. Scott, X. Yan, Z. Liu, X. Qin, S. Yue, Scr. Mater. 130 (2017) 49-53.
[294] Y.K. Lee, J. Han, Mater. Sci. Technol. 31 (2014) 843-856.
[295] B. Hu, H.W. Luo, F. Yang, H. Dong, J. Mater. Sci. Technol. 33 (2017) 1457-1464.
[296] Y. Ma, Mater. Sci. Technol. 33 (2017) 1713-1727.
[297] M. Cai, Z. Li, Q. Chao, P.D. Hodgson, Metall. Mater. Trans. A 45 (2014) 5624-5634.
[298] B.B. He, B. Hu, H.W. Yen, G.J. Cheng, Z.K. Wang, H.W. Luo, M.X. Huang, Science (2017).
[299] Z.J. Xie, C.J. Shang, S.V. Subramanian, X.P. Ma, R.D.K. Misra, Scr. Mater. 137 (2017) 36-40.
[300] H.W. Yen, S.W. Ooi, M. Eizadjou, A. Breen, C.Y. Huang, H.K.D.H. Bhadeshia, S.P. Ringer, Acta Mater. 82 (2015) 100-114.
[301] D. Lee, J.K. Kim, S. Lee, K. Lee, B.C. De Cooman, Mater. Sci. Eng. A 706 (2017) 1-14.
[302] H. Pan, H. Ding, M. Cai, Mater. Sci. Eng. A 736 (2018) 375-382.
[303] Y. Li, W. Li, W. Liu, X. Wang, X. Hua, H. Liu, X. Jin, Acta Mater. 146 (2018) 126-141.
[304] Y. Li, W. Li, N. Min, W.Q. Liu, X.J. Jin, Acta Mater. 139 (2017) 96-108.
[305] M.M. Wang, C.C. Tasan, D. Ponge, A.C. Dippel, D. Raabe, Acta Mater. 85 (2015) 216-228.
[306] M.M. Wang, C.C. Tasan, D. Ponge, A. Kostka, D. Raabe, Acta Mater. 79 (2014) 268-281.
[307] M.M. Wang, C.C. Tasan, D. Ponge, D. Raabe, Acta Mater. 111 (2016) 262-272.
[308] B.B. He, M.X. Huang, Metall. Mater. Trans. A (2018).
[309] H. Luo, J. Liu, H. Dong, Metall. Mater. Trans. A 47 (2016) 3119-3124.
[310] R.L. Miller, Metall. Mater. Trans. B 3 (1972) 905-912.
[311] J. Han, S.-J. Lee, J.-G. Jung, Y.-K. Lee, Acta Mater. 78 (2014) 369-377.
[312] X.G. Zhang, G. Miyamoto, Y. Toji, S. Nambu, T. Koseki, T. Furuhara, Acta Mater. 144 (2018) 601-612.
[313] X. Zhang, G. Miyamoto, T. Kaneshita, Y. Yoshida, Y. Toji, T. Furuhara, Acta Mater. 154 (2018) 1-13.
[314] S. Yan, X. Liu, T. Liang, Y. Zhao, Mater. Sci. Eng. A 712 (2018) 332-340.

[315] H.J. Pan, H. Ding, M.H. Cai, Mater. Sci. Eng. A 736 (2018) 375-382.
[316] S. Lee, S.-J. Lee, B.C. De Cooman, Scr. Mater. 65 (2011) 225-228.
[317] S.-J. Lee, S. Lee, B.C. De Cooman, Scr. Mater. 64 (2011) 649-652.
[318] J. Han, S.H. Kang, S.J. Lee, Y.K. Lee, J. Alloys Compd. 681 (2016) 580-588.
[319] A. Arlazarov, M. Goune, O. Bouaziz, A. Hazotte, G. Petitgand, P. Barges, Mater. Sci. Eng. A 542 (2012) 31-39.
[320] Y.-b. Xu, Z.-p. Hu, Y. Zou, X.-d. Tan, D.-t. Han, S.-q. Chen, D.-g. Ma, R.D.K. Misra, Mater. Sci. Eng. A 688 (2017) 40-55.
[321] W.H. Zhou, X.L. Wang, P.K.C. Venkatsurya, H. Guo, C.J. Shang, R.D.K. Misra, Mater. Sci. Eng. A 607 (2014) 569-577.
[322] W. Zhou, H. Guo, Z. Xie, X. Wang, C. Shang, Mater. Sci. Eng. A 587 (2013) 365-371.
[323] Z.J. Xie, G. Han, W.H. Zhou, X.L. Wang, C.J. Shang, R.D.K. Misra, Scr. Mater. 155 (2018) 164-168.
[324] Y. Zou, Y.B. Xu, Z.P. Hu, X.L. Gu, F. Peng, X.D. Tan, S.Q. Chen, D.T. Han, R.D.K. Misra, G.D. Wang, Mater. Sci. Eng. A 675 (2016) 153-163.
[325] J. Zhu, R. Ding, J. He, Z. Yang, C. Zhang, H. Chen, Scr. Mater. 136 (2017) 6-10.
[326] X. Wan, G. Liu, R. Ding, N. Nakada, Y.-W. Chai, Z. Yang, C. Zhang, H. Chen, Scr. Mater. 166 (2019) 68-72.
[327] T. Tsuchiyama, T. Inoue, J. Tobata, D. Akama, S. Takaki, Scr. Mater. 122 (2016) 36-39.
[328] R. Ding, Z.B. Dai, M.X. Huang, Z.G. Yang, C. Zhang, H. Chen, Acta Mater. 147 (2018) 59-69.
[329] B.C. De Cooman, S.J. Lee, S. Shin, E.J. Seo, J.G. Speer, Metall. Mater. Trans. A (2016).
[330] Y.-G. Yang, Z.-L. Mi, M. Xu, Q. Xiu, J. Li, H.-T. Jiang, Mater. Sci. Eng. A 725 (2018) 389-397.
[331] B. Hu, H. Luo, Acta Mater. 176 (2019) 250-263.
[332] J. Ma, Q. Lu, L. Sun, Y. Shen, Metall. Mater. Trans. A 49 (2018) 4404-4408.
[333] E. De Moor, D.K. Matlock, J.G. Speer, M.J. Merwin, Scr. Mater. 64 (2011) 185-188.
[334] S. Kang, E. De Moor, J.G. Speer, Metall. Mater. Trans. A 46 (2014) 1005-1011.
[335] C. Zhao, C. Zhang, W. Cao, Z. Yang, H. Dong, Y. Weng, ISIJ Int. 54 (2014) 2875-2880.
[336] C. Zhao, W.Q. Cao, C. Zhang, Z.G. Yang, H. Dong, Y.Q. Weng, Mater. Sci. Technol. 30 (2013) 791-799.
[337] S. Kang, R.W. Hofer, J.G. Speer, D. Krizan, D.K. Matlock, E. De Moor, Steel Res. Int. (2018).
[338] R. Rana, P.J. Gibbs, E. De Moor, J.G. Speer, D.K. Matlock, Steel Res. Int. 86 (2015) 1139-1150.
[339] S. Kang, J.G. Speer, D. Krizan, D.K. Matlock, E. De Moor, Mater. Des. 97 (2016) 138-146.
[340] S. Lee, B.C. De Cooman, Metall. Mater. Trans. A 45 (2013) 709-716.
[341] Z.C. Li, H. Ding, R.D.K. Misra, Z.H. Cai, H.X. Li, Mater. Sci. Eng. A 672 (2016) 161-169.
[342] G.K. Bansal, D.A. Madhukar, A.K. Chandan, K. Ashok, G.K. Mandal, V.C. Srivastava, Mater. Sci. Eng. A 733 (2018) 246-256.
[343] H.W. Luo, J. Shi, C. Wang, W.Q. Cao, X.J. Sun, H. Dong, Acta Mater. 59 (2011) 4002-4014.

[344] R. Wei, M. Enomoto, R. Hadian, H.S. Zurob, G.R. Purdy, Acta Mater. 61 (2013) 697-707.
[345] H. Kamoutsi, E. Gioti, G.N. Haidemenopoulos, Z. Cai, H. Ding, Metall. Mater. Trans. A 46 (2015) 4841-4846.
[346] N. Nakada, K. Mizutani, T. Tsuchiyama, S. Takaki, Acta Mater. 65 (2014) 251-258.
[347] O. Dmitrieva, D. Ponge, G. Inden, J. Millan, P. Choi, J. Sietsma, D. Raabe, Acta Mater. 59 (2011) 364-374.
[348] J. Han, Y.K. Lee, Acta Mater. 67 (2014) 354-361.
[349] D.P. Yang, D. Wu, H.L. Yi, Scr. Mater. 161 (2019) 1-5.
[350] D.P. Yang, D. Wu, H.L. Yi, Scr. Mater. 174 (2020) 11-13.
[351] A. Kwiatkowski da Silva, G. Inden, A. Kumar, D. Ponge, B. Gault, D. Raabe, Acta Mater. 147 (2018) 165-175.
[352] Y.X. Wu, W.W. Sun, M.J. Styles, A. Arlazarov, C.R. Hutchinson, Acta Mater. 159 (2018) 209-224.
[353] S. Lee, B.C. De Cooman, Metall. Mater. Trans. A 47 (2016) 3263-3270.
[354] W. Kim, S. Kang, B. Jian, S.W. Lee, B.C. De Cooman, Metall. Mater. Trans. A 49 (2018) 4389-4393.
[355] H.W. Luo, C.H. Qiu, H. Dong, J. Shi, Mater. Sci. Technol. 30 (2014) 1367-1377.
[356] F. Huyan, J.-Y. Yan, L. Höglund, J. Ågren, A. Borgenstam, Metall. Mater. Trans. A 49 (2018) 1053-1060.
[357] G. Miyamoto, H. Usuki, Z.D. Li, T. Furuhara, Acta Mater. 58 (2010) 4492-4502.
[358] J. Emo, P. Maugis, A. Perlade, Comp. Mater. Sci. 125 (2016) 206-217.
[359] Q. Lai, M. Gouné, A. Perlade, T. Pardoen, P. Jacques, O. Bouaziz, Y. Bréchet, Metall. Mater. Trans. A 47 (2016) 3375-3386.
[360] N. Yan, H. Di, R.D.K. Misra, H. Huang, Y. Li, Mater. Sci. Eng. A 753 (2019) 11-21.
[361] X. Zhang, G. Miyamoto, Y. Toji, T. Furuhara, Metals 9 (2019).
[362] Z.-Q. Liu, G. Miyamoto, Z.-G. Yang, C. Zhang, T. Furuhara, Metall. Mater. Trans. A 45 (2014) 5290-5294.

Mr. Zongbiao Dai is currently a PhD student of Materials Science and Engineering at Tsinghua University, Beijing, China. He obtained his bachelor degree at University of Science and Technology Beijing (USTB), China in 2016. Since 2016, he has been studying in the Tsinghua University. His PhD project is focused on thermodynamics and kinetics of phase transformation in advanced high strength steels, e.g. quenching & partitioning steels and medium Mn steels.

Dr. Hao Chen is associate professor of Materials Science and Engineering at Tsinghua University, Beijing, China. He obtained his Bs and MsC degree at Tianjin University, China in 2007 and 2009, his PhD degree with "Cum laude" at Delft University of Technology in 2013. He also spent a year as postdoctoral fellow at University of British Columbia, Canada in 2014. He received the 2015 Aaronson award for his work in the field of phase transformations. Dr. Chen has published 70+ refereed articles in international journals such as Acta Materialia, et. al. He has delivered 15+ invited talks at international conferences like TMS, PRICM, etc. Dr. Chen's research is focused on two areas: (i) Thermodynamics and kinetics of phase transformation and microstructure change in metals, and (ii) Alloy by design, including advanced high strength steels, heat resistant steels, alloy design for additive manufacturing, et.al. In general, His research contains fundamental aspects, but it is within the context of industrial interest.

Dr. Ran Ding is currently an associate professor in School of Materials Science and Engineering at Tianjin University. He received his Ph.D. in Materials Science from University of Science and Technology Beijing in 2016, and then worked as a postdoctoral researcher in School of Materials Science and Engineering at Tsinghua University. His research interests include (1) austenite formation and decomposition mechanism, (2) architecturing novel microstructure via chemical boundary engineering, and (3) micromechanical behavior of multiphase steels containing retained austenite.

Dr. Qi Lu is currently a researcher at China Science Lab, General Motors Global R&D. He received B.Sc. degree from Northeastern University in 2008, M.S. degree at Institute

of Metal Research, Chinese Academy of Sciences in 2011, and Ph.D. degree from Delft University in 2015. His current research focuses on the development and application of advanced automotive steels.

Dr. Chi Zhang is professor of Materials Science and Engineering at Tsinghua University, Beijing, China. He obtained his Bs and PhD degree at Tsinghua University, China in 1996 and 2001. He also spent two years as postdoctoral fellow at Ibaraki University, Japan in 2001-2003. Dr. Zhang has published 140+ refereed articles in international journals such as Acta Materialia, et.al. Dr. Zhang's research is focused on the development of advanced high strength steels and reduced activation ferritic/martensitic steels.

Dr. Zhigang Yang is full professor of Materials Science and Engineering at Tsinghua University, Beijing, China. He obtained his Bs, MsC and PhD degree at Tsinghua University, China in 1989, 1993 and 1996. He also spent two years as postdoctoral fellow at Ibaraki University, Japan in 1997-1999, and spent one year as visiting scholar at Lawrence Berkeley National Lab. USA. Dr. Yang has published 100+ refereed articles in international journals such as Acta Materialia, et.al. Dr. Yang's research is focused on (i) Phase transformation in steel, (ii) Mechanical properties of steels, (iii) Oxidation of metal and heat-resistant steels and (iv) Metallic coating materials and processing on steels.

Dr. Sybrand van der Zwaag (1955) is full professor Materials Science at the faculty of Aerospace Engineering of the Delft University of Technology (The Netherlands) and 1000 Talent Foreign Scholar at the School Material Science and Engineering, Tsinghua University, Beijing (PR China). He obtained an MSc in metallurgy from the TU Delft and a PhD in applied physics from Cambridge University (UK). He then worked as a polymer scientist at the Corporate Research Lab of Akzo Nobel on the next generation super fibres. In 1992 he was appointed full professor in the chair Microstructural Control in Metals. In 2003 he moved to the Faculty of Aerospace Engineering to create

the chair Novel Aerospace Materials. In 1996 he was one of the four academic founders of the Netherlands Institute for Metals Research. From 2005-2017 he was the Scientific Director of the national research program on Self-Healing Materials. In 2012 he received the title of Distinguished Professor from the TU Delft and in 2017 he received an Honorary Doctorate from Mons University (Belgium) as well as a Chinese 1000 talent foreign Scientist and a professorship at Tsinghua University. In 2018 he received the Grande Medaille from the French Materials Science Society. He has published over 550 journal publications and has supervised 55 PhD students.

Author Photo

Mr. Zongbaio Dai

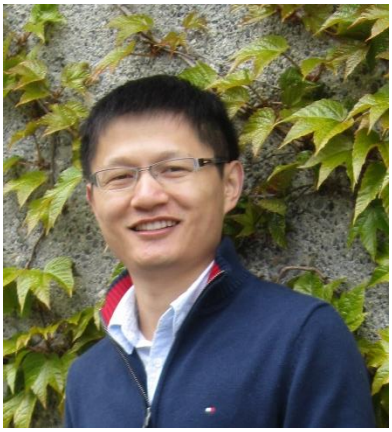

Dr. Hao Chen

Dr. Ran Ding

Dr. Qi Lu

Dr. Chi Zhang

Dr. Zhigang Yang

Dr. Sybrand van der Zwaag

Click here to access/download

Supporting File

Supporting-file.docx

Declaration of interests

☒ The authors declare that they have no known competing financial interests or personal relationships that could have appeared to influence the work reported in this paper.

☐The authors declare the following financial interests/personal relationships which may be considered as potential competing interests:

none